Old Dominion University

# ODU Digital Commons

Summer 2021

# Enhancing Thermal Stability of Perovskite Solar Cells with a Polymer Through Grain Boundary Passivation

Tanzila Tasnim Ava
*Old Dominion University*, tava001@odu.edu

## Recommended Citation

# ENHANCING THERMAL STABILITY OF PEROVSKITE SOLAR CELLS WITH A

# POLYMER THROUGH GRAIN BOUNDARY PASSIVATION

by

Tanzila Tasnim Ava
B.S. June 2012, University of Dhaka
M.S. October 2015, Karlsruhe Institute of Technology

A Dissertation Submitted to the Faculty of
Old Dominion University in Partial Fulfillment of the
Requirements for the Degree of

DOCTOR OF PHILOSOPHY

ELECTRICAL AND COMPUTER ENGINEERING

OLD DOMINION UNIVERSITY
August 2021

Approved by:

Gon Namkoong (Director)

Hani E. Elsayed-Ali (Member)

Helmut Baumgart (Member)

Tarek Abdel-Fattah (Member)

**ABSTRACT**

ENHANCING THERMAL STABILITY OF PEROVSKITE SOLAR CELLS WITH A
POLYMER THROUGH GRAIN BOUNDARY PASSIVATION

Tanzila Tasnim Ava
Old Dominion University, 2021
Director: Dr. Gon Namkoong

Organic-inorganic halide perovskite solar cells have emerged as a promising photovoltaic technology due to their superb power conversion efficiency (PCE) and very low material costs. While perovskite solar cells are expected to eventually compete with existing silicon-based solar cells on the market, their long-term stability has become a major bottleneck. In particular, perovskite films are found to be very sensitive to external factors such as air, UV light, light soaking, thermal stress and others. Among these stressors, light, oxygen and moisture-induced degradation can be slowed by integrating barrier or interface layers within the device architecture. However, the most representative perovskite absorber material, $CH_3NH_3PbI_3$ (MAPbI$_3$), appears to be thermally unstable even in an inert environment. This poses a substantial challenge for solar cell applications because device temperatures can be over 45 °C higher than ambient temperatures when operating under direct sunlight. In this thesis, the thermal stability of perovskite solar cells was primarily investigated.

Initially, we systematically studied the effects of heating and cooling processes on the principal photovoltaic performance of perovskite solar cells by combining temperature-dependent J-V, steady-state PL, UV-VIS and time-resolved lifetime decay measurements. In particular, we have observed the dynamic evolution of degraded crystallinity, increased charge trapping, deep trap depth and PbI$_2$ phase. During the heating process, the thermal degradation of the perovskite film was observed at 70 ° C or higher. An increase in the disordered phase of the perovskite film

involved a drastic increase in charge trapping and the development of a deeper trap depth. Interestingly, we observed that the degradation of the perovskite film persisted even after the temperature was dropped, which led to irreversible J-V characteristics of the perovskite solar cell.

Later, we introduced a polymer layer of PMMA which improved thermal stability for more than 1000hrs at 85°C. Without PMMA, host-casted MAPbI$_3$ films suffered rapid thermal degradation, forming a number of pin-holes at GBs and then extending into GIs. Rapid thermal degradation of perovskite GBs without PMMA may be due to the rich moisture chemical structure of hydrated $(CH_3NH_3)_4PbI_6\bullet H_2O$. At the elevated temperature, hydrated $(CH_3NH_3)_4PbI_6\bullet H_2O$ grain boundaries might suffer from moisture-assisted decomposition, forming a number of pin-holes at GBs. Conversely, we observed high thermal stability of perovskite films by introducing PMMA to induce marked thermal stability at GBs. It is believed that the excellent hygroscopicity of PMMA played an active role in absorbing moisture from hydrated $(CH_3NH_3)_4PbI_6\bullet H_2O$ GBs and driving them out through the GB channel. We believe that continuous functionalization of perovskite GBs or crosslinking perovskite GBs with PMMA molecules might drastically render perovskite GBs chemically robust, resilient, and heat-resistant. Moreover, we mixed inorganic cesium (Cs) cation into the perovskite, which improved thermal stability at a higher temperature of 120°C.

Finally, we have fabricated perovskite solar cells in an antisolvent method in which the perovskite film does not contain deeper grain boundary like hot-casted perovskite thin film. Also, we introduced a polymer (polyimide) on the top of the perovskite solar cell which has a large contact angle and glass transition temperature. Consequently, perovskite solar cells with polyimide showed thermal stability without any efficiency decrement more than 30days.

This thesis is dedicated to my parents.

# ACKNOWLEDGMENTS

# TABLE OF CONTENTS

# LIST OF FIGURES

# CHAPTER 1

# INTRODUCTION

## 1.1 Motivation of this work

It is inevitable to replace non-renewable energy sources with renewable energy sources, as the proverb says, "*Future is green energy and renewable energy*". In everyday life, from the electricity that runs homes to the cars on road, mankind is largely dependent on the use of fossil fuels such as coal, oil, natural gas, etc. Fossil fuels are carbon-rich deposits extracted and burned for producing energy. When fossil fuels are burned as energy sources, they produce a large amount of greenhouse gases (GHG) such as carbon dioxide ($CO_2$) which gets trapped in the environment causing global warming. According to the U.S. Energy Information Administration (EIA), in the year 2018, $CO_2$ emissions from fossil fuels used in the energy sector were equal to about 75% of total U.S. GHG emissions caused by humans. Human activities also cause the emission of other greenhouse gases such as methane ($CH_4$), nitrous oxide ($N_2O$), hydrofluorocarbons (HFCs), etc. A part of these gases originates from the decomposition of fossil fuels as well. The combined emissions of these other greenhouse gases accounted for about 19% of total U.S. anthropogenic GHG emissions in 2018 [1].

The constituents of fossil fuels are carbon and hydrogen. When fossil fuels are burned, oxygen combining with carbon forms $CO_2$ and with hydrogen forms water ($H_2O$). These chemical reactions release heat which is used for energy. The amount of $CO_2$ formation is dependent on the amount of carbon in the fuel; hence, the amount of $CO_2$ emission depends on the fuel source. In 2019, about 46% of U.S. energy-related $CO_2$ emissions came from burning petroleum fuels, 33% came from burning natural gas, and 21% came from burning coal (Fig. 1).

**U.S. energy consumption by source, 2019**
total = 100.2 quadrillion British thermal units

natural gas 32%
petroleum 37%
coal 11%
nonfossil 20%

**U.S. energy-related carbon dioxide emissions by source, 2019**
total = 5,130 million metric tons

coal 21%
natural gas 33%
petroleum 46%
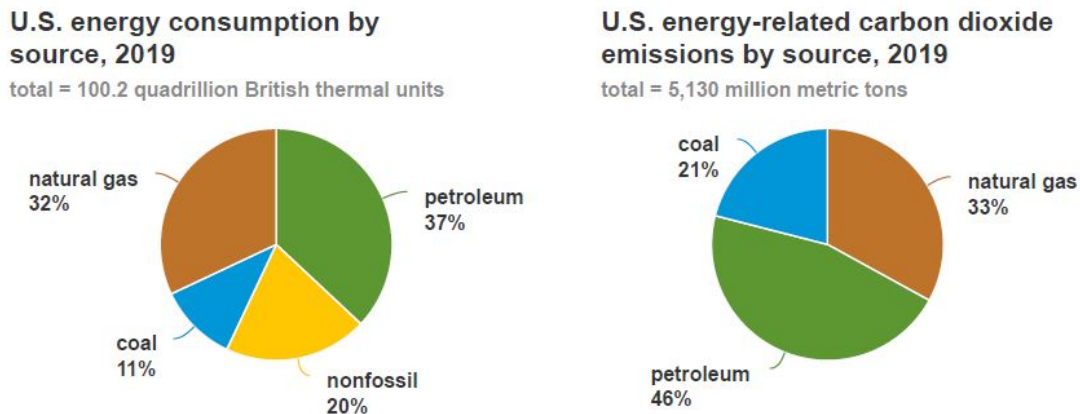
Fig. 1. U.S. energy consumption and energy related carbon dioxide emission by source reported in 2019. Note: nonfossil is nuclear and renewable energy [2].

Excessive $CO_2$ emission leads to the need for an alternative to fossil fuels. In particular, fossil fuels used in the energy sector can be replaced with renewable energy sources to create a green and clean environment on the earth. Renewable energy also referred to as "clean energy" comes from natural resources which replenishes naturally. The renewable energy sector is flourishing, keeping its promise to maintain a clean energy future. The major types of renewable energy sources include biomass, hydropower, geothermal, wind, and solar. The use of renewable energy sources is increasing day by day. The consumption of biofuels, geothermal, solar, and wind energy in the United States in 2019 was nearly three times greater than in 2000 [3]. In 2019, the energy provided by renewable sources was about 11.5 quadrillion (1 quadrillion is the number 1 followed by 15 zeros) Btu (Btu: British thermal units). This amount is approximately equal to 11.4% of total U.S. energy consumption (Fig. 2). About 56% of total U.S. renewable energy consumption in 2019 was from the electric power sector, and 17% of electricity generation was

from renewable energy sources (Fig. 3). Renewable energy can play an important role in reducing the emission of $CO_2$ and pollution. It is projected that the use of renewable energy sources will continue to increase and be significantly prominent through 2050.



Fig. 2.  Primary energy consumption by energy in the U.S. in 2019. Note: Sum of components may not equal 100% because of independent rounding [4].

From ancient times, solar energy has been used by mankind to harvest food, stay warm, and dry food. In today's world, we use sunlight to heat buildings, warm water, or power devices. Solar or photovoltaic (PV) technology is the process by which sunlight absorbed by a PV material is converted into electricity. Solar energy is one promising renewable energy source with few environmental affects as long as solar panels are installed responsibly. A solar cell is a device that converts light energy into electrical energy through photovoltaic effects. The photovoltaic effect

was first discovered by the French physicist Becquerel in 1839 [5]. The first successful solar cell with a semiconductor/metal interface was prepared by Fritts in 1883; however, the efficiency was only ~1%. In 1954, Pearson et al. from US Bell Labs developed the first crystalline silicon solar cell with a photo-conversion efficiency of 4.5% which started a new era in the field of solar power [6].
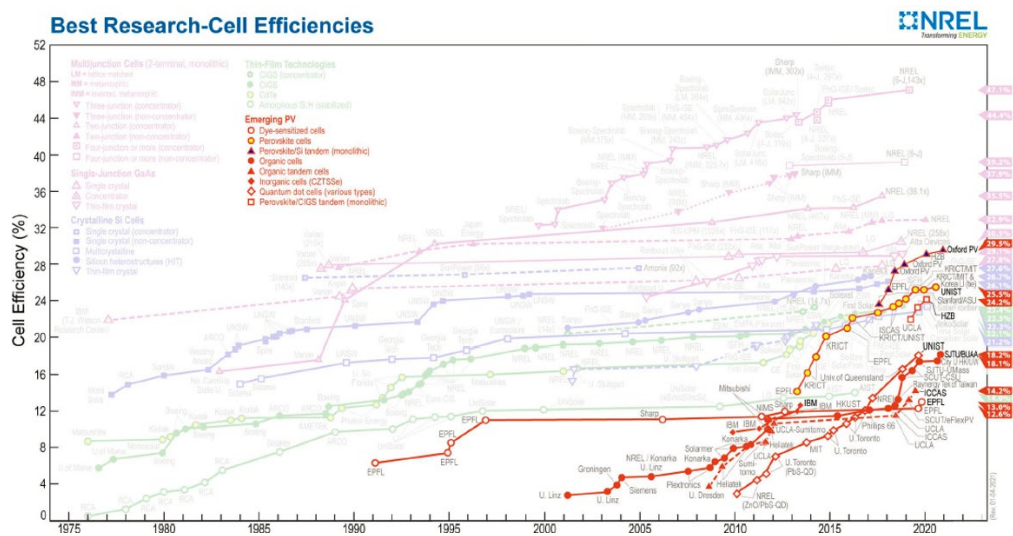


Fig. 3. Best research cell efficiency of emerging PV technologies certified by NREL. The champion efficiency of perovskite solar cell was recorded to be 25.5% achieved by Ulsan National Institute of Science and Technology (UNIST) [8].

Almost 90% of the current commercial PVs is taken by silicon PV since it provides module efficiency of ~27%, long sustainability of about 25 years and low cost of 0.3$/W [7,8]. An emerging PV technology has developed rapidly in recent years which is known as perovskite solar

cells. In comparison with silicon solar cells, the perovskite solar cell is promising with an efficiency of 25.5% and manufacturing cost almost half of silicon PV [7,8]. The latest efficiency chart of perovskite PV technology recorded by National Renewable Energy Laboratory (NREL) is shown in Fig. 3. However, the stability of perovskite is still a major issue hindering the commercialization of perovskite solar cells.

In this work, the stability of perovskite solar cells was extensively studied to address the thermal instability of perovskite solar cells and a few possible solutions to achieve thermally stable perovskite solar cells which will be discussed in the following chapters.

## 1.2 Overview

Chapter 1 presents the motivation of this dissertation describing U.S. energy consumption source and the future of renewable energy. In addition, an introduction of solar energy as renewable energy sources and the future of perovskite solar cells is depicted.

Chapter 2 provides a detailed illustration of perovskite material and a perovskite solar cell. It also provides the basic working principle of solar cells and current-voltage characteristic which is the basis of photovoltaic performance. Finally, it illustrates the advantages and limitations of perovskite solar cells describing the necessity of stable perovskite solar cells to make them commercially available.

Chapter 3 provides detailed fabrication and characterization techniques of a perovskite solar cell. Two types of perovskite thin film (hot casting and conventional) fabrication techniques will be described. Detailed morphological and structural characterization techniques including XRD, UV-vis, NMR, SEM, EDS IR nonoscopy, etc. will be given.

Chapter 4 investigates the performance of a perovskite solar cell during a heating and cooling temperature cycle between room temperature and 82 °C. Temperature dependent steady-state photoluminescence (PL) and time-resolved PL are used to find out the origin of irreversible degradation of perovskite solar cells. Perovskite films undergo an irreversible degradation above 70 °C which is also evident in the XRD and UV-vis measurement [9].

Chapter 5 introduces a new polymer of PMMA to improve the thermal stability of perovskite thin film. PMMA is applied on the top of perovskite film which makes perovskite thin film stable for more than 1000 hrs at 85 °C. GB is crosslinked with PMMA to stabilize the perovskite film which is proven using NMR, IR nanoscopy and several other characterization techniques [10].

Chapter 6 provides the thermal stability of perovskite film using mixed cation. In particular, a small amount of inorganic cation cesium (Cs) is helpful to achieve improved thermal stability of Cs based perovskite film with PMMA at an elevated temperature of 120 °C.

Chapter 7 presents the fabrication technique of perovskite thin film using an antisolvent approach. The antisolvent method removed larger grain boundaries from the perovskite film typically observed in a hot casting technique. The removal of deeper grain boundaries will particularly be beneficial to the performance and stability of perovskite solar cells since deeper and large grain boundaries are considered to be defective and prone to degradation under thermal stress. We introduce another polymer polyimide on top of perovskite solar cells which stabilizes the perovskite solar cell for more than a month of heating at 85 °C.

Chapter 8 depicts the summary and future prospects of this research. It is shown that both polyimide and PMMA could address the issue of thermal and air stability of perovskite solar cell.

**CHAPTER 2**

**BACKGROUND OF THE STUDY**

**2.1 Introduction to perovskite solar devices**

The rapid growth of organic-inorganic hybrid perovskite solar cells (PSCs) has made this type of solar cell one of the promising candidates on the market to compete with existing solar cells. The highest efficiency for PSCs has been recorded to be more than 25% to date [8] due to advancements in solvent engineering [11], interface engineering [12] and composition engineering [13]. The outstanding performance of PSCs is attributed to the excellent optoelectronic properties of perovskite materials such as high absorption coefficient, weak exciton binding energy, and long diffusion length [14,15,16,17,18].

Perovskite was first discovered in the 19th century by the Prussian Gustav Rose in 1839 and named perovskite after the renowned mineralogist Count Lev A. Perovskiy. A series of oxides with similar structures were later discovered and classified as perovskite compounds [19]. Miyasaka and co-workers first introduced organic-inorganic hybrid perovskite solar cells in DSSCs having an efficiency of only 3.81% [14]. The poor stability and efficiency of liquid electrolyte based DSSCs were attributed to iodine-based redox processes. The efficiency increased to 10% when the liquid electrolyte was replaced with a solid-state hole transport layer of spiro-OMeTAD and led to improved stability as well [20,21]. Since then, two common device architectures have been developed for perovskite solar devices. The first structure is similar to the classical solid-state DSSCs [22], where metal-halide based PSCs were made of a mesoporous scaffold of $TiO_2$ nanoparticles and a thin $TiO_2$ blocking layer between the FTO substrate and the absorber layer. The second structure is the planer heterojunction structure consisting of a solid

perovskite layer with electron and hole selective contacts, which was introduced by Snaith, et al. [21]The planar heterojunction structure can be fabricated at a low temperature (<150 °C), while the mesoporous $TiO_2$ scaffold structure requires high temperature (<400 °C), making the former structure superior to the later structure [23]. The projected theoretical maximum efficiency of solar cells made of this type of device structures is more than 30% which has already surpassed the practical efficiency of ~25% for silicon solar cells [24].

## 2.2 Properties of Perovskite

Perovskite materials possess phenomenal opto-electronic properties which make them unique and result in outstanding performance. Properties of perovskite material vary based on their chemical compositions. The bandgap of perovskite can be tuned depending on the type of halide present in the material. For example, Iodide based perovskites have the smallest bandgap (1.7-1.8eV) while Bromide based perovskites have the largest bandgap (2.2-2.3eV) [25]. In addition, the crystalline phase of these materials is highly dependent on temperature and chemical structure. Here, some of the unique properties of perovskite materials will be described which are considered to play significant role in the performance of perovskite solar devices.

### 2.2.1 Crystal structure

A typical unit cell structure of a basic perovskite compound is shown in Fig. 4. The generic structure of perovskite materials used in PSCs comprises of $ABX_3$ where A is a univalent cation, that is, methylammonium (MA) $CH_3NH_3^+$, formamidinium (FA) $CH_2(NH_2)_2^+$, ethyl-ammonium $CH_3CH_2NH_3^+$, $Cs^+$, or $Rb^+$, while B stands for divalent cations (e.g., $Pb^{2+}$, $Sn^{2+}$, $Ge^{2+}$) and X for halogen anion (e.g., $F^-$, $Cl^-$, $Br^-$, $I^-$). Among the structures, methyl-ammonium-lead-iodide

(MAPbI₃) is the most widely used perovskite light absorber. Recent research is also focusing on lead-free perovskites due to concerns about the toxicity of lead in the large-scale manufacture of the device in the future.
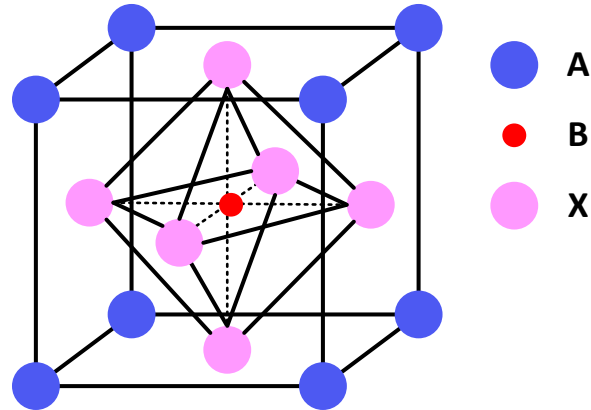


Fig. 4. The unit cell of cubic perovskite (ABX₃), where the red spheres at lattice corners are A cations, the green sphere at the center is a B cation, and the blue spheres at the lattice faces are X anions [26].

The halide perovskites obtain a desired crystal symmetry by maintaining an allowable tolerance factor. A tolerance factor developed by Goldschmidt [27] determines the radii sizes associated with cubic symmetry, described by

$$t = \frac{R_A + R_X}{\sqrt{2}(R_A + R_X)} \qquad (1)$$

where $R_A$, $R_B$, $R_X$ are the ionic radii of A, B, X, respectively. The tolerance factor provides a rough estimate of the stability and distortion of crystal structures of a compound. In addition, it gives an idea of whether the phase is cubic (t = 1) or deviates into the tetragonal or orthorhombic phase [28]. In general, an established tolerance factor value for halide perovskites lies in the range of $0.85 < t < 1.11$ [28]. Non-perovskite structures are formed when the tolerance factor is higher or lower.
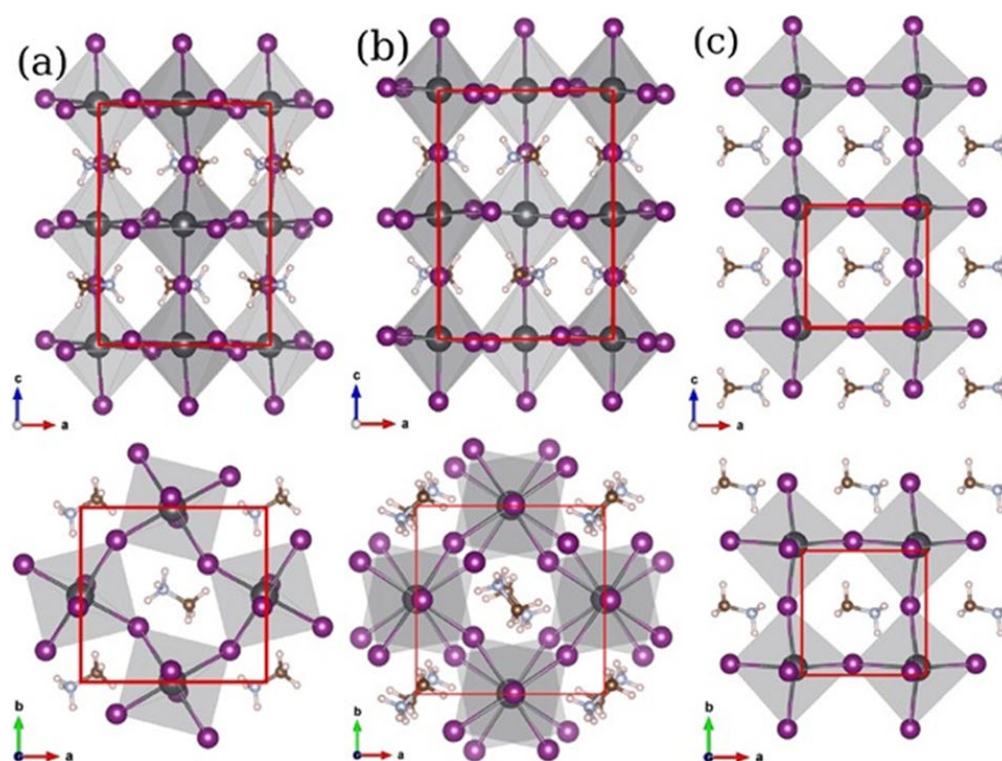


Fig. 5. Comparison of (a) orthorhombic, (b) tetragonal, and (c) cubic perovskite phases obtained from structural optimization for the case of MAPbI$_3$. Top row: ac-plane, bottom row: ab-plane [29].

In an inorganic-organic hybrid perovskite, it is difficult to calculate the absolute tolerance factor as the organic cation has a non-spherical geometry [28]. However, it is possible to qualitatively analyze the transition of structure in these materials. For example, formamidinium lead iodide, $HC(NH_2)_2PbI_3$ ($FAPbI_3$), has a larger A cation than methylammonium lead iodide, $CH_3NH_3PbI_3$ ($MAPbI_3$), and a larger cation would generally represent a higher tolerance factor [28]. Two phases can be obtained in solution processed $FAPbI_3$ materials. One is the photoactive α-phase (black phase) and the other is a non-photoactive phase (yellow phase or δ-phase) [28]. Perovskite materials vary in phases with the change of temperature. Perovskite materials show a stable orthorhombic (γ) phase at a temperature lower than 100 K. When the temperature is increased to 160 K, the tetragonal phase (β) starts to appear [30]. With further increase in temperature to about 330 K, the tetragonal phase(β) is replaced by a stable cubic phase (α) [31]. Fig. 5 shows all three perovskites with three different phases. The thermal stability of perovskite materials is particularly influenced by the tetragonal-cubic phase transition at higher temperature.

### 2.2.2 Optical Properties

Perovskite materials have a high absorption capacity reflected by a high optical absorption coefficient ($\sim 10^5$/cm). The absorption layer of PSCs can be very thin even below 500nm, and the layer can absorb enough sunlight to achieve high efficiency of 15% or more. The optical absorption mechanism for first-generation, second-generation, and perovskite-based solar cell absorbers were schematically compared by Yin et al. [25] as shown in Fig. 6. Si being an indirect semiconductor, the transition probability between band edges is two orders lower, which makes the absorber thickness two orders thicker in first generation solar cells [25]. Both the second-generation absorber (GaAs) and the halide perovskite absorber (e.g., $MAPbI_3$) have direct bandgaps; however,

their electronic structures are different. The atomic p orbital in the MAPbI₃ conduction band (CB)

lower part is less dispersive than the s orbital in the lower part of GaAs CB. Therefore, the DOS

in the lower CB of MAPbI₃ is higher than that of GaAs making it superior in terms of optical

absorption capacity.
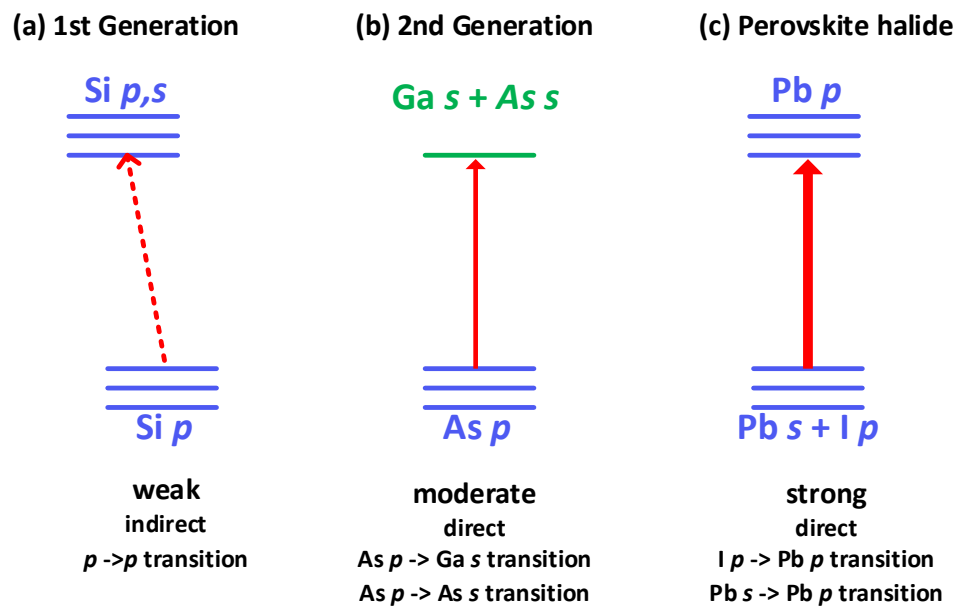


Fig. 6.   The schematic optical absorption of (a) first-generation, (b) second-generation, and (c)

halide perovskite solar cell absorber. GaAs has been chosen as a prototypical second-generation

solar cell absorber [25].

## 2.3 Perovskite solar device architecture

The initial perovskite solar cells were designed based on the structure of dye sensitized solar cells (DSSC). The first reported DSSC based PSCs showed 3.8% device efficiency which lasted only for a few minutes [14]. To avoid this degradation, a solid-state hole transport layer of polymer spiro-MeOTAD was used and reported to have ~ 10% efficiency and to improve device stability [20,21]. Presently, two device architectures are commonly found for PSCs, which include mesoporous scaffold [20,21,32] and planar heterojunction structures [12,33]. In the mesoporous scaffold structure, the PCE depends on the pore size, porosity and morphology of the metal oxide nanoparticles, which predominantly determine morphological change and carrier lifetime of the perovskite layer. However, the fabrication of the inorganic metal oxide mesoporous scaffold is complicated and requires a high processing temperature of more than 450 °C [32], making the fabrication procedure expensive. The layer by layer fabrication of planar heterojunction PSCs is either conducted through high vacuum deposition [33] or a solution-based method [12,34]. However, due to the dewetting process and sensitivity to the atmosphere, the production of uniform films is somewhat challenging by implementing cost-effective solution processes. A schematic of both the planar and mesoscopic structures can be found in Fig. 7. The device architecture of a typical PSC comprises of a perovskite absorber layer sandwiched between two selective contacts, an electron transport layer (ETL) such as $TiO_2$, and a hole transport layer (HTL) such as spiro-OMeTAD. Metal contacts are formed on either side of the transport layers. A transparent conducting oxide such as indium-doped tin oxide (ITO) or fluorine-doped tin oxide is formed as window contact, and a back contact is formed using Au, Ag, Al, etc.

Perovskite devices with a planar heterojunction architecture can be fabricated with either a n–i–p or p–i–n structure due to the ambipolar semiconducting characteristic of the perovskite

[35]. Unfortunately, the n–i–p type planar cells sandwiched between TiO₂ as electron transport layer (ETL) and (2,2',7,7'-tetrakis(N,N-di-pmethoxyphenylamine)9,9'-spirobifluorene) (spiro-OMeTAD) as hole transport layer (HTL) exhibit a serious hysteresis, induced time dependent behaviors, poor stability in moisture and temperature, and reduced photocurrent-voltage (*J-V*) characteristics in the PSCs [36,37]. In contrast, inverted planar heterojunction perovskite solar cells with a p–i–n structure attracted considerable attention due to having less serious hysteresis than the n–i–p type planar structures [38]. In the inverted planar PSCs, poly(3,4-ethylenedioxythiophene) polystyrene sulphonate (PEDOT:PSS) is one of the most widely used HTLs; however, its acidic and hygroscopic nature significantly reduces device stability, which leads to the replacement of organic HTLs with an inorganic one. In this thesis, we have fabricated perovskite solar cells using an inverted p-i-n structure.
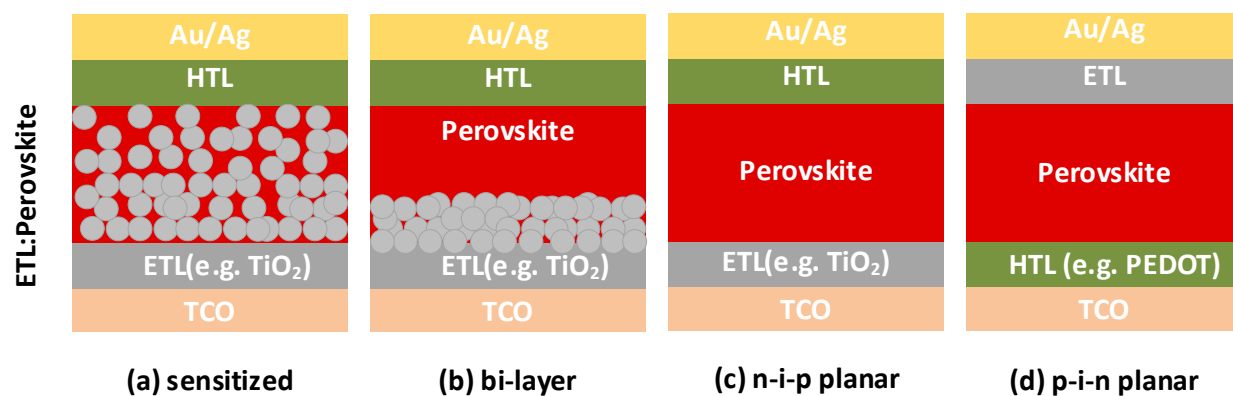


Fig. 7. Various device architectures for organometal trihalide perovskite solar cells. (a) Mesoporous sensitized, (b) bi-layer, (c) n-i-p planar and (d) p-i-n planar. ETL, HTL, and TCO

stand for electron transport layer, hole transport layer, and transparent conducting oxide, respectively [39].

**2.4 Working principle of perovskite solar devices**
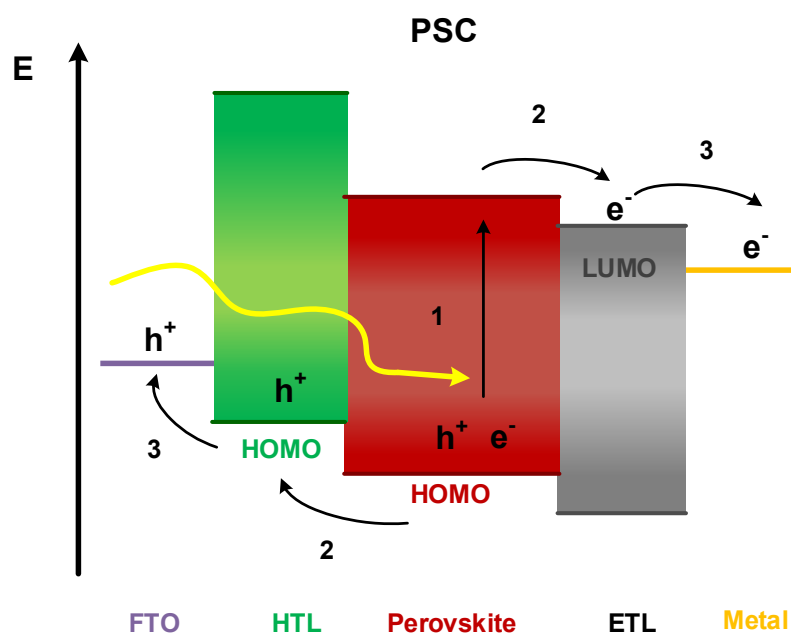


Fig. 8.  Band diagram and main processes in PSCs: 1. Absorption of photon followed by exciton formation; 2. Exciton diffusion; 3. Charge separation; 4. Charge extraction [40].

As mentioned in the device architecture section before, a typical perovskite solar cell consists of an active layer, charge transport layers and metal electrodes. The basic working principle of PSCs has three major functioning steps, as shown in Fig. 8. Upon illumination, light is incident on the transparent electrode and absorbed by the photons. The absorption of photons

leads to the formation of photo-generated charge carriers (excitons) (Step 1). Subsequently, the dissociation of excitons occurs at the interface between the absorber and the charge transporting layers. The separated electron and hole diffuse to the electron-transporting layer (ETL) and hole-transporting layer (HTL), respectively (Step 2). Finally, the electrons migrate to the anode, and the holes migrate to the cathode where the charge is extracted by the electrodes to an external circuit to generate current (Step 3) [41].

## 2.5 Current-voltage characteristics

### 2.5.1 Equivalent circuit model

Fig. 9 shows an equivalent circuit of a solar cell. Basically, a simple PV device can be modelled by the Shockley ideal photodiode equation as in Eq. 2.

$$\mathrm{I} = I_{ph} - I_0 \left[ exp \left( \frac{eV}{k_B T} \right) - 1 \right] \qquad (2)$$

Here $I_{ph}$ is the photocurrent provided by the photoactive absorbing layer, and $I_0$ is the diode reverse saturation current. As the applied voltage (*V)* increases, the diode current (which opposes the photocurrent) exponentially increases.[9]

$$\mathrm{I} = I_{ph} - I_0 \left[ exp \left\{ \frac{e(V+IR_s)}{nk_B T} \right\} - 1 \right] - \frac{V+IR_s}{R_{sh}} \qquad (3)$$

The real circuit, in practice contains a shunt and series resistances, $R_{sh}$ and $R_s$ and a non-ideal diode model is considered, which can be expressed as Eq. 3. Here, $k_B$ is the Boltzmann constant, *T* is the temperature in kelvin, n is the ideality factor and n=1 for an ideal diode. In an ideal diode all recombination occur outside the depletion region of the absorber layer, while in a

non-ideal diode, recombination occurs in the absorber layer and the ideality factor n can be more than 2.
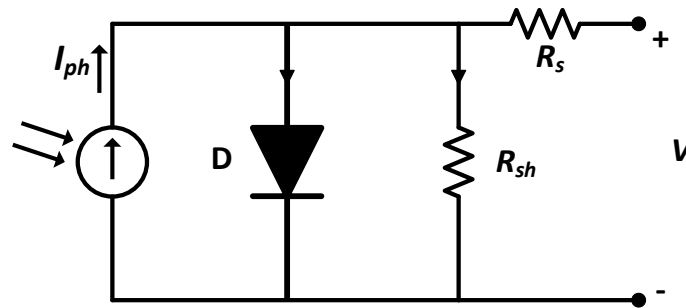


Fig. 9.  Equivalent circuit model of a solar cell.

**2.5.2 Current-Voltage measurements**

The device performance of a solar cell is generally determined by the current–voltage (I-V) sweeps. The current of a solar cell with a known active area is measured with different applied voltage biases. Fig. 10 illustrates a typical I-V curve for a solar cell, where the direction of current is considered to be positive. The I-V curve illustrates the key performance parameters of the solar cells, which includes the short circuit current ($I_{SC}$), open circuit voltage ($V_{OC}$), and the maximum power point (MPP). $I_{SC}$ is the photocurrent density provided by the solar cell when there is no applied voltage. $I_{SC}$ is dependent on the amount of absorbed light as well as the quality of the perovskite absorber layer. $V_{OC}$ is the voltage provided by the solar cell when no current is applied. The open circuit voltage $V_{OC}$ is dependent on the band structure of the absorber layer. In addition to $V_{OC}$ and $I_{SC}$, the power density, $P$, can be calculated at each point on the P-V curve where,

$$P = IV \qquad\qquad (4).$$
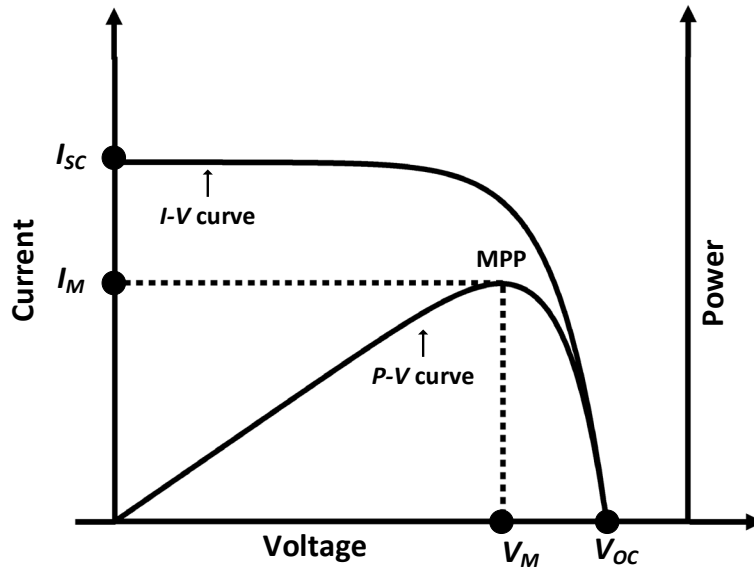
Fig. 10.  Solar cell *I-V* and power operation curve with the characteristic of $V_{OC}$ and $I$sc.

The ratio of maximum power density to the incident power density determines the power conversion efficiency (PCE). The maximum power density is achieved at the MPP which corresponds to the maximum power voltage ($V_M$) and maximum power current ($I_M$). The fill factor can be calculated using MPP and defined as

$$FF = \frac{I_M V_M}{I_{sc} V_{OC}} \qquad (5).$$

The Fill Factor (FF) is a percentage calculated from the ratio of area *A* to area *B*, shown in Fig. 10. B is the area corresponding to the product of $I_{SC}$ and $V_{OC}$, whereas A is the area corresponding to the maximum power. FF provides a metric for the non-ideality of the solar cell and determines the "squareness" of the I-V characteristics. A good solar cell has a high *FF*, and

this is a performance metric that needs to be maximized. PCE of a solar cell depends on the FF, $I_{SC}$, and $V_{OC}$ and can be calculated as

$$PCE, \eta\ (\%) = \frac{P_{OUT}}{P_{in}} \times 100 = \frac{I_{SC}V_{OC}FF}{P_{in}} \times 100 \qquad (6).$$

## 2.6 Limitations of perovskite solar devices

The promising performance of perovskite solar cells has been attributed to extraordinary material properties including high absorption coefficient, long charge carrier diffusion length, low exciton binding energy, and tunable bandgap [15,16,42,43,44,45]. Despite achieving a comparable lab-scale device efficiency to commercially available solar cells, PSCs have critical issues regarding stability. Standard PV modules available on the market typically have a warranty to retain their initial efficiency for 20–25 years. However, perovskite solar cells are prone to degradation when exposed to air, UV light, thermal stress (heat), light soaking, electric fields, and many other factors [46,47,48]. Extensive research has recently been focused on the study of degradation mechanisms to improve stability of the perovskite solar device. Improved stability could be achieved by device encapsulation, adding UV filters, and suppressing trap states for degradation caused by air, UV light, and electric fields, respectively. A deeper understanding and improvement to these limitations is crucial to upscaling the performance of PSCs.

**2.6.1 Stability of perovskite materials**

***Structural stability***

As described in section 2.2.1, the general structure of perovskite compounds consists of $ABX_3$, where A and B are cations and X is an anion. Usually, the A cations are larger than the B cations. In all cases, the halide perovskites must maintain an allowable tolerance factor to obtain the desired crystal symmetry since crystal structure and phase transition largely affect material properties. The A cation does not directly contribute toward electronic properties [49,50,51]; however, the size of A cations can cause distortion of the B-X bonds, unfavorably affecting the symmetry. Cubic symmetry provides optimum electronic properties due to a high degree of ionic bonding. Mismatch of crystal components outside of the ideal tolerance range results in octahedral tilting that can affect electronic properties. The structural stability of the perovskites is critical when used in photovoltaic devices, which is expected to remain stable for more than 25 years [52]. The structural stability is defined by the ability for a crystalline phase to be stable over a wide range of external factors such as heat, pressure, moisture, etc.

In recent years, methylammonium lead trihalide ($MAPbX_3$) has received increasing attention as an absorber material for perovskite solar cells. However, it was found that the stability of $MAPbX_3$ strongly varies depending on temperature, changing phase or crystal orientation. The structural data of methylammonium lead trihalides ($MAPbX_3$; X=I, Cl, Br) [53,54] is summarized in Table 1. As depicted in Table 1, both $MAPbBr_3$ and $MAPbCl_3$ crystallize in the cubic phase at room temperature while $MAPbI_3$ should be heated to >323 K at which point the phase transition from a tetragonal to a cubic phase takes place. Interestingly, many studies on $MAPbI_3$ materials report that the tetragonal phase of $MAPbI_3$ still exists even after heating to 373 K [21,20,55,56,57]. This suggests that the tetragonal phase is surprisingly stable in the thin films but also points out an

ambiguity about the exact phase transition temperature and the nature of the phase transition between the tetragonal and cubic phases.

TABLE 1

STRUCTURAL DATA FOR METHYLAMMONIUM LEAD TRIHALIDES [52]

| Halides (X) | Temperature (K) | Crystal structure | Space group | Lattice parameter (Å) | | |
|---|---|---|---|---|---|---|
| | | | | a | b | c |
| Cl | >178.8 | Cubic | *Pm3m* | 5.675 | | |
| | 172.9–178.8 | Tetragonal | *P4/mmm* | 5.656 | | 5.630 |
| | <172.9 | Orthorhombic | *P222₁* | 5.673 | 5.628 | 11.182 |
| Br | >236.9 | Cubic | *Pm3m* | 5.901 | | |
| | 155.1–236.9 | Tetragonal | *I4/mcm* | 8.322 | | 11.832 |
| | 149.5–155.1 | Tetragonal | *P4/mmm* | 5.894 | | 5.861 |
| | <144.5 | Orthorhombic | *Pna2₁* | 7.979 | 8.580 | 11.849 |
| I | >327.4 | Cubic | *Pm3m* | 6.329 | | |
| | 162.2–327.4 | Tetragonal | *I4/mcm* | 8.855 | | 12.659 |
| | <162.2 | Orthorhombic | *Pna2₁* | 8.861 | 8.581 | 12.620 |

***Air stability***

The impact of environmental factors such as moisture, water, humidity, and UV light are undeniable in the performance and stability of organic-inorganic halide perovskites. The degradation from $CH_3NH_3PbI_3$ to $PbI_2$ is most likely accompanied by a release of gases via simple sublimation or assisted chemical reaction. It is proposed that the first mass loss step during the degradation of $CH_3NH_3PbI_3$ and $CH_3NH_3I$ under an inert atmosphere proceeds as [39]:

$$CH_3NH_3PbI_3 \text{ (s)} \xrightarrow{H_2O} CH_3NH_3I \text{ (aq.)} + PbI_2 \text{(s)} \qquad (7)$$

$$CH_3NH_3I \text{ (aq.)} \rightarrow CH_3NH_2 \text{(aq.)} + HI \text{ (aq)} \qquad (8)$$

$$4HI \text{ (aq.)} + O_2 \text{(g)} \rightarrow 2I_2 \text{ (g)} + 2H_2O \text{ (l)} \qquad (9)$$

$$2HI \text{ (aq.)} \rightarrow 2H_2 \text{ (g)} + I_2 \text{ (s)} \qquad (10)$$
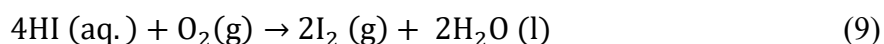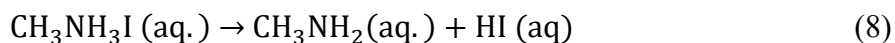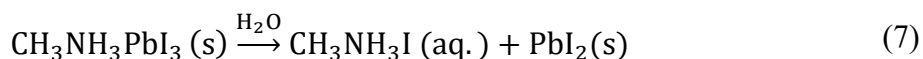
As shown in Eq. (7) - (10), in the presence of moisture, MAI dissolves leaving inorganic lead halide, and subsequently MAI continue the hydrolysis and release HI. The decomposition is irreversible with the existence of moisture. Dao et al. showed the stability of the perovskite layer before and after air exposure. The study revealed that the original MAPbI$_3$ film has a pinhole free large grain of 5µm. However, after exposure in the air for 18h, there are voids inside the grain which are mainly volatile gases of H$_2$ and I$_2$. Large grains are converted into small grains when exposed to air for 18 hours. Studies have shown that humidity also plays an important role in the performance of perovskite solar cells. Kelly et al. showed that the increase in relative humidity (RH) from 50% to 80% in the N$_2$ environment dramatically reduced the absorption affecting the photo conversion efficiency. They suggested that use of a proper hole transport layer could reduce the degradation. Encapsulation of a perovskite based solar device is necessary to protect it from moisture induced degradation. The organic charge transport layers are proven to be susceptible to air exposure; therefore, researchers replaced these organic transport layers with inorganic materials such as CuSCN, CuI and NiO$_X$ as the hole transport layers and ZnO$_2$ and TiO$_2$ as the n-type transport layers [58]. You et al. showed improved stability in the presence of moisture and air by implementing p-type NiOx and n-type ZnO nanoparticles as hole and electron transport layers, respectively. The device could retain almost 90% of the original efficiency after 60 days of exposure in air under room temperature [58].

### *Thermal stability*

Typically, device temperatures can increase up to 45 °C higher than ambient temperatures when solar cells operate under direct sunlight. According to International Standards (IEC 61646 climatic chamber tests), long-term stability at 85 °C is required in order to compete with the silicon-based technology [59]. Therefore, the study of thermal stability of perovskite solar devices

have attracted attention of researchers all over the world. Different degradation pathways have been proposed, and the topic is still under debate, but it is clear that MAPbI$_3$ (CH$_3$NH$_3$PbI$_3$) perovskite loses its excellent light harvesting properties over time because it evolves into PbI$_2$ after a nominal loss of CH$_3$NH$_3$I.

Several studies have been reported corresponding to the thermal stability of the perovskite absorber layer in the PSCs. Conings, et al. investigated the thermal stability of perovskite solar cells, with a structure of ITO/TiO$_2$/MAPbI$_3$ [59]. The hole transfer layer (HTL) and top electrode were omitted to isolate the perovskite layer degradation from degradation at other interfaces. The samples were heated at 85 °C for 24 h, under four environmental conditions: pristine film (reference), O$_2$ environment, N$_2$ environment and ambient conditions. The study revealed the formation of PbI$_2$ under ambient conditions.

In their work, Han, et al. [60] tested the stability of perovskite solar devices in an environmental chamber, where the temperature was controlled in the range of -20 °C to 100 °C. The actual cell temperature inside the chamber was found to be approximately 30 °C higher than the environmental temperature. Hence, the temperatures were denoted as "environmental temperature (actual cell temperature)", e.g., 55 °C (85 °C) [60]. The degradation mechanism of CH$_3$NH$_3$PbI$_3$ solar cells were analyzed for 500h at 55 °C (85 °C) using cross- sectional focused ion beam–scanning electron microscopy (FIB-SEM). The cross-sectional FIB-SEM images shown in Fig. 11 revealed the degradation mechanism of an encapsulated device. The direct exposure to one sun illumination clearly damaged the entire device with the most degradation observed in the silver layer. A number of degradation features were observed in the degraded cells, which include degradation of the silver layer, formation of voids in spiro-OMeTAD and the perovskite layer, and detachment of the perovskite layer from the TiO$_2$ layer. In addition, new particles with high atomic

number were observed in the perovskite layer. It is anticipated that the degradation was initiated by the reaction of HI gas and Ag in an encapsulated device structure. Therefore, the authors suggested replacing the silver contact and using highly heat-resistant encapsulating materials.
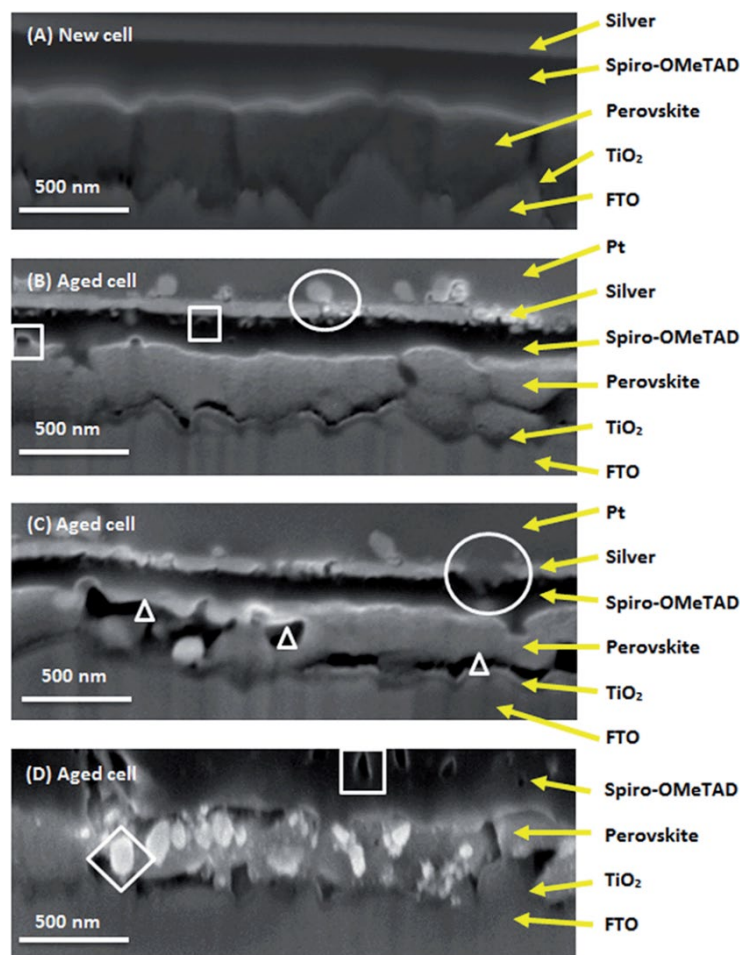


Fig. 11.  (A) Cross-sectional FIB-SEM images of a new cell and (B-D) different areas of the aged cell at constant temperature (55 °C (85 °C)) and humidity (50%) for 500 h. Degradation features are denoted as follows: voids in the Spiro-OMeTAD layer (□); voids in the perovskite layer (Δ);

degraded silver layer (○) and formation of particles with higher atomic numbers, likely PbI2 (◊).
Reprinted with permission from [60].

Several techniques have been utilized to achieve thermally stable perovskite solar cells. One approach includes the use of polymers such as poly(methyl methacrylate) (PMMA), polycarbonate (PC), polystyrene to protect perovskite films from oxygen and moisture [62]. Along with protection from air, polymers act as insulating tunneling contact and passivates defects in perovskite film by increasing efficiency by more than 18% [61]. Habisreutinger, et al. [62] proposed a device architecture composed of single-walled carbon nanotubes for selective charge extraction and an encapsulating polymer matrix such as PMMA or PC to protect the device from moisture ingress. The devices remained stable in ambient humidity conditions at elevated temperatures of 80 °C, while control devices degraded rapidly. Another approach to improve thermal stability is substituting the methylammonium (MA) cation of the perovskite material. Mixed cation-based perovskites have been extensively studied by researchers. Enhanced crystallinity and structural stability with improved power conversion efficiency were obtained by replacing MA with formamidinium (FA) [26,63,64], cesium (Cs) cations, [65,66,67,68] or a mixture of the two [69,70,71,72,73,74]. Several groups have reported on Cs/FA mixtures, with enhanced stability in light, moisture, and heat compared to the pure one ($FAPbI_3$). Saliba, et al. have fabricated solar cells using quadruple-cation perovskites (MA/FA/Cs/Rb), also revealing improved reproducibility and stability [75]. Saliba, et al. tested aged devices for 500 hours at 85°C under continuous illumination with full intensity and maximum power point (MPP) tracking in a nitrogen atmosphere. The current-voltage characteristics of the best performance solar cells and the EQE electroluminescence (EL) are shown in Fig. 12 (a)-(c). This compounded stress test

exceeds industrial standards [76]. They showed that the device retained 95% of its initial performance when heated at 85 °C for 500 hours, as shown in Fig. 12(d).
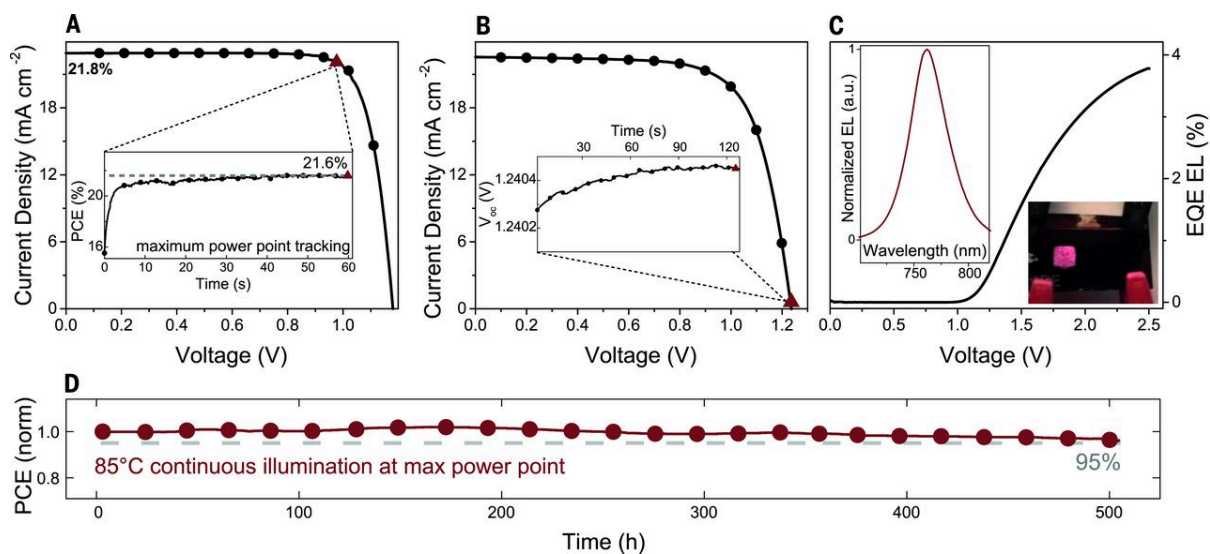


Fig. 12. (A) Current density–voltage (J-V) curve of the best performed RbCsMAFA solar cell. The inset shows the scan rate–independent maximum power point (MPP) tracking for 60s. (B) J-V curve of the highest-$V_{OC}$ device. The inset shows the $V_{OC}$ over 120s (C) EQE electroluminescence (EL) as a function of voltage. The left inset shows the corresponding EL spectrum over wavelength. The right inset shows a solar cell. (D) Thermal stability test of a perovskite solar cell. Reprinted with permission from [28].

**2.6.2 Stability of other layers**

The stability of other components such as electron transport layer (ETL), hole transport layer (HTL), and metal electrode also play an important role in the performance and stability of PSCs.

***Electron transport layer (ETL)***

The most commonly used ETL in perovskite solar devices is titanium dioxide ($TiO_2$). However, non-stoichiometric defects, such as oxygen vacancies and titanium interstitials can form in this layer [77] and cause deep sub-band gap trap states. Perovskite devices with $TiO_2$ ETL showed rapid degradation under illumination. Recently, Ahn, et al. showed that compact $TiO_2$-based perovskite solar cells completely decomposed only after 6 hours [78]. As evidenced by the SEM images, degradation is initiated at the perovskite/$TiO_2$ interface in the $TiO_2$-based device. The authors postulated that the trapped charges at the interface were responsible for the irreversible degradation of perovskites along grain boundaries [78]. To enhance stability, compact $TiO_2$ ETL can be replaced with $C_{60}$, which showed much more stable performance when deployed in the device structure. Wojciechowski, et al. used $C_{60}$ as an interface modification layer for $TiO_2$ and as a stand-alone electron-accepting layer [79,80].

***Hole transport layer (HTL)***

The most commonly used hole transport layer in the inverted perovskite device structure is poly(3,4-ethylenedioxythiophene) polystyrene sulfonate (PEDOT:PSS). However, the prime disadvantage of the PEDOT:PSS based hole transport layer (HTL) is that it leads to the chemical instability of perovskite solar devices due to its acidity and highly hygroscopic nature [81,82,83]. In addition, Vitoratos, et al. [84] investigated the thermal stability of PEDOT:PSS as the most popular hole transport material in an organic semiconductor. The study revealed that the electric

conductivity of perovskites decreased with aging owing to the shrinkage of PEDOT conductive grains. Moreover, the XPS and UPS measurements suggested a broken conformational PEDOT:PSS structure, which results in the thermal instability of this material [84]. A recent study [85] showed improved efficiency and stability of perovskite solar cells with traditional PEDOT: PSS HTLs. They fabricated PEDOT:PSS monolayers by spin coating, and then ultrapure water was used to wash away most of the PEDOT:PSS, constructing an ultra-thin layer of PEDOT:PSS. The water rinsed device sustained more than 50% of its stability, which is attributed to the less hygroscopic nature of the thin PEDOT:PSS layer [85]. Another approach is to use an oxide-based hole transporting material such as NiO, which was found to exhibit better air [58,86,87] and thermal stability [37].

### *Metal electrodes*

The most commonly used electrode for high efficiency perovskite solar devices is gold (Au) or silver (Ag) [38,88,89]. Gold is very expensive and can be typically replaced by Ag paste as an electrode in perovskite solar cells [90]. However, it has been reported that both Ag and Au show degradation when exposed to thermal stress [91,92]. Domanski, et a*l*. reported the migration of gold through HTL into the perovskite materials at 70 °C [92]. Li, et al. showed that in an inverted perovskite solar cell (PSC), ions migrated from MAPbI$_3$ thin film diffused through the PCBM ETL and accumulated at the Ag surface in N$_2$ at 85 °C [93]. They showed that the loss of MAI occurred at grain boundaries (GBs) and upon thermal heating, AgI, MA$^+$, and I$^-$ ions migrate to reconstruct the GBs, creating more defects in both the bulk grains and the MAPbI$_3$/PCBM interface. Multiple reports have investigated an alternative to Au and Ag based electrodes by employing carbon as a back-contact material [48,94]. Li, et al. [48] fabricated a hole-conductor-free PSC based on a triple layer architecture with printed carbon electrode. The device structure displayed excellent stability.

An encapsulated device showed stable performance during outdoor operation for seven consecutive days in Jeddah, Saudi Arabia. Moreover, the encapsulated device remained thermally stable when heated at 80–85 °C for 90 days, in the dark. The use of carbon as a back-contact can be beneficial to make stable PSCs at an elevated temperature of 100 °C, which represented one-step forward to the commercialization of PSCs [95].

### 2.6.3 I-V Hysteresis

The hysteretic current-voltage, I−V behavior between forward (lower voltage → higher voltage) and reverse scan (higher voltage → lower voltage) during current-voltage characterization presents a challenge for determining the accurate power conversion efficiency of the PSCs. Generally, the reverse scan displays higher PCE than the forward scan, which means the reverse scan and the forward scans display a mismatch in the efficiency of the PSCs [96,97,98]. The I-V hysteretic behavior of PSCs depends on many parameters such as scan rate, voltage range, scan direction, and configurations of PSCs [36,99,100,101,102,103,104]. The scan rate is one of the crucial parameters in hysteresis analysis since with increasing scan rate the hysteresis increases, and the hysteresis can be removed using a slower scan rate [36,99,100,101]. The PV performance as well as the hysteresis is also affected by scan range with different initial bias voltages[103,105]. McGhee et al. reported that the light soaking has a great impact on the photovoltaic performance by increasing FF and short-circuit current density upon light soaking with large positive bias voltage, while light soaking with large negative bias voltage showed negative impact on the PV performance. The anomalous I−V hysteresis behavior has been observed in a variety of PSCs irrespective of their device architecture including p-i-n & n-i-p structure where Spiro-OMeTAD

and TiO$_2$ layers are used as an p- and n- type contacts in p-i-n cells; while PCBM and PEDOT:PSS layers are used as an n- and p-type contacts in n-i-p cells [106,107,108,109].

The origin of I-V hysteresis has been reported to be due to ferroelectric polarization of the perovskite layer [103,110], charge accumulation at the interfaces due to trapping and de-trapping [111,112,113,114], and ion migration of related defects under applied bias [115,116]. The slow decay process of the capacitive charging or discharging during I-V characterization is attributed to cause non steady-state photocurrent and hysteresis [100]. The non-steady state photocurrent, due to capacitive charging or discharging, results in electrode polarizations at perovskite and electrode interfaces, which influences the hysteresis. However, the PV performance after light soaking with different bias voltages cannot only be explained with the capacitive effect. The modified steady-state current due to band bending, instead of capacitive effect could be the reason behind the change in the PV performance. The origin of band bending is due to trapped charges, ion migrations, or ferroelectric polarization. The extraction efficiency of electron and hole contributes to the observed hysteresis behavior. The extraction efficiency is influenced by the charge trapping and detrapping process at the interface, and grain boundaries and enhancing charge extraction is vital for controlling hysteresis. The partially trapped states at the interfaces create a depletion region at the HTL/Perovskite and ETL/Perovskite interfaces. This leads to change in the band structure and reduces charge extraction under forward bias condition. Under large forward bias, trap states can be filled, which reduces the depletion region and the band bending. The trapping and detrapping process of charges thus affects the hysteresis behavior in PSCs. Accumulation of ions occur at interfaces near the electrodes due to ion migration, and an electric field is generated. This ion migration is considered another cause of band bending, which influences the separation and extraction of photogenerated charges. Ferroelectric polarization is another possible cause to

modulate the electric field distribution, resulting in different PV performance under reverse and forward scan.

**2.6.4 Toxicity**

The toxicity of perovskite originates from the widely used lead as metal cation in the perovskite compound. Therefore, environmental and health hazards would be a major concern in large-scale manufacturing of these emerging solar cells. Studies have shown that contamination from perovskite can be considered insignificant compared to other sources of lead waste [117]. However, many researchers have been investigating the possibility and outcome of lead-free PSCs. The first candidate to replace lead (Pb) was tin (Sn) since both are carbon periodic materials and are thus expected to have similar crystal structure. However, as shown by Noel et al. [118], $Sn^{2+}$ can easily oxidize to $Sn^{4+}$ leading to poor device performance of tin based PSCs. Other reports showed that the hybrid Sn-Pb metal cations in perovskite could reduce the toxicity of lead to some extent as well as have advanced PCE [119]. A remarkable PCE of 15.2% with a light absorber of $MASn_{0.25}Pb_{0.75}I_3$ was reported by Zhu et al. [120].

In addition to Sn, Bismuth (Bi) was studied as a replacement for lead. It provided a stable $(MA)_3Bi_3I_9$ (MABI) perovskite material. However, the first reported MABI-based PSC only reached a low efficiency of 0.12% with a relatively low $V_{OC}$ of 0.68 V and an extremely low $J_{SC}$ of 0.52 mA/cm$^2$ [121]. At present, the Bi-based PSC is still not promising even compared with Sn. Several other types of lead-free perovskites such as $CsGeI_3$ [122], $MAGeX_3$ (X: Cl, Br, I) [123], $MASrI_3$ [124], $MACaI_3$ [125] had also been reported; however, most of the PSC showed low efficiency of less than 1%. Moreover, these materials are not suitable for visible light

absorption due to large bandgap [119]. Hence, an established lead-free perovskite solar cell has a long way to go for development and needs extensive study.

## 2.7 Summary

In this chapter, the structure and properties of perovskite materials are summarized. In addition, the operational principle of perovskite solar devices as well as the evolution device architecture are described. Moreover, the major drawbacks of perovskite solar cells such as air and thermal stability are discussed with possible solutions that have been adopted by researchers. In this thesis, our focus is to overcome the thermal instability of perovskite solar cells and establish stable perovskite solar cells. The following chapter illustrates the experimental methods used throughout this thesis.

# CHAPTER 3

# EXPERIMENTAL METHODS

## 3.1 Perovskite precursor preparation

The perovskite ($CH_3NH_3PbI_{3-x}Cl_x$) precursor was prepared by mixing lead iodide ($PbI_2$, Sigma-Aldrich, 99%) and methylamine hydrochloride (MACl, Sigma-Aldrich) at a ratio of 1:1 before adding N, N-dimethylformamide (DMF, Sigma-Aldrich, anhydrous, 99.8%) to get 11wt% concentration. The solution was stirred overnight in a glove box at 70 °C.

The perovskite ($CH_3NH_3PbI_3$) precursor solution was prepared by dissolving an equimolar ratio of methylammonium iodide (MAI, Greatcell Solar) and lead iodide ($PbI_2$, Sigma-Aldrich, 99%) dissolved in 11 wt% N,N-dimethylformamide (DMF, Sigma-Aldrich, anhydrous, 99.8%) concentration. To fabricate Cs-doped perovskite ($Cs_xMA_{1-x}PbI_3$), the precursor solution was prepared with the three concentrations of cesium iodide (CsI) (x=5%, 9%, and 20%) and stirred overnight at 70 °C.

## 3.2 Perovskite solar cell fabrication

Perovskite solar devices were fabricated using the p-i-n structure of FTO/ $NiO_x$ (or PEDOT:PSS)/ $MAPbI_3$ (or $MAPbI_{3-x}Cl_x$ / $CsMAPbI_3$)/ C60 (or PCBM)/ C60:C/ Ag. The perovskite absorber layer was fabricated using two different approaches: hot-casting and antisolvent method. The fabrication methods of two different approaches of the perovskite layer, different hole and electron transport layers are explained in detail in the following sections of this chapter.

**3.2.1 Transparent electrode FTO preparation**

Patterned FTO (SnO$_2$/F, ~8 Ω/sq-1, Aldrich) substrates were cleaned using mucosal, de-ionized water, methanol, acetone, and iso-propanol (IPA) sequentially. Each solution was heated at 100 °C and then put into an ultrasonic bath for 10 minutes to clean the substrate. The substrate was then dried with nitrogen and heated at 120 °C for 20 minutes to completely evaporate all residues.

**3.2.2 Hole transport layer (HTL) deposition**

A NiO precursor was prepared by mixing 50 mg of NiO (Sigma-Aldrich) with 3 mL of HCl (Alfa Aesar, 36%) and stirring overnight at 75°C inside a fumehood. After mixing, the solution was filtered by a 0.45 μm filter. The NiO thin film was prepared using a hot-casting technique. For that, FTO substrates were kept at different hot-casting temperatures ranging from room temperature to 120 °C. The prepared NiO precursor solution was then immediately deposited on the hot substrate by spin coating at 2000 rpm for 60 s in order to maintain the substrate temperature. NiO thin film was then heated to 350 °C for 15 minutes.

In the case of PPEDOT:PSS, PEDOT:PSS was diluted by using 2-propanol in a ratio of 1:3 and was spin coated on FTO/glass substrates at a speed of 3000 rpm. PEDOT:PSS was heated on a hot plate for 15 minutes at 150 °C.

**3.2.3 Active layer of perovskite deposition**

The perovskite film was fabricated using 2 different techniques. First, the hot-casting technique was applied to fabricate perovskite thin film on pre-cleaned FTO substrates. In this

process, the precursor solution and substrate temperature were kept at 70 °C and 180 °C, respectively. The perovskite precursor solution was then immediately spin-coated on the hot FTO substrates at 4000 rpm for 10 s.

For the antisolvent approach, the perovskite precursor solution was prepared by dissolving an equimolar ratio of $PbI_2$ : MAI :DMSO (1:1:1) in DMF. The solution was stirred overnight inside a glove box at 70 °C. The solution was cooled down to room temperature before spin coating in a fumehood. 0.1 ml of the perovskite solution was dropped on the FTO/NiO substrate and spin-coated using dynamic spin speed. The first spin speed is 1000rpm for 10s, and the second one is 5000rpm for 30s. At 10s of the second spinning cycle, 0.5 ml antisolvent (diethyl ether) was dropped on the rotating sample. The films were then annealed at 100 °C for 10 minutes in air on a hot-plate.

### 3.2.4 Electron transport layer (ETL) deposition

The electron transport layer consists of PCBM (Nano-c) dissolved in di-chlorobenzene (Sigma-Aldrich) and was spin coated onto the perovskite film in a nitrogen filled glove box at 1250 rpm. Then C60 and carbon were depoisted in electrom beam evaporation. PCBM, C60, and carbon layers were measured to be about tens of nanometers.

### 3.2.5 Cathode electrode deposition

Finally, silver was deposited in electron beam evaporation at a deposition rate 4 angstrom/s. The thickness of the Ag metal was about 180 nm.

## 3.3 Polymer preparation

For the deposition of PMMA, PMMA (Sigma-Aldrich, $M_w$ ~120 000) was dissolved in chlorobenzene (Sigma-Aldrich, 99.5%) (10mg/mL) and spin-coated on top of the perovskite film with a spin speed of 4000 rpm for 10 s.

Polyimide was dissolved in chloroform (20mg/ml) and spin coated on top of perovskite solar cells with a spin speed of 3000 rpm for 10s under a nitrogen environment inside a glove box.

## 3.3 Electrical characterization

### 3.3.1 Current-voltage characteristics (J-V)

The photocurrent density (J) vs voltage (V) curves were determined using a Keithley 2400 source meter under AM 1.5G illumination at $100mW/cm^2$ provided by a solar simulator (Newport 69907). One sun illumination was adjusted using NREL-calibrated, KG-2 filtered Si diode. A 450 W Xenon lamp was used as the light source, and the lamp remained on for 30min before starting the photocurrent measurement to stabilize the light intensity. J–V curves were obtained by scanning from -0.05V to 1V. Temperature-dependent J-V measurements were carried out following the identical procedure and keeping all conditions the same as temperature-dependent PL and TRPL measurements. $N_2$ atmosphere was provided to protect the sample from moisture during temperature-dependent J-V measurements.

**3.5 Optical characterization**

**3.5.1 Steady state and time resolved photoluminescence (PL) measurement**

Perovskite samples were prepared on glass substrates to attain optical characterization of steady-state and time-resolved PL. The cleaning steps of glass substrates and the deposition procedure of the perovskite layer were the same as mentioned for the perovskite solar cells. To prevent degradation by air exposure, samples were coated using a polymer, polymethyl-methacrylate (PMMA, Sigma-Aldrich, Mw~120,000) in chlorobenzene (Sigma-Aldrich, 99.5%) (10 mg/ml) at 2000 rpm for 30s. Steady-state and time-resolved PL spectra were recorded using spectrophotometer (Flurolog, Horiba Jobon Yvon) and time-correlated single photon counting (TCSPC) system connected with a solid-state laser. For PL measurement, an excitation wavelength of 450nm with 20MHz repletion rate was used, and the emission spectra were measured from 600 nm to 850 nm. For time-resolved PL (TRPL), a high-speed photomultiplier tube detector (FL-1073, Horriba scientific Inc) was employed for photon counting with repetition rate of 4MHz and 450nm excitation wavelength. Both PL and TRPL measurements were performed at a very low excitation density of 0.2 $\mu W/cm^2$ to avoid possible degradation by laser. For temperature-dependent PL and TRPL measurements, a THM S600E Linkam temperature control stage with 0.1 °C accuracy was used. To passivate the defects in the perovskite film, 20 min light soaking was applied at room temperature before undertaking the measurement. The temperature-dependent measurement was conducted over thermal cycles of 28-82-28 °C. In the heating and cooling processes, the temperature was increased and decreased respectively at a step size of 1 °C, and a waiting time of 2min was maintained at each temperature in order to hold the sample at an assigned temperature. During the temperature-dependent measurement, cool water was circulated using a Linkam ECP water circulation pump to control the temperature precisely.

**3.5.2 UV-vis measurements**

The UV-VIS spectra were measured by using a Perkin Elmer Lambda 45 spectrophotometer. To measure UV-VIS, an active layer of perovskite was prepared on top of a glass substrate.

**3.5.3 IR nanoscopy measurement**

Nano IR absorption spectrum, morphology, and absorption mapping image of the perovskite film were obtained using infrared nanoscopy (IR nanoscopy) (Anasys Instruments, CA, USA) under an ambient condition. The IR nanoscopy system is combined with a high-resolution AFM operating in contact mode to simultaneously measure morphology and absorption spectra with a spectral range of 900 to 2000 cm$^{-1}$.

**3.6 Structural and morphological characterization**

**3.6.1 X-ray diffraction measurement**

X-ray diffraction was measured on a solar cell device using a Rigaku MiniFlex II X-ray diffractometer. The solar cell device was heated in the N$_2$ atmosphere at different temperatures using the THM S600E Linkam system. An acquisition rate of 5 °/min with a step size of 0.02 ° was used.

**3.6.2 Scanning electron microscopy (SEM) and energy dispersive X-ray spectroscopy (EDS) measurement**

The surface morphology and EDS mapping of the perovskite film was characterized by scanning electron microscopy (SEM; JEOL, JSM-6060LV). Images were taken at different magnifications and at an accelerating voltage of 15kV. Samples for SEM/EDS were prepared by Au coating with a Hummer V sputter coater for preventing electron charging.

**3.6.3 Nuclear magnetic resonance measurement**

The high-resolution proton NMR spectra were taken on a JEOL 400 MHz spectrophotometer. For NMR measurement, deuterated DMSO was used as a solvent. The $CH_3NH_3PbI_3$ solution is prepared by mixing 0.009g $CH_3NH_3I$ and 0.027g $PbI_2$ in 0.3mL deuterated DMSO and stirred at 60 °C for 12 hours. The PMMA solution is prepared by dissolving 0.003mg PMMA in 0.3mL deuterated DMSO. $CH_3NH_3PbI_3$ solution mixed with PMMA is prepared by adding 0.009g $CH_3NH_3I$, 0.027g $PbI_2$, and 0.003mg PMMA in 0.3mL deuterated DMSO.

**3.7 Summary**

The preparation of the perovskite precursor solution and the fabrication method of the perovskite film and perovskite solar cells with different charge transport layers were described in this chapter. In addition, characterization techniques such as PL, TRPL, J-V, SEM, EDS, XRD, UV-vis, and NMR used in this thesis are depicted in this chapter.

**CHAPTER 4**

**DEGRADATION MECHANISM of PEROVSKITE FILM AND SOLAR CELL DURING**

**HEATING AND COOLING TEMPARATURE CYCLE**

**4.1 Introduction**

The organo-inorganic halide perovskite has evolved rapidly into the most important new candidate for next-generation photovoltaics in an unprecedentedly short period of time [32,126,127,128]. During the past few years, refined fabrication processes of perovskite solar cells, improved understanding of solar cell physics, and innovative device engineering have led to significant progress and much improved cells that operate at greater than 20% efficiencies [8]. Despite all these advances, the instability of organometal halide perovskite solar cells [127,59,129,130,131] has been a major obstacle to commercial viability. Either $CH_3NH_3PbI_3$ ($MAPbI_3$) or $CH_3NH_3PbI_{3-x}Cl_x$ ($MAPbI_{3-x}Cl_x$) have been widely studied for photovoltaic applications, which displays a distorted three-dimensional network [132]. From a chemical point of view, the perovskite material is composed of complicated chemical structures in the $ABX_3$ coordination, in which the A cation is composed of $CH_3NH_3^+$ (or $MA^+$), the B metal cation is divalent metal ion of $Pb_2^+$ while the X anions are halides including $Cl^-$ and $I^-$. As predicted by theoretical frameworks, the optoelectronic properties of perovskites will be in part governed by $CH_3NH_3^+$ organic moiety, the Pb-X (X=Cl and I) bonds and their chemical configurations [133]. Therefore, the chemical distortion or rupture induced by decomposition or degradation of perovskite films will inevitably alter the optoelectronic properties of solar cells. Indeed, recent studies

demonstrated that the presence of moisture accelerated the chemical decomposition from the dark brown $MAPbI_{3-x}Cl_x$ to yellow $PbI_2$ when the perovskite layer was not properly encapsulated. In addition, Zhou et al. [127] demonstrated an 80% decline of photovoltaic performance of unencapsulated perovskite solar cells when stored in ambient conditions for 24 hrs at room temperature, which highlights the importance of an advanced encapsulation technique. Given these problems, considerable efforts have been devoted to employing the encapsulation layers as a means of protecting the underlying perovskite film. Nevertheless, studies revealed that perovskite films are inherently unstable and highly sensitive to the temperature even in an inert environment [129]. In particular, Conings et al. systematically investigated thermal instability of $MAPbI_3$ from a morphological, electronic and chemical point of view. Their investigation concluded that perovskite film is not intrinsically stable but gradually disintegrates from $MAPbI_3$ to $PbI_2$ with loss of $CH_3NH_3I$ when heated to 85 °C even in inert atmosphere. Deretzis et al. [130] also made similar observation of thermal instability of $CH_3NH_3PbI_3$ which transformed to $PbI_2$ at 150 °C under vacuum. Most strikingly, in-situ high-resolution transmission electron microscopy (TEM) and electron energy loss spectroscopy showed the thermal degradation of perovskite films even at $\sim50-60$ °C [131].

Although there is some understanding of the thermal instability of perovskite solar cells, little is known about the impact of thermal instability on the reversible or irreversible behaviour of perovskite solar cells. At present, studies on the thermal instability of perovskite solar cells have been conducted at specific temperatures for a specific period of time [127,129,130,131]. However, it should be noted that device temperatures can increase up to 45 °C higher than ambient temperature under direct sunlight which also varies

depending on the time of day and the time of year [60]. As a result, the device operating temperature fluctuates from low to high or vice versa, depending on ambient temperatures. In this work, we conducted a quantitative and systematic investigation of pathways for thermal degradation and their impacts on device operation during a heating and cooling temperature cycle between room temperature and 82 °C. Most surprisingly, it is revealed that the irreversible degradation of perovskite solar cells was triggered at 70 °C in a nitrogen environment. Another intriguing observation is that the degradation momentum of the perovskite solar cell did not stop but continued even when the device temperature cooled down from 82 °C, close to a solar cell's field operating temperature to room temperature. Our new finding infers that the instability of perovskite solar cells at such a low temperature under illumination may limit their real field commercial applications.

## 4.2 Temperature-dependent photovoltaic performance of perovskite solar cells during heating and cooling processes

Perovskite solar cells were fabricated having the device structure of FTO/PEDOT:PSS/MAPbI$_{3-x}$Cl$_x$ /PCBM/carbon/Ag, as shown in Fig. 13 (a). In this study, photoactive MAPbI$_{3-x}$Cl$_x$ perovskite film was prepared using a hot casting technique in which a hot (70 °C) perovskite solution was spin-coated onto FTO/PEDOT: PSS substrates maintained at 180 ° C. A precursor solution of MAPbI$_{3-x}$Cl$_x$ was prepared by dissolving an equimolar ratio of PbI$_2$ and CH$_3$NH$_3$Cl (MACl) in N, N-dimethylformamide in a concentration of 11wt%. Unlike conventional spin-casting methods, this hot-casting technique produces uniform, pinhole-free perovskite morphologies, as shown in Fig. 13 (b). As an electron transport layer (ETL), combined PCBM/carbon was utilized. In previous studies, we have found that the deposition of carbon on

top of PCBM resulted in improved series and shunt resistances of perovskite solar cells. In particular, a 10 nm thick carbon film led to high conductivity ($\sigma$=4.24±0.68 Scm$^{-1}$) that is much better than reported conductivity of C60 (2.4×10$^{-3}$ Scm$^{-1}$) and PCBM (3.2 ×10$^{-4}$ Scm$^{-1}$). Fig. 13 (c) shows current (J)-voltage (V) characterization of MAPbI$_{3-x}$Cl$_x$ solar cells with PCBM/carbon ETL. Short-circuit current (J$_{SC}$), open circuit voltage (V$_{OC}$) and fill factor (FF) were 23.69 mA/cm$^2$, 0.96 V and 0.71, resulting in a power conversion efficiency (PCE) of 16.2%. [9]
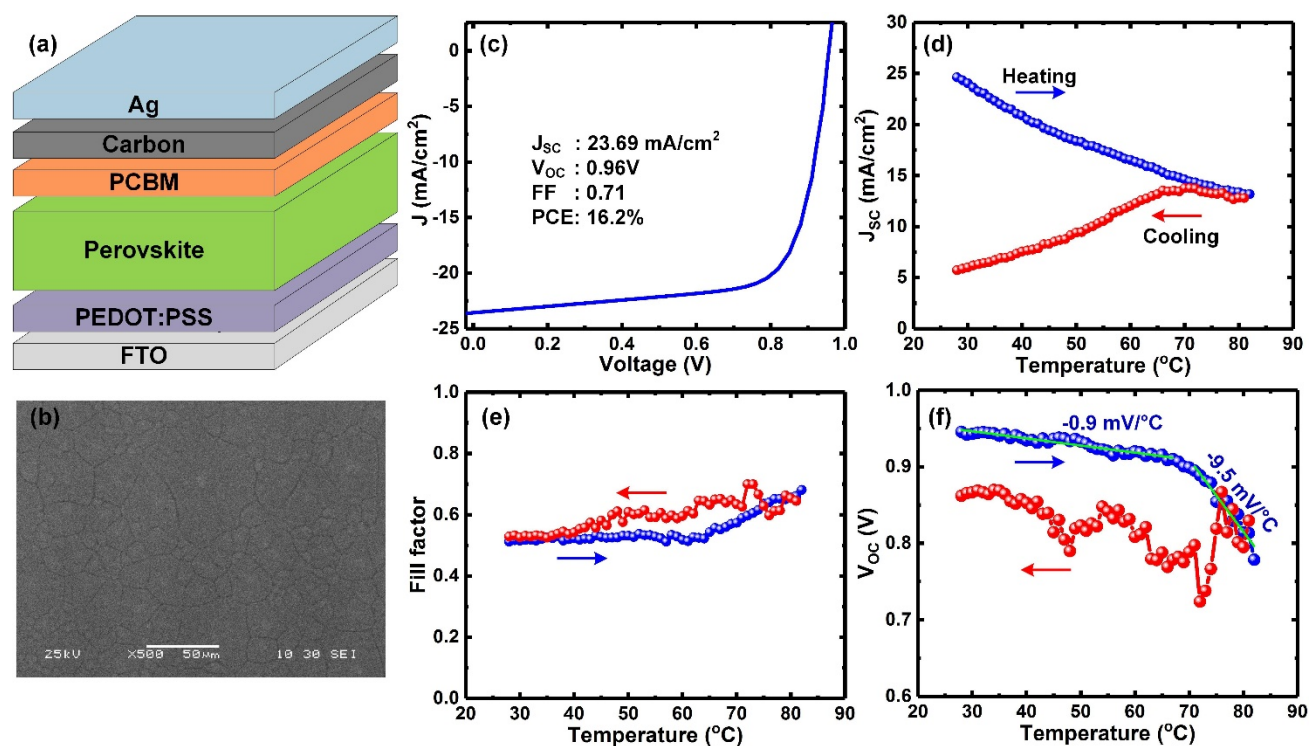


Fig. 13. (a) Inverted p-i-n perovskite solar cell structure and (b) SEM image of perovskite film fabricated by a hot-cast technique. (c) Current-voltage J-V characteristic of perovskite solar cell at room temperature exhibited a PCE of 16.2% at room temperature. However, after soldering

electrodes to the electrical connectors of the THM S600E system, photovoltaic parameters of perovskite solar cell changed slightly, and the initial efficiency dropped to ~13%. Also, the evolution of photovoltaic parameters of (d) short circuit current density ($J_{SC}$), (e) fill factor (FF) and (f) open circuit voltage ($V_{OC}$) of perovskite solar cell during the heating and cooling processes is illustrated. [9]

For temperature-dependent J-V measurements, $MAPbI_{3-x}Cl_x$ perovskite solar cell was placed in a nitrogen-filled Linkam THM S600E system while adjusting the temperature at 1 °C intervals for 2 min at each point before collecting data. In addition, cool water was circulated using a Linkam water circulation pump to control the temperature precisely. The device temperature was increased from room temperature to 82 °C and then cooled to room temperature. Fig. 13 (d)-(f) summarizes the temperature dependencies of the principal photovoltaic parameters ($J_{SC}$, $V_{OC}$ and FF) of the perovskite solar cell during the heating and cooling processes. We observed the irreversible performance of $J_{SC}$ and $V_{OC}$ during the heating and cooling processes. Upon increasing temperature, $J_{SC}$ in Fig. 13 (d) gradually decreased at a rate of approximately -0.18 mA/°C. In a cooling process, the decrease in $J_{SC}$ was also observed in which $J_{SC}$ initially increased but declined steadily. Remarkably, the $V_{OC}$ showed very strong temperature-dependent decline, as shown in Fig. 13 (f). As the temperature rises from room temperature to 70 °C, the $V_{OC}$ sharply decreased at a much faster rate of -9.5mV/°C. During the cooling process, the $V_{OC}$ steadily dropped from 82 °C to 70 °C and then slowly recovered as the temperature decreased to room temperature. [9]

**4.3 Temperature dependent steady-state PL**

It was recently demonstrated that increased charge trapping was considered one of the plausible causes responsible for the irreversible degradation of perovskite film. In this regard, we conducted temperature dependent, steady-state and time-resolved PL measurements on perovskite films to probe the evolution of carrier dynamics that determine photovoltaic performance during the heating and cooling processes. For temperature-dependent PL measurements, the MAPbI$_{3-x}$Cl$_x$ film was coated with PMMA to prevent degradation due to air exposure and placed in a nitrogen-filled Linkam THM S600E system. Fig. 14 shows temperature-dependent PL as a function of temperature and wavelength in a two-dimensional (2D) contour. Remarkably, from PL contour plots of heating and cooling processes in Fig. 14 (a) and (b), we noticed very low PL intensity in the cooling process. In addition, the integrated PL intensity in Fig. 14 (c) clearly shows irreversible PL behaviour during heating and cooling processes. Interestingly, at elevated temperatures, the integrated PL showed three distinct PL transition peaks at 40 °C, 54 °C and 70 °C on a logarithmic scale, as shown in Fig. 14. Obviously, the PL peak at 54 °C marked a tetragonal-cubic phase transition, while an unusual rise in PL from RT to 40 °C was also observed. Recently, it was assumed that the PMMA layer accumulates the pressure and temperature which cause phase transitions that occur at temperatures well below the theoretical predicted phase transition temperatures. However, tetragonal-cubic phase transition was clearly observed at 54 °C. Therefore, the peak at 40 °C is not related to tetragonal-cubic phase transition. However, it is assumed that unusual rise in PL might be related to light soaking effect. To verify this, we undertook two consecutive PL measurements by varying temperatures between RT and 50°C – below a tetragonal-cubic phase transition temperature, as shown
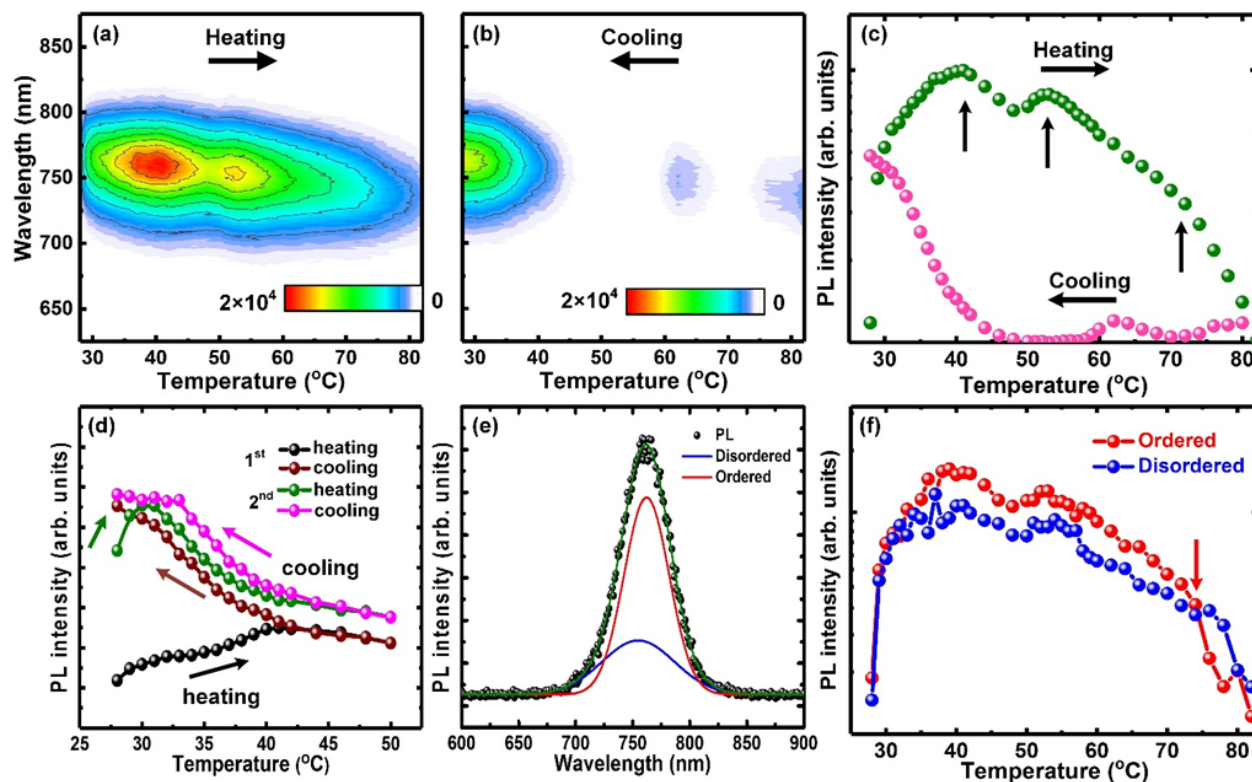
Fig. 14. Two-dimensional contour plots of PL during the (a) heating and (b) cooling temperature cycle. (c) Temperature-dependent PL intensity was re-plotted as a function of temperature clearly showing three transitional PL peaks during the heating process. (d) Consecutive PL measurements between room temperature and 52 °C were plotted during the heating and cooling processes. After the 1st thermal cycle was completed, the perovskite films were left in the dark for 30 min at room temperature and then the 2nd thermal cycle was conducted. (e) PL spectra were deconvoluted using the bi-Gaussian function for ordered (red) and disordered (blue) phases. (f) An evolution of deconvoluted PL intensities in a heating process is shown. [9]

in Fig. 14 (d). For the first heating and cooling process, a large discrepancy in PL was observed in which the PL intensity gradually increased to 40 °C and then decreased. However, for a second heating and cooling process, the PL intensity increased sharply and

continued to drop as the temperature increased. In addition, PL exhibited more reversible behavior during the second process. This might be a consequence of the light soaking effect at elevated temperatures. Indeed, Peng et al., reported that combined pre-light and heat exposure greatly enhanced the defect passivation of perovskite films. [9]

Another intriguing observation is a sharp decrease in PL intensity around 70 °C, a vital indicator of degradation of the perovskite film in Fig. 14 (c). As is well established, the collected PL spectra can be interpreted in terms of structural changes. In particular, structural degradation typically resulted in spectral broadening of PL, involving newly created defect states. Recently, our group reported a close correlation between chemical disorders and PL spectra of perovskite films using spatially and chemically resolved two-dimensional (2D) energy dispersive X-ray spectrometry (EDS) and PL mapping studies of the perovskite film. Our studies revealed that the PL spectrum observed in $MAPbI_{3-x}Cl_x$ perovskite thin film is asymmetric, which can be deconvoluted with a bi-Gaussian function, representing the ordered and disordered phases of the perovskite film. Critically, our chemical analysis of controlled morphologies revealed that non-stoichiometric chemical disorder led to a broad shoulder peak at the short wavelength while the stoichiometric perovskite grains showed a very uniform but longer wavelength. Fig. 14 (e) shows the deconvoluted PL spectra at room temperature, one with a broad full-width at half maximum (FWHM=74.9 nm) but shorter wavelength (754.9 nm) and the other with a narrow FWHM (46.7 nm) but longer wavelength (762.2 nm). Using a deconvoluted PL approach, we quantitatively analysed the evolution of the ordered and disordered phase of perovskite film in a heating process. Fig. 14 (f) shows the deconvoluted PL spectra using the bi-Gaussian function with increasing temperature. Remarkably, the analysis of the evolution of PL

intensities of ordered and disordered perovskite phases revealed that the disordered phase began to dominate above 70 °C. This suggests that the structural degradation of perovskite film might occur at 70 °C, the temperature at which $V_{OC}$ began to decrease, as shown in Fig. 14 (f). [9]

## 4.4 Temperature dependent time-resolved PL

Since the structural degradation of perovskites will accompany the increased trapping rates of charge carriers, it is expected that charge trapping will accordingly vary during the heating and cooling processes. For this purpose, we measured temperature-dependent lifetime decays and calculated the trapping and detrapping rates of photogenerated charge carriers. The trapping rate is proportional to the photogenerated carrier density and the number of empty trap states while the detrapping rate is proportional to the number of occupied trap states and empty conduction band states as expressed by the following equations [9]:

$$\frac{dn(t)}{dt} = -k_{tr}n + k_{de}n_{tr} \qquad (11)$$

$$\frac{dn_{tr}(t)}{dt} = k_{tr}n - k_{de}n_{tr} \qquad (12)$$

where $n$ is the density of free electrons and $n_{tr}$ the density of electrons in the traps, $k_{tr}$ the trapping rate and $k_{de}$ the detrapping rate. Fig. 15 (a) shows best-fitting of lifetime decay using the trapping and detrapping models. Also, temperature-dependent lifetimes and calculated trapping and detrapping rates were shown in Fig. 15 (b) and (c). When the temperature rises from room temperature to 40 °C, the lifetime value increased while the charge trapping rate dropped sharply, but the detrapping rate increased. Again, reduced

charge trapping but increased detrapping rate confirm the defect passivation of perovskite film due to both light and heat exposure. As the temperature rises above 70 °C, lifetime values decreased gradually while a rapid decrease in lifetime values above 70 °C was observed. From temperature-dependent lifetime transitions, we quantitatively analysed the trap depth using an Arrhenius plot

$$\tau(t) = \frac{\tau_0}{1 + \tau_1 \exp(-E_a / kT)} \qquad (13)$$

that yielded a trap depth of 145 meV at a temperature of 40-70 °C, which is in good agreement with reported values. Above 70 °C, a deeper trap depth of 1.1 eV was observed, which might be related to thermal degradation of the perovskite. Therefore, it is reasonable to assume that a sharp increase in the trapping rate in Fig. 15 (c) could be related to the formation of deep trap states in the perovskite film. Indeed, thermal degradation of the perovskite film at higher temperatures produced deep defects in the perovskite film with a deep activation energy of ~1.5eV. In addition, we observed very interesting behaviour when the perovskite temperature decreased, i.e. the lifetime value and charge trapping continued to increase. This indicates that the degradation of the perovskite film triggered around 70~82 °C did not stop but continued even after lowering the temperature. [9]
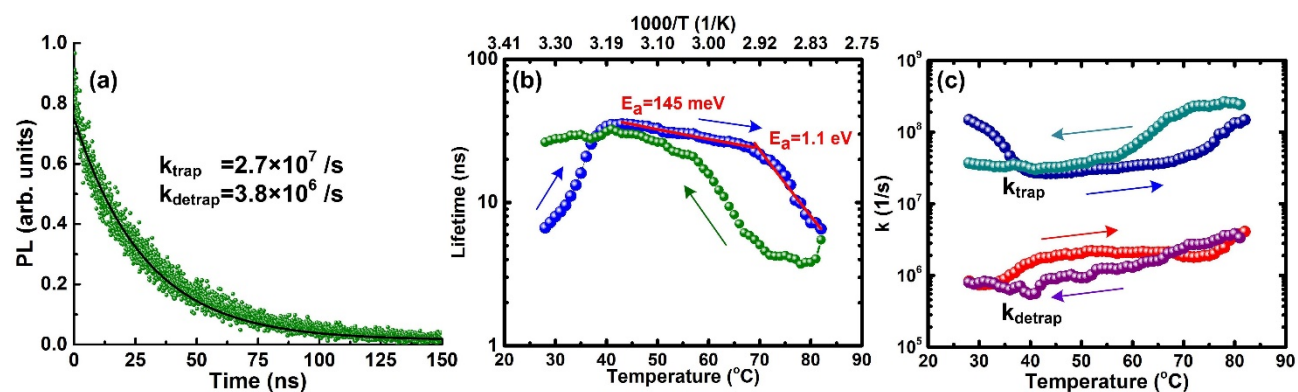
Fig. 15. (a) Best-fitting of lifetime decay using trapping and detrapping model and the evolution of (b) lifetime and (c) trapping and detrapping rates during temperature cycling. Quantitative analysis of Arrhenius plots resulted in the trap depth of 145 meV between 40 and 70 °C and 1.1eV above 70 °C, respectively. [9]

## 4.5 Temperature dependent UV-VIS measurement

Since light harvesting is closely related to the photocurrent of the perovskite solar cell, we conducted temperature-dependent UV-VIS measurement of the $MAPbI_{3-x}Cl_x$ perovskite film. Note that the $PbI_2$ is known to have a band edge absorption around 510 nm while the $MAPbI_{3-x}Cl_x$ exhibits a band edge absorption at much longer wavelengths of 700-800 nm. Fig. 16 shows UV-VIS measurement of perovskite film during the heating and cooling processes. At room temperature, $MAPbI_{3-x}Cl_x$ perovskite film exhibited band edge absorption in the range of 700 nm to 800 nm. Upon heating from 28°C to 82°C in Fig. 16 (a), we observe a gradual blue-shift of absorption band edge from 760 nm (or 1.63 eV) at room temperature to 736 nm (or 1.69 eV) at 82 °C, which is related to the downshift of the

valence band maximum and conduction band minimum. Interestingly, we did not observe a sharp change in the light absorption over the tetragonal–cubic phase transition around 54 °C, inferring the continuous tilting of the $PbI_6$ octahedra and the continuous change of Pb-I bond length with rising temperature. However, in the shorter wavelength range of less than 550 nm in Fig. 16 (a) we observed a gradual decrease in light absorption. We also observed that cooling down from 82 °C to 28 °C the absorption spectrum at shorter wavelengths of less than 550 nm continued to decrease, as shown in Fig. 16 (b) and (c). Remarkably, the absorption band edge of $PbI_2$ in Fig. 16 (c) became sharper during the cooling process. In addition, the comparison of UV-VIS absorption before and after the heating and cooling processes in Fig. 16 (d) shows the decreased light absorption. This suggests that light harvesting capability of $CH_3NH_3PbI_{3-x}Cl_x$ perovskite films deteriorated continuously during the cooling process.
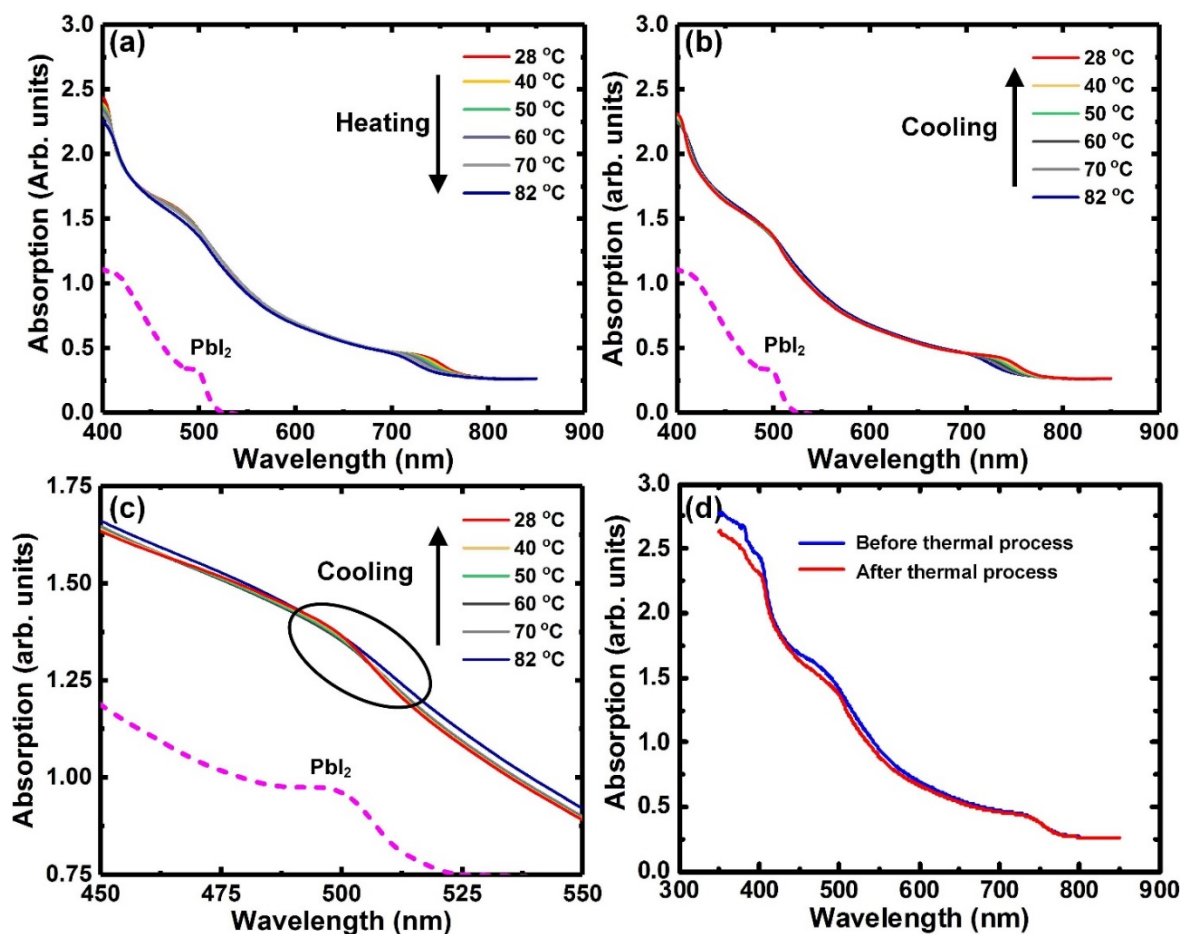
Fig. 16. Temperature dependent UV-VIS absorption of MAPbI$_{3-x}$Cl$_x$ during (a) heating and (b) cooling processes. (c) Absorption spectra from 450 nm to 550 nm was re-plotted to clearly show the development of the PbI$_2$ phase. (d) Comparison of UV-VIS before and after thermal process indicates the decreased light absorption after competing thermal process. [9]

**4.6 SEM and X-ray diffraction measurements**

Degradation in solar cells can primarily occur in three places: i) in the bulk of the active layer; ii) at the interface of the perovskite and the electrodes; and iii) at the electrode itself. To probe any degradation of the morphological degradation of perovskite films, perovskite/metal interfaces and the metal electrode of perovskite solar cells, scanning electron microscopy (SEM) measurement was conducted. In this case, two solar cells were fabricated under the same conditions and heat-treated for 0 and 3hrs. Fig. 17 (a) and (b) show cross-sectional SEM images for perovskite solar cells heated for 0 and 3 hrs at 82 °C. However, we have not found any noticeable degradation of the perovskite film, perovskite/metal interfaces, or Ag electrode from cross-section SEM images. However, we cannot rule out subtle degradation of perovskite film that SEM cannot detect but that leads to structural deformation. Therefore, we also performed X-ray diffraction measurements on perovskite solar cells at different annealing temperatures. Fig. 17 (c) shows the X-ray diffraction of perovskite solar cells heat-treated in the nitrogen filled Linkam sample stage. Before heating perovskite solar cells, we observed the presence of Ag from a metal electrode, $PbI_2$, $CH_3NH_3PbI_3$, and $CH_3NH_3PbCl_3$ phases, which is typical for the hot-casting technique of perovskite thin film. When the perovskite solar cell was heated at 55 °C, the X-ray peak of $PbI_2$ did not show a noticeable change. In contrast, we found that the X-ray peak intensity of $PbI_2$ slightly increased when the perovskite solar cell was heated at 70 ° C. This confirms that the thermal degradation of the perovskite layer indeed occurred at above 70 °C. In addition, a sharp increase in $PbI_2$ phase was observed at 82°C, inferring further degradation of the perovskite layer. Such structural degradation of $MAPbI_{3-x}Cl_x$ film might explain the observed optical degradations - a rapid increase in the disordered phase, charge trapping rate and trap depth of the $MAPbI_{3-x}Cl_x$ film and degraded perovskite solar cell performance above 70 °C. In addition, when the film

temperature cooled down from 82 °C to room temperature, we observed on-going thermal degradation of MAPbI$_{3-x}$Cl$_x$ thin film as demonstrated from PL and UV-VIS measurements. Remarkably, we also observed a similar degradation of the photovoltaic performance of the perovskite solar cell when the device temperature cooled down from 82°C to room temperature. Therefore, we can conclude that the irreversible device performance could originate from the intrinsic thermal degradation of MAPbI$_{3-x}$Cl$_x$ thin film. We noticed that there was a slightly different irreversible behaviour between V$_{OC}$ and J$_{SC}$ during the cooling process. It is found that the V$_{OC}$ gradually recovered whereas the photocurrent decreased continuously during the cooling process. Such difference might point to the fact that the V$_{OC}$ is very sensitive to surface and interfacial defects and is determined by the difference in quasi-fermi levels (or chemical potentials) of electrons and holes. In contrast, the photocurrent is more related to the surface defects, bulk defects, charge carrier mobility, and diffusion processes. We think that structural deformation occurred above 70 °C was not completely restored to the original perovskite structures and creates considerable defects in the bulk during the cooling process. As a consequence, there are a number of defects in the bulk facilitate non-radiative recombination of photo-generated charge carriers while diffusing towards respective electrodes, resulting in continued degradation of the photocurrent. [9]
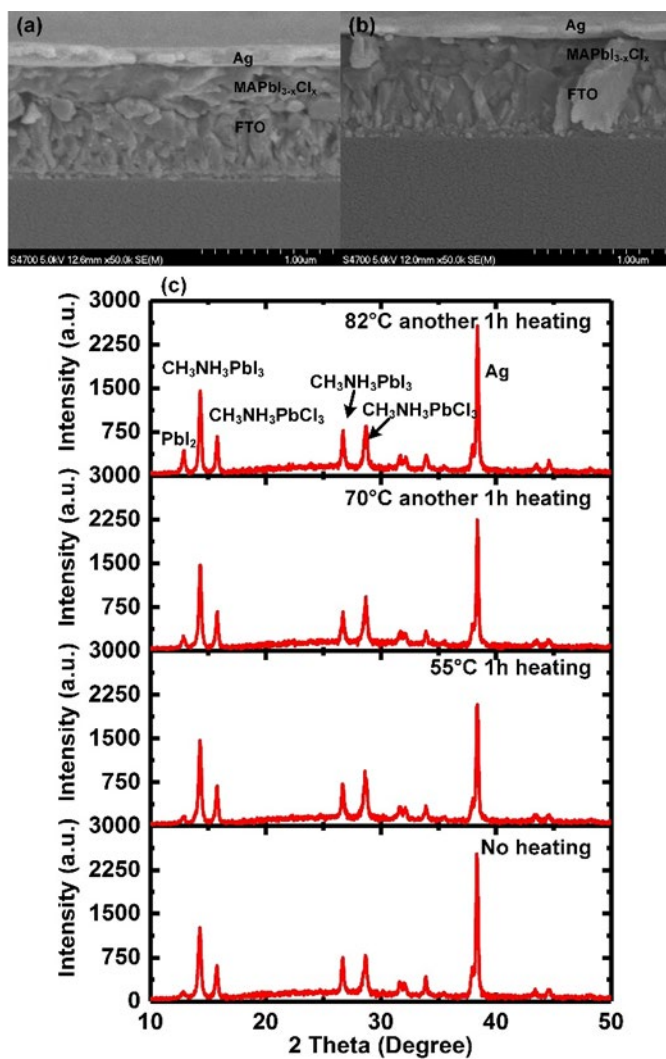
Fig. 17. SEM images of (a) 0 hr and (b) 3 hrs heating at 82 °C and (c) X-ray diffraction measurement at different temperatures, particularly showing the development of $PbI_2$ above 70 °C. [9]

## 4.7 Summary

In summary, we have demonstrated the irreversible degradation of perovskite solar cells during heating and cooling processes. In particular, perovskite film showed irreversible degradation at 70°C or higher which can be explained by dynamic evolution of degraded crystallinity, increased charge trapping, deep trap depth and formation of $PbI_2$. One interesting aspect is that the degradation did not stop when the temperature was below 70°C. This irreversible degradation study will help to commercialize perovskite solar cells and increase thermal stability. In the following chapter, we will focus on investigating the stability of perovskite film at a higher temperature.

**CHAPTER 5**

**ROLE OF PMMA TO MAKE MAPBI$_3$ GRAIN BOUNDARY HEAT RESISTANCE**

**5.1 Introduction**

Hybrid organic-inorganic perovskites have attracted much attention in recent years due to their outstanding optoelectronic properties [16,42] and opened new ways for optoelectronic applications such as photovoltaics [20,134] photodetectors [135], light emitting diodes (LEDs) [136], and lasers [137,138]. In the photovoltaic research, perovskite materials have achieved photo conversion efficiencies exceeding 25% [8]. Despite recent progress, designing long-lasting materials and device structures is still challenging. In general, the degradation of perovskite films undergoes a series of chemical reaction paths when exposed to moisture, oxygen, light, and heat [59,66,139,140,141,142]. So far, the light, oxygen and moisture-induced degradation can be slowed by integrating the barrier or interface layer or using advanced encapsulation [60,143], compositional engineering [26,69,144], and UV-filter techniques [145] within the device architecture [146]. However, the *most* representative perovskite material of CH$_3$NH$_3$PbI$_3$ (MAPbI$_3$) absorber appears to be thermally unstable even in an inert environment [59,131,130]. This poses a great challenge for solar cell applications because device temperatures can increase up to 45 °C higher than ambient temperatures when operating under direct sunlight [59]. To achieve better stability, all inorganics, triple or quadruple cations coupled with mixed halide anions, polymer composites, and others have been attempted [59,73]. Among them, the use of triple or quadruple cations looks like the rational approach to enhance the stability of perovskites due to thermally stable cations, a stable Goldschmidt tolerance factor (t) approaching to unity and

stronger bond strengths [147]. Recently, new insights into perovskite stability have been revealed by advances in MAPbI₃ solar cells [148]. The high stability of MAPbI₃ solar cells has been achieved by using additives (80 % of initial PCE after 500 hrs of thermal aging at 85 °C and 20 % relative humidity) [148]. Note that this stability is comparable to the one achieved by quadruple cations (CH₃NH₃ (or MA), HC(NH₂)₂ (or FA), Cs, Rb) based solar cells (95 % of initial PCE after 500 hrs of thermal aging at 85 °C in a nitrogen environment) [75]. This result is somewhat surprising because MAPbI₃ perovskites were often considered to be thermodynamically unstable compared to triple or quadruple cation based perovskites [59,75]. Presently, it was speculated that the high crystallinity of MAPbI₃ with larger grains was responsible for enhanced thermal stability [148]. Also, Wang, et al. demonstrated enhanced thermal stability of MAPbI₃ perovskite films by altering nanoscale defect states and disordered chemistries of grain boundaries (GBs) [149]. His experiments in part confirm that moisture-induced degradation initiated at the GBs and propagated along the in-plane direction when exposed to external forces. Recently, Park, et al. observed the enhanced thermal stability of perovskite via GB passivation [150]. These findings highlight the importance of stabilizing the GBs to improve the stability of perovskite solar cells. [10]

Recently, polymers such as poly (methyl methacrylate) (PMMA), polystyrene, polyethylene terephthalate (PET), polytetrafluoroethylene (PTFE) or Teflon, polydimethylsiloxane (PDMS), and polycarbonate (PC) have been used as barriers to protect perovskite films from oxygen and moisture ingression [151,152]. Among them, PMMA showed excellent physical properties such as high transparency, hardness, chemical resistance, and glass transition temperature [153]. Despite all these excellent physical properties, the poor conductivity of PMMA polymer could be an issue when applied in a perovskite solar cell. However, many studies have shown that the conductivity of PMMA can be improved by incorporating graphene

in the polymer [154]. So far, PMMA has been primarily used in perovskite devices to protect against moisture, facilitate charge transport, reduce trap sites and charge recombination losses, and improve efficiency [152,61]. Several studies proved that PMMA encapsulated perovskite solar cells can retain 95% of initial PCE after exposure to air (25°C, 35% RH) for 1000 hrs [152]. Recently, Mckenna, et al. reported thermal degradation of PMMA treated perovskite films with a heating time of 29 hrs [155]. They observed the progressive evolution of PL quenching regions with prolonged thermal aging. In contrast, Habisreutinger, et al. reported further improved thermal stability of MAPbI$_3$ film using carbon nanotube/PMMA composites up to 96 hrs at 80 °C in air [62]. In addition, Han et al., explored combined poly(methyl methacrylate) (PMMA)/reduced graphene oxide (rGO) composite (PRC) passivation layer for the enhanced chemical and thermal stability of PSCs [156]. However, at this stage, it is not clearly known what caused thermal stability of MAPbI$_3$/PMMA films. Currently, it is well known that organic MA cations of MAPbI$_3$ are weakly bound via hydrogen bonds to the ionic cages of Pb and I [157]. Therefore, unbound or loosely bound organic MA cations at the GBs or defective domains are likely to escape from the crystal lattice and ultimately lead to the thermal decomposition to PbI$_2$. For this reason, it is hypothesized that improved thermal stability might be associated with an introduction of scaffolding material such as PMMA polymer to render GBs less defective and tightly scaffold perovskite components. [10]

To further understand the critical role of PMMA in MAPbI$_3$, MAPbI$_3$/PMMA films were fabricated and structural and chemical degradations were characterized during the thermal aging test. In this work, we performed the thermal stability study at 85 °C for up to 1000 hours of perovskite layers with a thin PMMA layer. To perform this investigation, we used an energy dispersive X-ray spectroscope (EDS), X-ray diffraction measurement, infrared nanoscopy, and

proton nuclear magnetic resonance (NMR) measurements to probe the chemical and structural degradation across the GBs at the nanoscale. [10]

## 5.2 Perovskite film with PMMA

The hot-casting technique [17] was used to produce MAPbI$_3$ films in an air environment by facilitating thermal energy to form large grain perovskites during the spin-casting process. Specifically, the FTO/glass substrate was pre-heated at a temperature (180°C) higher than the boiling temperature (153°C) of the DMF solvent while the perovskite precursor solution was kept at 70 °C, as shown in Fig. 18 (a). After the FTO/glass substrate was transferred to the spin-coater, the perovskite precursor solution was then immediately spin-coated on the hot FTO/glass substrate for 10 seconds at 4000 rpm. Also, poly(methyl methacrylate) (PMMA) dissolved in chlorobenzene (Sigma-Aldrich, 99.5%) (10mg/ml) was spin-coated onto the MAPbI$_3$ film with a spin speed of 4000 rpm for 10 s in a glove box. Surface morphology of hot-casted MAPbI$_3$ film is shown in Fig. 18 (b). Perovskite films exhibited leaf-like morphologies that are a typical feature of a hot-casting technique. Since it is critical to ensure that the PMMA was evenly distributed over the MAPbI$_3$ film, the nanoscale morphology of perovskite and chemical vibration modes of PMMA were probed using IR nanoscopy measurement, as shown in Fig. 18 (c)-(f). The schematic of an IR nanoscopy system is illustrated in Fig. 18 (c). As shown, the IR nanoscopy combines atomic force microscope (AFM) and photo thermal induced resonance spectroscopy (PTIR) to probe and correlate aspects of film morphology and IR absorption mapping image of the local region at a specific frequency [158,159,160,161]. A tuneable IR laser is illuminated onto the ZnSe prism with total internal reflection, then

the sample absorbs light at a specific frequency and volume expansion occurs sequentially in the nanoscopic area of the sample. After that, the AFM cantilever in contact with the sample surface begins to vibrate. These vibrations of the cantilever are detected by a four-quadrant AFM detector and transformed into an absorption spectrum using a Fourier transform. As IR nanoscopy uses AFM mode, a high spatial resolution of ~20 nm can be achieved, which makes it possible to probe the uniform coating of PMMA within $MAPbI_3$ perovskite film at the nanoscale level. In order to investigate the PMMA distribution at the nanoscale levels, particularly at perovskite grain boundaries (GBs), we performed the IR absorption mapping of stretching vibrational mode of PMMA across perovskite grains. Fig. 18 (d) indicates the AFM morphology of perovskite films containing grain boundary (GB) and grain interior (GI). Two representative points at GI (P1) and GB (P2) were probed and analyzed with IR absorption spectra of the C=O stretching vibrational mode ($1736 \text{ cm}^{-1}$) of PMMA and C-H bending mode ($1472 \text{ cm}^{-1}$) of $MAPbI_3$ [162,163]. As shown in Fig. 18 (e), both the C=O stretching vibrational mode of representative peak of PMMA and C-H bending vibrational mode of representative peak of $MAPbI_3$ were observed at both GBs and GIs. In addition, from the absorption mapping image of C=O vibrational mode, we can clearly see that PMMA was well distributed over the entire grain area of the $MAPbI_3$ film, as shown in Fig. 18 (f). [10]
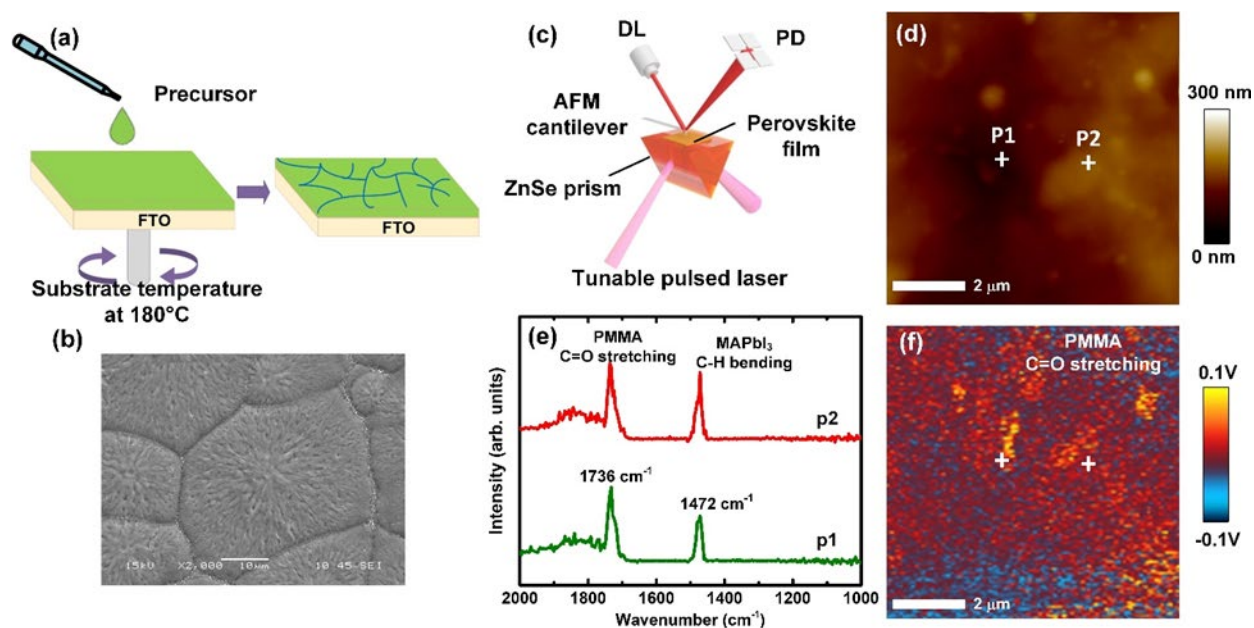
Fig. 18. (a) Hot-casting technique of perovskite and (b) SEM image of hot-casted MAPbI₃ film. (c) Schematic of IR nanoscopy system is shown with (d) AFM morphology of MAPbI₃ film, (e) IR spectra and (f) IR absorption mapping. Two specific locations of P1 and P2 were chosen for C=O stretching (1736 cm⁻¹) of PMMA and C-H bending (1472 cm⁻¹) of MAPbI₃. [10]

## 5.3 Morphological stability of perovskite thin film with PMMA at 85 °C

To understand the thermal stability of MAPbI₃, the MAPbI₃ films were placed on a hotplate in a nitrogen-filled glove box in which the hotplate temperature was kept at 85 °C for up to 1000 hrs. Surface morphologies of perovskite films with and without PMMA were examined over heating time, as shown in Fig. 19. Fig. 19 (a)-(c) show the surface morphology and cross-sectional images of fresh MAPbI₃ films without PMMA before the thermal treatment. When perovskite

films were thermally treated in a nitrogen-filled glove box, we observed thermal degradation of MAPbI$_3$ without PMMA. Fig. A1. (a)-(e) show planar SEM images exhibiting the degradation of MAPbI$_3$ without PMMA in the form of pinholes with increased thermal treatment time. Notably, thermal degradation of MAPbI$_3$ without PMMA initiated at the GBs. After 72 hrs of heating, a number of pinholes formed around GBs while GIs exhibited far stronger stability. As the heating time further increased, the pinholes formed at GBs extended toward the GIs. The entire surface of MAPbI$_3$ extensively degraded with many pinholes after 528 hrs of heating, as shown in Fig. 19 (d). Cross-sectional SEM image of MAPbI$_3$ in Fig. 19 (e) and (f) clearly show the decomposition of perovskite films after 528 hrs of heating, showing many hilly shapes of perovskite films. Some areas revealed the FTO substrates due to near-complete decomposition of ~450 nm thick MAPbI$_3$ films. Conversely, MAPbI$_3$/PMMA films showed negligible morphological change even after 1000 hrs of heating at 85 °C, as shown in Fig. 19 (g). The cross-sectional SEM image in Fig. 19 (h) and (i) show the robust characteristic of MAPbI$_3$/PMMA, showing a uniform perovskite film and a sharp interface with FTO substrate even after 1000 hrs of heating. This is in a stark contrast with MAPbI$_3$ without PMMA in which pinholes were predominantly formed at GBs and propagated towards the GIs. [10]
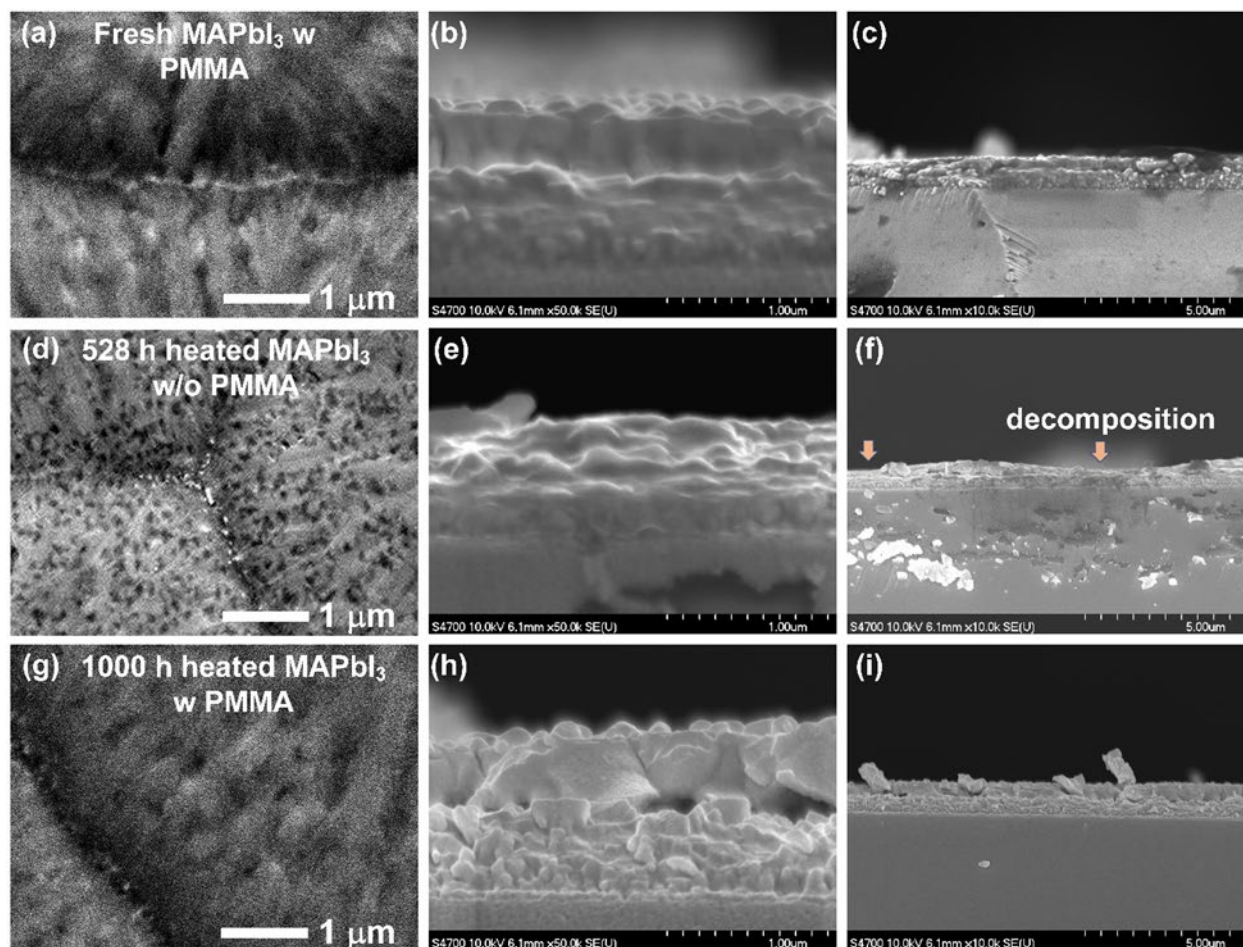
Fig. 19.  SEM images of (a-c) fresh MAPbI$_3$ without PMMA before heat treatment, (d-f) MAPbI$_3$ without PMMA after 528 hrs of heating at 85 °C and (g-i) MAPbI$_3$/PMMA after 1000 hours of heating at 85 °C. [10]

## 5.4 Structural stability of perovskite thin film with PMMA at 85 °C

Our XRD measurement also confirmed the degradation of MAPbI$_3$ without PMMA as thermal treatment time increased, as shown in Figure 3. The fresh perovskite film contains two

prime perovskite peaks located at 14.3° and 28.4° that are indexed to the (110) and (220) planes. In addition, the presence of the (211) plane at a scattering angle of 23.5° demonstrates the tetragonal phase of perovskite. The presence of FTO can be seen at 26.8°, 33°, and 37°. Initially, there is no presence of $PbI_2$ in the diffraction pattern of fresh perovskite film. However, after 72 hours of heating at 85 °C, an additional new peak at 12.9°, which is attributed to $PbI_2$, is clearly observed, as shown in Fig. 20 (a). The perovskite peaks at scattering angles of 14.3° and 28.4° have lessened with increased heating time, as shown in Fig. 20 (a) and (c). Conversely, the peak intensity for $PbI_2$ gradually increased with increased heating time (see Fig. 20 (a) and (d)), demonstrating that $MAPbI_3$ mostly degraded to $PbI_2$. Moreover, a peak of $I_2$ at 38.7° after 72 hours of heating was observed and became more prominent with increased heating time. This confirms that $MAPbI_3$ film without PMMA degraded into $PbI_2$ and $I_2$. On the contrary, no significant difference was found in the diffraction pattern of $MAPbI_3$/PMMA film upon heating for 1000 hours at 85 °C, as shown in Fig. 20 (b). Fig. 20 (c) and (d) show the variation of XRD intensity of $MAPbI_3$, $PbI_2$, and $I_2$ with and without PMMA, clearly demonstrating the excellent thermal stability of $MAPbI_3$/PMMA. A similar trend was observed for $MAPbI_3$ diffraction peak intensity along the (110) direction, as shown in Fig. 20 (c). Remarkably, the crystal size remained almost constant after 144 hrs. However, the crystallite size for the $MAPbI_3$ sample without PMMA gradually decreased with the heating time, which is due to the thermal degradation. [10]
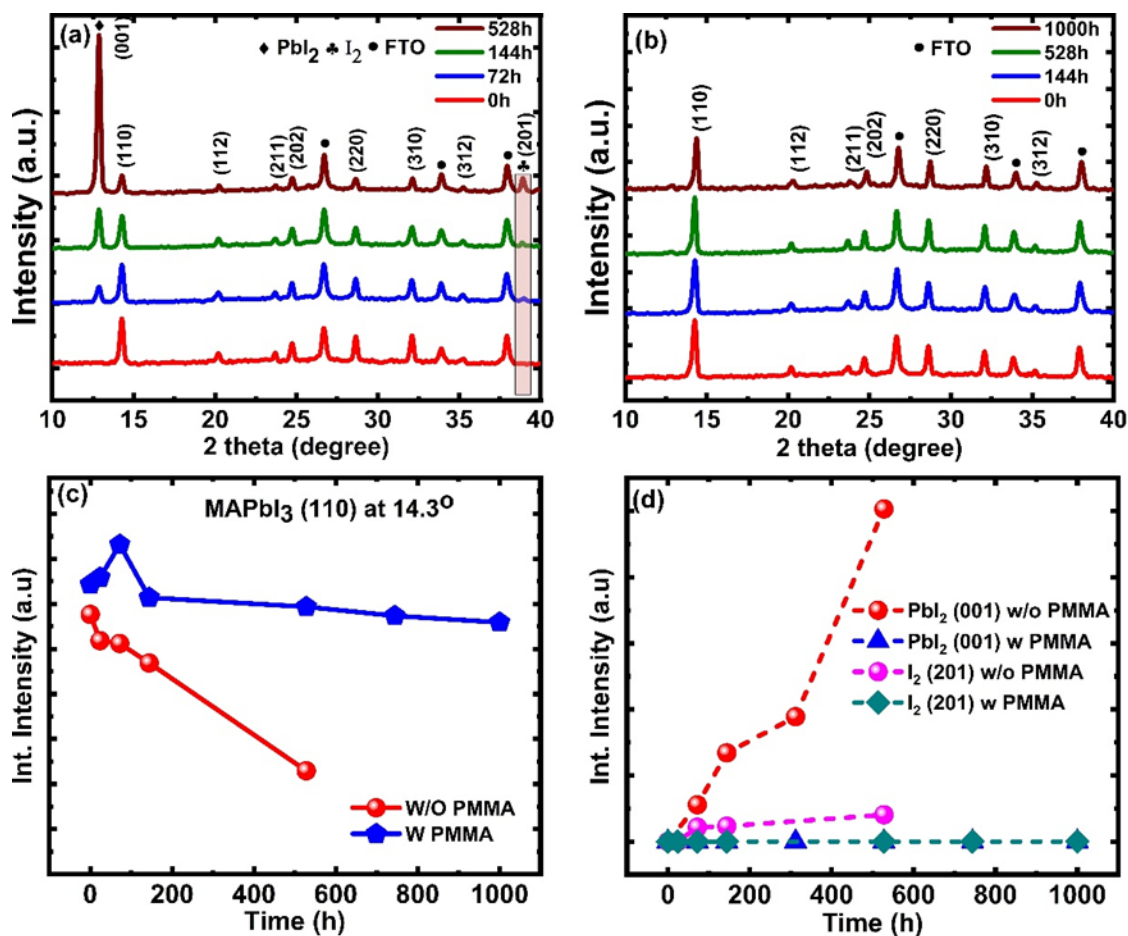
Fig. 20. Time evolution of XRD spectra of (a) MAPbI₃ without PMMA and (b) MAPbI₃ with PMMA at 85 °C. The integrated peak intensity of (c) MAPbI₃ along (110), (d) PbI₂ along (001), and I₂ along (201) direction for MAPbI₃ sample with and without PMMA was shown. [10]

## 5.5 Absorption study of perovskite thin film with PMMA at 85 °C

The UV-vis absorption spectrum also supports the heat resistant behavior of MAPbI₃ when PMMA was applied (Fig. 21). The absorbance spectra clearly revealed the degradation of MAPbI₃ without PMMA over time. However, the absorption spectra of MAPbI₃/PMMA film displayed

nearly identical pattern before and after heating at 85 °C. Moreover, the absorption band edge shifted dramatically for MAPbI₃ without PMMA, which can be observed from the optical bandgap $E_g$. Davis and Mott's work [164] showed that the optical absorption strength depended on the difference between photon energy and the bandgap as, $(\alpha h\nu)^{1/n} = A(h\nu - E_g)$, where $h$ is Planck's constant, $\nu$ is the photon's energy, $\alpha$ is the absorption coefficient, $E_g$ is the bandgap, and A is a proportionality constant. The value of the exponent denotes the nature of the electronic transition, considered as n=1/2 for direct allowed transition of the perovskite film. The optical bandgap determined from the extrapolation of the linear part of a Tauc plot [165] is shown in Fig. 21 (c) and (d). The value of the optical bandgap for the MAPbI₃ sample was 1.56eV, which is consistent with the previous reports [166,167]. Interestingly, the bandgap shifted from 1.56eV to 1.52eV after heating for 528 hours in the case of the MAPbI₃ sample without PMMA, while a nominal change of optical bandgap (~1meV) was observed for MAPbI₃ with PMMA. The nominal change in optical bandgap of MAPbI₃/PMMA film indicates high thermal stability was achieved by applying PMMA layer. [10]
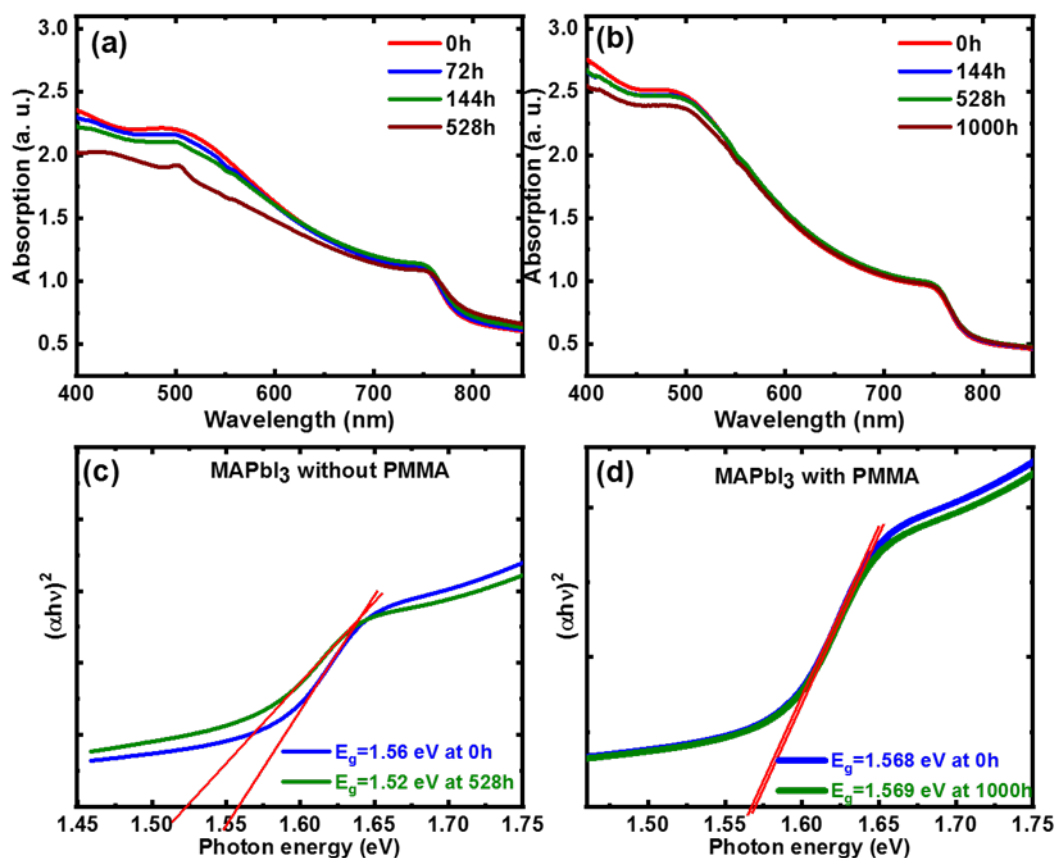
Fig. 21. Absorption spectra as a function of wavelength for MAPbI3 sample (a) without PMMA and (b) with PMMA. Tauc plots of optical coefficient $(\alpha h\nu)^2$ *vs.* photon energy (hν) for (c) MAPbI3 without PMMA and (d) MAPbI3 with PMMA are displayed. [10]

## 5.6 Elemental analysis of perovskite thin film with PMMA at 85 °C

To further investigate heat-induced chemical decomposition behavior of perovskite films, energy dispersive spectroscopy (EDS) mapping was investigated. In this study, three different MAPbI3 films including the bare MAPbI3, MAPbI3 heat-treated for 528 hrs and MAPbI3/PMMA heat-treated for 1000 hrs were analyzed. Fig. 22 (a)-(i) show 2D EDS mapping of MAPbI3 films

highlighting local chemical distributions of oxygen (O) and lead (Pb) across the perovskite grain. Overall, a deficiency of perovskite elements was observed at GBs for all three samples. However, high oxygen concentrations of bare MAPbI$_3$ and heated MAPbI$_3$ without PMMA were observed, as shown in Fig. 22 (d)-(e). Remarkably, the uniform oxygen distribution of MAPbI$_3$/PMMA in Figure 4(f) was observed after heating for 1000 hrs at 85°C. To quantitatively examine chemical distributions of perovskite elements across the films, several locations at GBs and GIs were pinpointed and analyzed. Fig. 22 (j) shows the average atomic percent of oxygen at GBs and GIs. For bare MAPbI$_3$ film, the oxygen atomic percent was 17.7±2% and 57.1±7% at GIs and GBs where oxygen content at GBs was about more than three times higher than at GIs. This indicates that moisture was heavily incorporated into GBs during the film process. Even after heating of bare MAPbI$_3$ for 528 hrs in a nitrogen-filled glove box, no change in the oxygen atomic percent at GIs and GBs was observed. This indicates that heating MAPbI$_3$ samples in a nitrogen environment did not reduce oxygen of perovskite films. Instead, we observed a significant reduction of oxygen content in MAPbI$_3$/PMMA in which the oxygen atomic percent remarkably decreased to 10.4 ± 1.1 % at GIs and 22.5±6.5 % at GBs, respectively. Such reduction of oxygen contents of MAPbI$_3$/PMMA film might explain the uniform distribution of oxygen in 2D EDS mapping in Fig. 22 (f). We also investigated the I/Pb elemental ratio of MAPbI$_3$ at GIs and GBs, as shown in Fig. 22 (k). For bare MAPbI$_3$, it is found that GBs were found to be defective and composed of non-stoichiometric perovskite chemistry. Specifically, the large I/Pb ratio of 6.0 ±0.9 was found at GBs for bare MAPbI$_3$ films without PMMA. After 528 hrs without PMMA, the I/Pb ratio decreased to 4.7±0.9. A further decrease in the I/Pb ratio to 4.4 ±0.6 was observed at GBs for MAPbI$_3$/PMMA after 1000 hrs of heating. Conversely, GIs of MAPbI$_3$/PMMA yielded a ratio of I/Pb close to ~3.3±0.2, which is close to a stoichiometric value of I/Pb=3. After 528 hours of
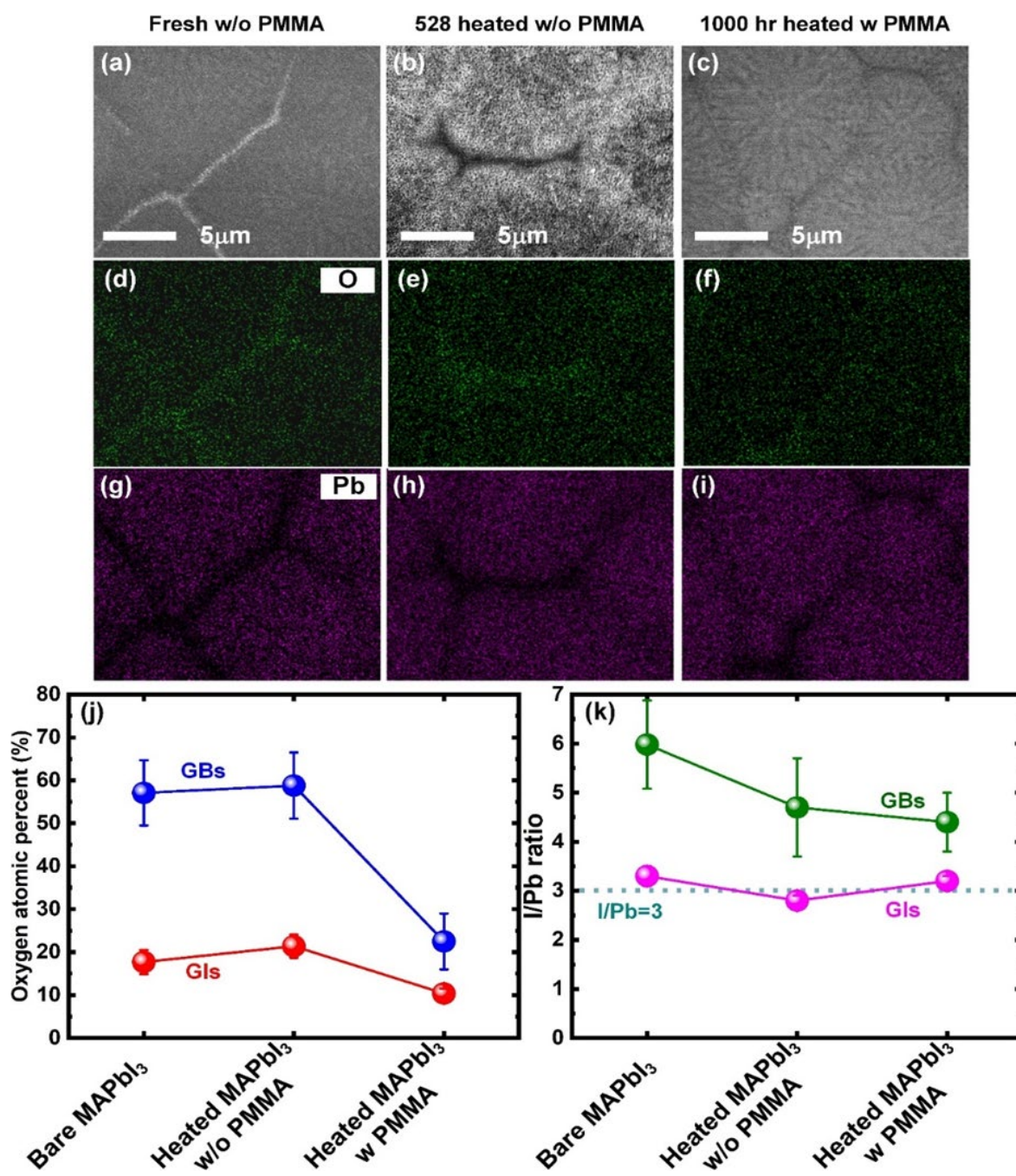
Fig. 22.  SEM images of (a) fresh perovskite, (b) heated perovskite film without PMMA at 85 °C for 528 hours, and (c) heated perovskite film with PMMA at 85 °C for 1000 hours and

corresponding chemical distributions of (d-f) oxygen and (g-i) lead (Pb) that were measured by EDS mapping. (Scale bar: 5 μm). (j) Average oxygen atomic percent and (k) I/Pb ratios at the GBs and GIs across the films by pinpointing several locations at GBs and GIs were also shown. [10]

heating of MAPbI$_3$ without PMMA, a slight modification of chemical distribution was observed at GIs where the I/Pb ratio of MAPbI$_3$ without PMMA decreased to 2.8±0.1. This indicates that GIs of MAPbI$_3$ without PMMA underwent thermal decomposition towards PbI$_2$ while MAPbI$_3$/PMMA film after 1000 hrs of heating maintained the I/Pb ratio of 3.2±0.1 at GIs, indicating no chemical degradation. [10]

**5.7 IR nanoscopic study of perovskite thin film with PMMA at 85 °C**

To further investigate heat-induced chemical decomposition properties of perovskite films, an IR nanoscopy measurement was performed, as shown in Fig. 23. Note that for the IR mapping study, a relatively short heating time of 2 hrs for MAPbI$_3$ films was used to rapidly probe the evolution of GIs and GBs with and without PMMA. Here, a conventional oven was used for heat treatment of the MAPbI$_3$ film formed on the ZnSe prism. By using a conventional oven, it was possible to apply heat from below, above and both sides. Thus, we were able to obtain the chemical property of MAPbI$_3$ film in a faster time. Fig. 23 (a) and (c) show typical topography images of hot-casted MAPbI$_3$ film with and without PMMA, respectively. Fig. 23 (b) shows the IR mapping image of C-H bending vibrational mode of MAPbI$_3$ film without PMMA after heating at 85 °C for 2 hrs. It clearly shows the distinct intensity of C-H vibrational mode between GIs and GBs where GBs (blue color) exhibited significantly lower IR intensity than at GI (red color) that indicates thermal degradation. Unlike MAPbI$_3$ film without PMMA, MAPbI$_3$/PMMA film showed the

uniform intensity of the C-H bending mode in GB (red color) across the perovskite grains, as shown in Fig. 23 (d). These results are consistent with spatially resolved EDS measurements, showing high chemical stability of MAPbI$_3$/PMMA film. [10]
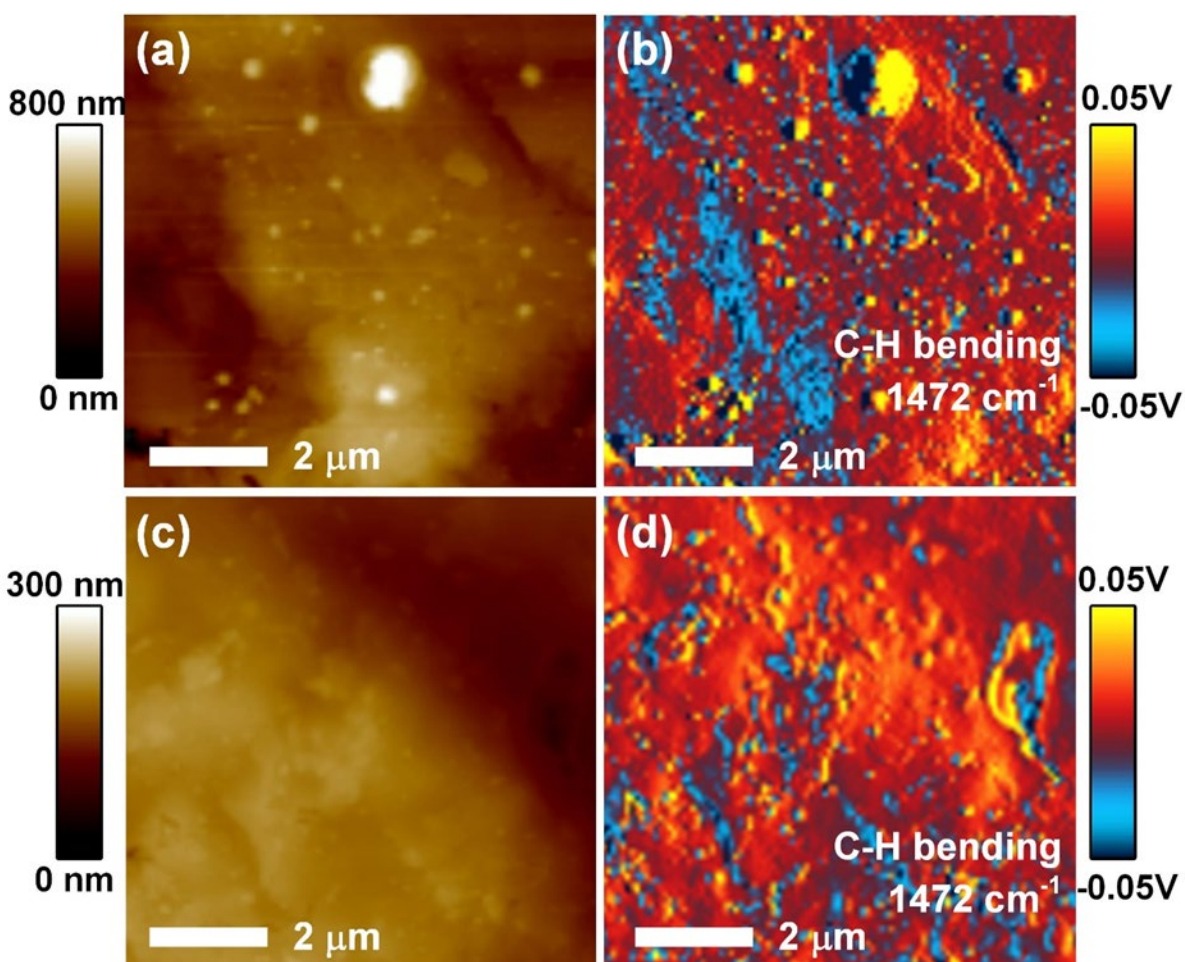


Fig. 23.  AFM image of MAPbI$_3$ film without (a), with (c) PMMA after heating at 85 °C for 2 hrs in conventional oven, IR absorption image of MAPbI$_3$ film without (b), with (d) PMMA after heating at 85 °C for 2 hrs in conventional oven. [10]

**5.8 NMR study of perovskite thin film with PMMA at 85 °C**

The proton nuclear magnetic resonance (NMR) experiment was carried out to probe an interaction between perovskite and PMMA by comparing the three NMR spectra of deuterated DMSO solutions of MAPbI$_3$, PMMA and MAPbI$_3$/PMMA. As shown in Fig. 24 (a), we observed the PMMA peak at 3.53 p.p.m that corresponds to the methoxy protons (−OCH$_3$) of PMMA [168] while the peak at 3.30 p.p.m is of residual solvent. For MAPbI$_3$, a sharp singlet occurring at 7.46 p.p.m for the proton resonance signals of the −NH$^{3+}$ group in the MAPbI$_3$ was observed. When the PMMA was added to MAPbI$_3$, the proton resonance signals of the −NH$^{3+}$ group slightly shifted downfield from 7.46 p.p.m to a 7.48 p.p.m with line broadening. Conversely, the chemical upfield shift of the methoxy proton peak of PMMA at 3.53 p.p.m to 3.47 p.p.m with slight line broadening was observed. This trend points to the interaction of PMMA and MAPbI$_3$ [156], which can be interpreted as the hydrogen bonds [169] between the methoxy protons (−OCH$_3$) of PMMA and −NH$^{3+}$ of MAPbI$_3$, as shown in Fig. 24 (b). Such bonding configuration between MAPbI$_3$ and PMMA will lead to the hydrophilic functional group (−OCH$_3$) closely bonding with MAPbI$_3$, which will turn hydrophobic functional group (−CH$_3$ methyl group) of PMMA outward, as shown in Fig. 24 (b). [10]
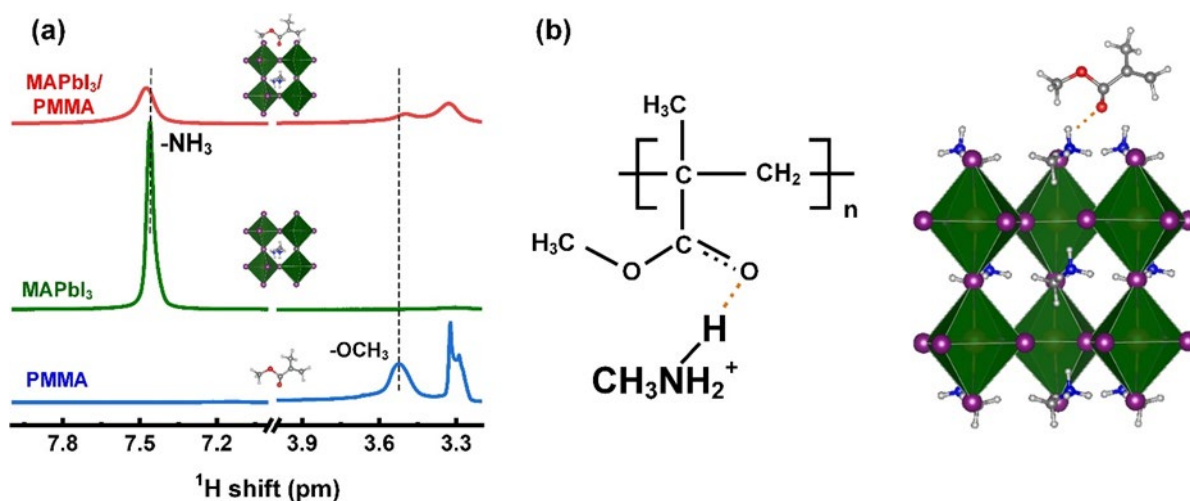
Fig. 24. (a) NMR spectra of MAPbI₃, PMMA and mixture of MAPbI₃+PMMA respectively and (b) plausible bonding configuration between MAPbI₃ and PMMA. [10]

## 5.9 Plausible mechanism of stability of perovskite thin film with PMMA at 85 °C

According to SEM, EDS, and IR nanoscopy measurements, it is believed that GBs and GIs of MAPbI₃ with and without PMMA go through different thermal degradation processes. According to EDS analysis, hot-casted MAPbI₃ film without PMMA mainly contains GBs composed of $(CH_3NH_3)_4PbI_6 \bullet H_2O$ while GIs are primarily composed of $CH_3NH_3PbI_3$. This conjecture is based on the I/Pb ratio in which GBs exhibited the I/Pb ratio=6 with the high oxygen atomic percent of 57% while GIs showed the I/Pb ratio=3.3 with the low oxygen atomic percent of 17.7%. Recently, Yang et al., identified a hydrated intermediate phase of $(CH_3NH_3)_4PbI_6 \bullet H_2O$ [116] during the air degradation process of perovskites using in-situ XRD technique. Since a hot-casting technique for MAPbI₃ films was fabricated in an air environment while maintaining a high temperature of FTO/glass around 180°C, there is a high chance for moisture to rapidly diffuse into

the GBs and form a hydrated intermediate phase of $(CH_3NH_3)_4PbI_6 \bullet H_2O$ at the GBs. Fig. 25 (a) shows our degradation model of MAPbI$_3$ without PMMA highlighting hydrated $(CH_3NH_3)_4PbI_6 \bullet H_2O$ at GBs and MAPbI$_3$ at GIs. Note that hydrated $(CH_3NH_3)_4PbI_6 \bullet H_2O$ has the 0D structure composed of isolated $PbI_6^{4-}$ octahedra, $CH_3NH_3^+$ cations and $H_2O$ molecules. Upon heating, bare MAPbI$_3$ films without PMMA will undergo different thermal degradation at GBs and GIs. This is due to the different amount of oxygen content (originated from absorption of moisture) at GBs and GIs where oxygen atomic percent at GBs was three times higher than that at GIs. Thus, it is expected that the high concentration of $H_2O$ will facilitate the decomposition process of perovskite at GBs to PbI$_2$ and I$_2$. Critically, $(CH_3NH_3)_4PbI_6 \bullet H_2O$ at GBs will eventually decompose into CH$_3$NH$_3$I, PbI$_2$ and I$_2$ in the presence of $H_2O$ at the GBs. Indeed, our XRD measurements showed the gradual increase in XRD intensities of PbI$_2$ and I$_2$ peaks with increased heating time. Conversely, it is believed that the thermal degradation at GIs from CH$_3$NH$_3$PbI$_3$ to PbI$_2$ might occur through a surface-initiated layer-by-layer degradation path by breaking the weak Pb-I-Pb bond along the (001) direction, as Fan, et al. revealed thermal degradation process [170]. Thereby, we believe that GIs undergo layer-by-layer thermal degradation converting from MAPbI$_3$ to PbI$_2$, which is a slower thermal degradation process than at GBs. Conversely, when PMMA is applied to perovskite, we observed the significant reduction of oxygen content of MAPbI$_3$/PMMA at both GBs and GIs after heating. Oxygen contents at GBs and GIs were 21% and 10%, which are three and two times lower than that of fresh and 528 hr heated MAPbI$_3$ without PMMA. Such reduction of oxygen can be ascribed to the excellent hygroscopicity of the PMMA molecules that surrounded perovskites. Note that the hygroscopic PEG polymer scaffold architecture was effectively used in MAPbI$_3$ perovskite films to absorb and drain water efficiently [171]. In this case, the omnipresent PEG molecules within MAPbI$_3$ films were anchored on the surface of
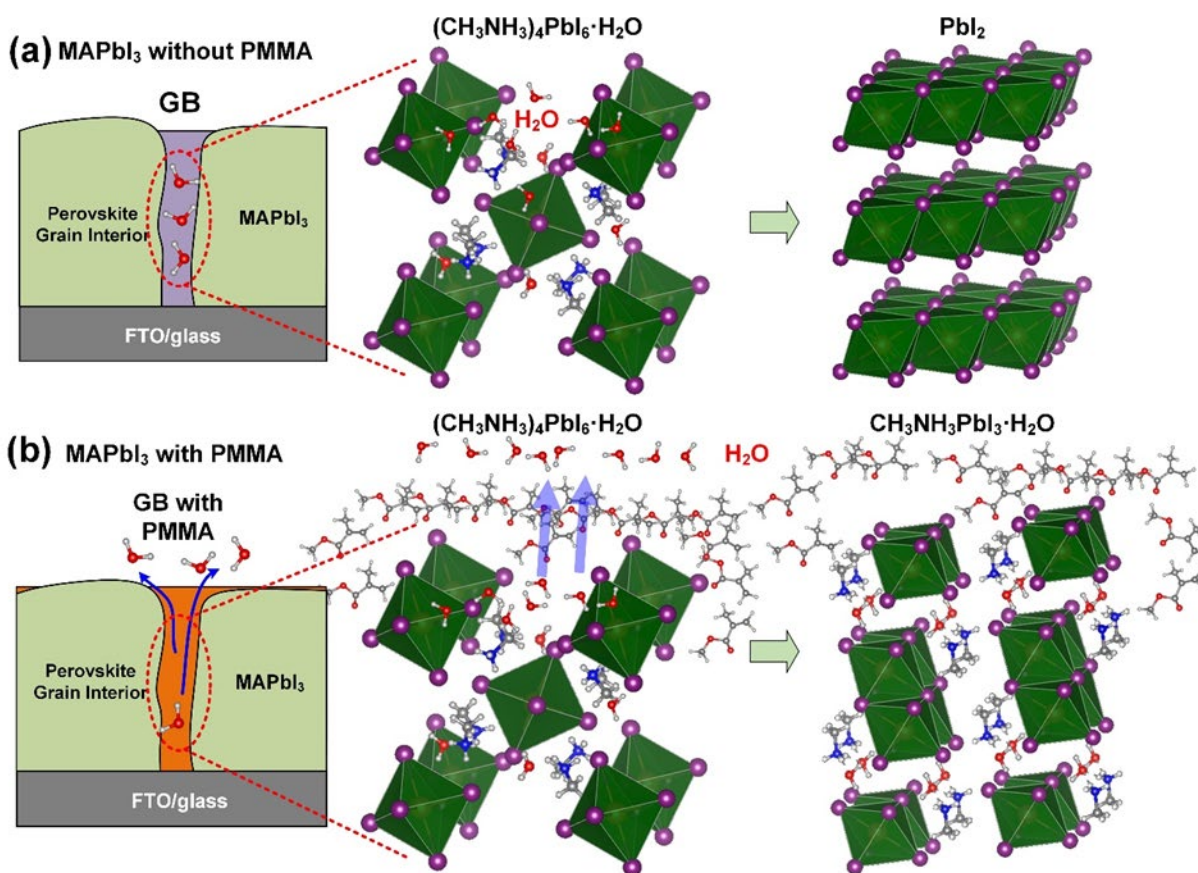
Fig. 25.  Thermal degradation models illustrating perovskite GBs (a) without PMMA and (b) with PMMA. Hydrated $(CH_3NH_3)_4PbI_6 \cdot H_2O$ will be dominant at GBs due to the high absorption of moisture during hot-casting. However, PMMA will have a key role in efficiently absorbing moistures and driving them out through GB channels. [10]

MAPbI$_3$ grains by hydrogen bonding and played a critical role in fully recovering the perovskite solar cells in a matter of minutes even after vapor exposure. We believe that PMMA played a similar role in absorbing moistures from perovskite films and subsequently driving out moisture from perovskites. Since there is abundant moisture at GBs, PMMA will efficiently absorb moisture

and drive it out through GB channels, which will reduce oxygen contents, as shown in Fig. 25 (b). In this case, the conceivable chemical reaction might be the conversion of hydrated $(CH_3NH_3)_4PbI_6 \bullet H_2O$ to monohydrated $CH_3NH_3PbI_3 \bullet H_2O$ and $H_2O$, as suggested by Song et al. [172]. However, the observed change of Pb/I ratio from 6 to 4.4 at GBs indicates incompletion conversion from $(CH_3NH_3)_4PbI_6 \bullet H_2O$ to $CH_3NH_3PbI_3 \bullet H_2O$. [10]

## 5.10 Summary

In summary, we have successfully introduced a polymer on perovskite thin film to achieve more than 1000 hours stable perovskite film under thermal stress at 85 °C. We investigated the underlying mechanism of how PMMA makes perovskite GBs to be thermally resistant. Perovskite films without PMMA decompose into $PbI_2$ and $I_2$, forming many pinholes at GBs and extending towards the grain interior. This is due to the presence of hydrated $(CH_3NH_3)_4PbI_6 \bullet H_2O$ at GBs of perovskites. Conversely, PMMA makes perovskite GBs thermally resistant by absorbing moisture from hydrated $(CH_3NH_3)_4PbI_6 \bullet H_2O$ GBs and driving them out through the GB channel. In addition, a high stability characteristic of PMMA (Tg=105°C) surrounding perovskite GBs can be considered an additional cause of protecting the perovskite from decomposition at elevated temperatures. We believe that continuous functionalization of perovskite GBs or crosslinking perovskite GBs with PMMA molecules might drastically render perovskite GBs chemically robust, resilient, and heat-resistant.

**CHAPTER 6**

**ENHANCEMENT OF THERMAL STABILTY OF MIXED CATION PEROVSKITE**

**THIN FILM WITH A POLYMER LAYER OF PMMA**

**6.1 Introduction**

Rapid advances in the photoconversion efficiency (PCE) of organic-inorganic perovskite solar cells (PSCs) have surged to a global record of 22.1% [8] from 3.8% in 2009 [14]. However, many researchers have found that the instability of perovskite materials presents a challenging problem to be resolved in the near future. The high sensitivity of perovskite materials to environmental factors greatly impacts device stability. In particular, perovskite materials are found to be sensitive to moisture, oxygen, UV light, electric field, heat, and many other factors [9,46,173]. For instance, the presence of moisture induces hydration of perovskite in which $CH_3NH_3PbI_3$ (MAPbI$_3$) perovskites hydrate into $CH_3NH_3PbI_3 \bullet H_2O$ or $(CH_3NH_3)_4PbI_6 \bullet H_2O$. [62,171,174]. In addition, oxygen facilitates electron transfer reactions with electron transport layers (e.g., TiO$_2$) which results in band bending and formation of trap states [108,175,176]. UV illumination in air causes oxygen to diffuse into the active perovskite absorber layer and buffer layers [150]. An electric field induces ion migration, which leads to electro-migration, compressive stress, and hysteretic effects [141]. In addition to light, moisture, and oxygen, perovskite materials undergo thermal degradation. High temperature induces $CH_3NH_3PbI_3$ perovskite to decompose into HI, $CH_3NH_2$, and PbI$_2$ [96]. In particular, thermally decomposed perovskite chemical components easily diffuse towards interfacial layers and electrodes which results in poor charge extraction and higher contact resistance [141].

The generic structure of perovskite materials used in PSCs comprises of $ABX_3$ where A is a univalent cation, that is, methylammonium (MA) $CH_3NH_3^+$, formamidinium (FA) $CH_2(NH_2)_2^+$, $Cs^+$, or $Rb^+$, while B stands for $Pb^{2+}$ or $Sn^{2+}$ and X for halides ($Cl^-$, $Br^-$, $I^-$). At the beginning of PSC research, $MAPbI_3$ has been extensively used as the light absorber; however, $FAbI_3$ attracted many due to its smaller bandgap and high heat resistance [96] although both $MAPbI_3$ and $FAPbI_3$ degrades quickly in ambient air even in encapsulated devices [177,178]. The need for absolute replacement of organic cations leads to the idea of using inorganic cesium lead halide, which showed excellent thermal stability [67]; however, $CsPbBr_3$ does not have a favorable bandgap for PV applications, and $CsPbI_3$ crystallizes in a photoinactive phase at room temperature and exhibits a photoactive stable perovskite phase only at temperatures above 300 °C [179] Unfortunately, due to the thermal or structural instability of pure perovskite compounds, there have been efforts to develop mixed cations and/or halide ions to overcome these limitations to achieve perovskite compounds with improved thermal stability and efficiency.

The recent progress in mixed cation-based perovskite exhibited that the highest efficiency perovskites were achieved with Pb-based and MA/FA mixed perovskites [63,180]. It has been demonstrated from this success that a small amount of MA in MA/FA mixture effectively induces the photoactive phase of FA perovskite, resulting in improved thermal stability and efficiency. However, even with very high efficiency solar cells, it is still difficult to obtain FA perovskite without the yellow phase even in the presence of MA [64]. The presence of yellow phases even in small quantities could influence crystal growth and charge collection, which in turn could affect device performance. The inorganic Cs cation has recently attracted attention to be included in mixed cation perovskites with a considerably smaller ionic radius than that of MA and FA cations [181]. Choi, et al. showed excellent improvement in PCE by using Cs/MA perovskites, which is

attributed to the improved light absorption, morphology, and increased energy difference between the active layer components [182]. In another study, Park and co-workers reported on Cs/FA mixtures with enhanced stability of heat, moisture, and light when compared to the pure FAPbI$_3$. [71] According to Yi, et al. this improved stability is attributed to lattice shrinkage and entropic stabilization [73]. Moreover, Saliba et al. showed improved stability and reproducibility by fabricating Cs/MA/FA solar cells with a stabilized PCE of 21.1% [69].

In addition, encapsulation of perovskites is an effective way to prevent degradation and different materials such as Al$_2$O$_3$, [183,184] poly(methyl methacrylate) (PMMA) and polycarbonate (PC) [174,185] have recently been investigated to achieve stability in perovskites. In particular, the use of polymer composites prepared from PMMA or PC mixed with poly(3-hexylthiophene-2,5-diyl) (P3HT) and carbon nanotubes lead to a thermal stability for up to 96 hrs under thermal treatment at 80 °C in air [174]. According to the work of McKenna et al. [155], a study of thermal stability using a number of polymers showed that PMMA performed as the best encapsulant among all polymers, extending the lifetime of the CH$_3$NH$_3$PbI$_{3-x}$Cl$_x$ film from 24 h to >400 h under continuous thermal treatment at 60 °C. Polymers such as polystyrene, PMMA, SWNT with PMMA, are known to act as insulating tunneling contacts and to passivate defects with an efficiency increase of over 18% in the perovskite solar cells [61]. It is well known that the grain boundaries (GBs) in perovskites are defective, which contains enriched oxygen concentration and iodine vacancies [186]. PMMA passivates the defects along grain boundaries (GBs), resulting in improved thermal stability of perovskite film by reducing defect states.

To date, the investigation of thermal stability of Cs/MA perovskites with PMMA incorporation is somewhat limited. It is evident that Cs/MA mixed perovskites exhibited better thermal durability when exposed at a higher temperature according to the work of Gu et al. [187].

They showed that for an un-encapsulated Cs/MA device, the PCE maintained about 75% of its original value under 80 min of heating at 140 °C in a dry atmosphere (RH ≤ 30%). Herein, we presented a study on MAPbI$_3$ perovskite without Cs$^+$ and with 5 and 9% Cs$^+$ incorporation into the cation to yield Cs$_{0.05}$MA$_{0.85}$PbI$_3$ and Cs$_{0.09}$MA$_{0.81}$PbI$_3$ perovskites when exposed to thermal stress of 85 °C and 120 °C. Moreover, the addition of PMMA on top of perovskite film to achieve thermally stable perovskite at 85 °C was explained thoroughly since PMMA has been proven to assist in improved stability and device performance by passivating defects. Although the operational temperature window of solar cells lies in the range of -40 to 85 °C, the original temperature could rise more than 100 °C any time depending on the location and environmental aspects. Therefore, a comparative study of perovskites with and without Cs under thermal stress at elevated temperature is presented in this report.

## 6.2 Effect of mixed cation (Cs) in thermal stability of perovskite thin film at 85 °C

Fig. 26 shows the thermal degradation of Cs$_x$MA$_{1-x}$PbI$_3$ perovskite films (x=0, 5, 9%) with different heat treatment times at 85 °C in a nitrogen-filled glove box. Among the three samples, MAPbI$_3$ perovskite film with no Cs before heat treatment exhibited the strongest XRD peaks at 14.08° and 28.44° corresponding to the (110) and (220) perovskite planes, as shown in Fig. 26 (a). However, the XRD intensities of (110) and (220) planes of Cs$_x$MA$_{1-x}$PbI$_3$ perovskite films decreased with increased Cs concentrations. Another observation is that the XRD peak at 20.2° along the (112) direction slightly increased with the increased Cs concentration due to the preferred crystal orientation of Cs along the thermodynamically stable direction of the (112) plane [188]. When Cs$_x$MA$_{1-x}$PbI$_3$ perovskite films underwent thermal treatment and were heat-treated, Cs$_x$MA$_{1-x}$PbI$_3$ perovskite films appeared to be degraded. Fig. 26 (b) and (c) show the XRD peaks

of $Cs_xMA_{1-x}PbI_3$ perovskites thermally treated at 85 °C for 72 hrs and 336 hrs. Obviously, two new XRD peaks appeared at 12.7° and 38.7°, corresponding to the (001) plane of $PbI_2$ and the (201) plane of $I_2$, respectively. In particular, as $Cs_xMA_{1-x}PbI_3$ perovskite films were heated for more than 72 hrs, the $PbI_2$ peak increased at an alarming rate, inferring a substantial degradation of the perovskite films. After 336 hrs of heating, the XRD peaks of $PbI_2$ and $I_2$ predominated whereas the XRD peaks of $Cs_xMA_{1-x}PbI_3$ perovskites almost disappeared. However, it can be seen that the degree of thermal degradation of three $Cs_xMA_{1-x}PbI_3$ perovskite films is slightly different with different Cs concentration. In order to quantitatively analyze the degree of thermal degradation of $Cs_xMA_{1-x}PbI_3$ films with different Cs concentrations, we calculate the degradation rate by following the procedure reported elsewhere [37], as shown in Fig. 26 (d). In this case, the decomposition rate of $Cs_xMA_{1-x}PbI_3$ was calculated by analyzing the XRD peak intensity ratio between the (001) $PbI_2$ peak and the (110) $Cs_xMA_{1-x}PbI_3$ peak. As shown in Fig. 26 (d), all three $Cs_xMA_{1-x}PbI_3$ perovskite films exhibited similar degradation rates up to 72 hrs. However, after more than 100 hrs of thermal treatments, the large deviation of the degradation rate was observed for the three $Cs_xMA_{1-x}PbI_3$ perovskite films. Notably, $Cs_xMA_{1-x}PbI_3$ perovskite film with x=5% Cs showed the best thermal stability. It should be noted that the $Cs_xMA_{1-x}PbI_3$ perovskite film with x=9% Cs exhibited lower thermal stability than the $MAPbI_3$ perovskite film. This might be due to an introduction of high concentration of Cs, resulting in the distorted crystallinity of $Cs_xMA_{1-x}PbI_3$ perovskite films. As shown in Fig. 26 (a), $Cs_xMA_{1-x}PbI_3$ with 9% Cs among the three samples showed the lowest XRD intensity of the (110) plane.
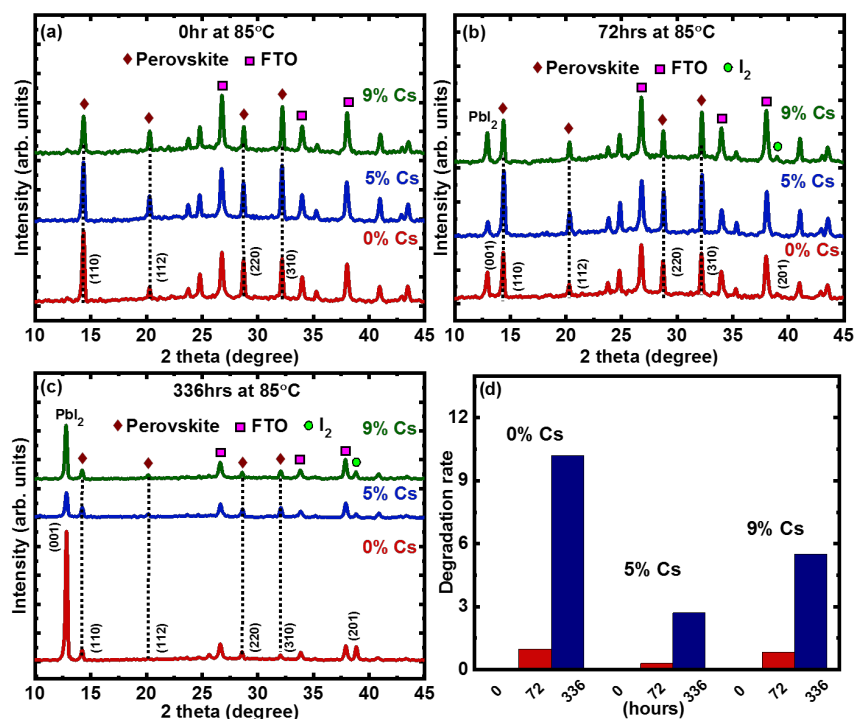
Fig. 26. XRD spectrum of $Cs_xMA_{1-x}PbI_3$ perovskite, where x = 0, 5, and 9% after (a) 0hr (b) 72hrs, and (c) 336 hrs of thermal treatment at 85 °C in a nitrogen filled glove box. (d) Degradation rate of perovskite films calculated by using the integrated XRD intensities of $PbI_2$ divided by (110) plane of $MAPbI_3$.

To investigate the morphological degradation of $Cs_xMA_{1-x}PbI_3$ during heat treatment, scanning electron microscopy (SEM) images were taken. Note that $Cs_xMA_{1-x}PbI_3$ films were fabricated using a hot-casting technique in which pre-heated glass slides more than 180 °C were quickly transferred to a spin-coater and promptly processed to fabricate large perovskite grains. Typically, a hot-cast method results in tens of micrometer morphologies of perovskite films. We did not observe any large discrepancies of surface morphologies of $Cs_xMA_{1-x}PbI_3$ perovskite films,

Fig. 27. SEM images of $Cs_xMA_{1-x}PbI_3$ perovskite without PMMA, where (a-c) x = 0%, (d-f) x = 5% and, (g-i) x = 9% after (a, d, g) 0hrs (b, e, h) 72hrs, and (c, f, i) 336 hrs of heating at 85 °C. Scale bar is 1 μm.

as shown in Fig. 27 (a), (d), and (g). This might be due to the small Cs concentration up to 9% which might induce noticeable variation of morphologies of perovskite films. Thermal degradation and formation of pin-holes initially occur around the grain boundaries (GBs) of perovskite films. In our previous studies [186], it has been shown that GBs contain non-stoichiometric perovskite chemistries with enriched oxygen, a number of defects and disordered chemical bonds. Thus, it is commonly observed that degradation starts from the GBs and propagates into the grain interiors (GIs). Therefore, SEM images were highlighted on the surface areas including the GBs to critically observe the development of thermally induced pin-holes. Fig. 27 shows surface morphologies of $Cs_xMA_{1-x}PbI_3$ films before and after heat treatment. Interestingly, all three samples start to develop

small pinholes on the surface after 72 hrs of heating (Fig. 27 (b), (e), and (h)) in which the distribution of small pinholes on the surface was similar. This is consistent with XRD measurement, showing similar decomposition rates in Fig. 26 (d). However, as the heat treatment time increased to 336 hrs, the pinholes became larger, and the number of pinholes increased, as shown in Fig. 27 (c), (f), and (i). From SEM images, it can be seen that $Cs_xMA_{1-x}PbI_3$ perovskite film with x= 5% Cs exhibited very thermal stability while $Cs_xMA_{1-x}PbI_3$ perovskite film with x= 9% Cs exhibited the poorest thermal stability.

## 6.3 Effect of polymer in thermal stability of mixed cation perovskite thin film at 85 °C

It should be noted that the pinholes are typically caused by the evaporation of MAI or $CH_3NH_2$ from the defective domains, leaving the film recrystallized as $PbI_2$ and $I_2$. Therefore, it is assumed that scaffolding of the defective domains can prevent thermal decomposition of perovskite films. Recently, to further thermally stabilize perovskite films, poly(methyl methacrylate) (PMMA) has been used in perovskite devices to protect against heat [155]. Mckenna, et al. [155] reported thermal degradation of PMMA treated perovskite films with a heating time of 29 hrs. They observed the progressive evolution of photoluminescence (PL) quenching regions with prolonged thermal aging. In contrast, Habisreutinger, et al. reported further improved thermal stability of $MAPbI_3$ film using carbon nanotube/PMMA composites up to 96 hrs at 80 °C in air [157]. However, the thermal stability of perovskite films with PMMA is still unsatisfactory and needs to be further enhanced. To explore the effect of PMMA on thermal stability of $Cs_xMA_{1-x}PbI_3$ perovskite films, PMMA thin layer was spin-casted on top of the $Cs_xMA_{1-x}PbI_3$ films at an rpm of 4000 at room temperature. Fig. 28 shows the XRD of $Cs_xMA_{1-x}PbI_3$ perovskite thin films with PMMA for up to 1000 hours of heating at 85 °C. Remarkably, we

did not observe any sign of degradation in $Cs_xMA_{1-x}PbI_3$ with PMMA after 336 hrs of heating while there is a negligible peak of $PbI_2$ under thermal treatment for 1000 hrs of healing. In addition, no XRD peak of $I_2$ at 38.7° was observed from XRD measurement. This is in stark contrast to $Cs_xMA_{1-x}PbI_3$ perovskite films without PMMA that rapidly degraded and decomposed to $PbI_2$ and $I_2$ after 72 hrs of healing.
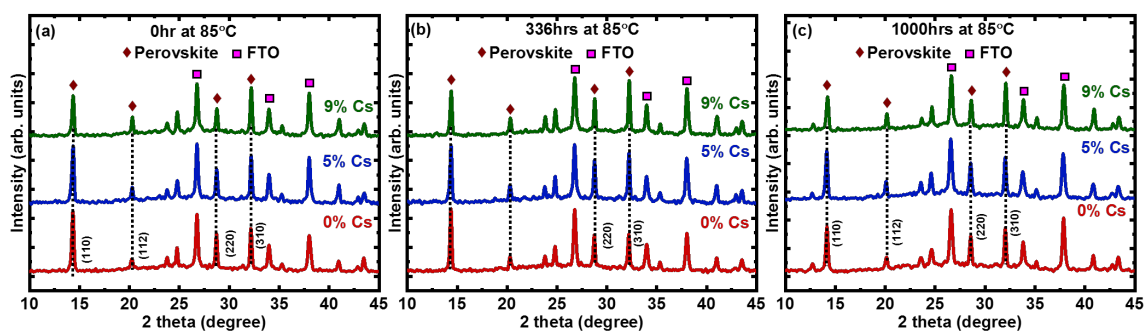


Fig. 28.  XRD spectrum of $Cs_xMA_{1-x}PbI_3$ perovskite with PMMA, where x = 0, 5, and 9% after (a) 0hrs (b) 336hrs, and (c) 1000hrs of heating at 85 °C.

Fig. 29 (a), (d), and (g) shows evolution of SEM images of $Cs_xMA_{1-x}PbI_3$ with PMMA with different heating times. Again, all three $Cs_xMA_{1-x}PbI_3$ perovskite films before heating exhibited similar morphologies. Remarkably, we did not see any degradation or noticeable pinholes of $Cs_xMA_{1-x}PbI_3$ perovskite films with PMMA after 336 hrs of heating, as shown in Fig. 29 (b), (e), and (h). Without PMMA, the entire surface of all three perovskite films was covered by a number of pinholes caused by thermal decomposition. However, even after 1000 hrs of

heating, extensive pinholes around GB were not observed for all three samples, as shown in Fig. 29 (c), (f), and (i) . This clearly indicates that PMMA suppressed the thermal decomposition of perovskite films and prevented the formation of pin-holes. Note that the glass transition temperature ($T_g$) of PMMA is around 105 °C [155]. Therefore, it is assumed that the PMMA polymer on top of perovskite films inhibited the loss of perovskite chemistries and prevented the thermal decomposition of perovskite films.



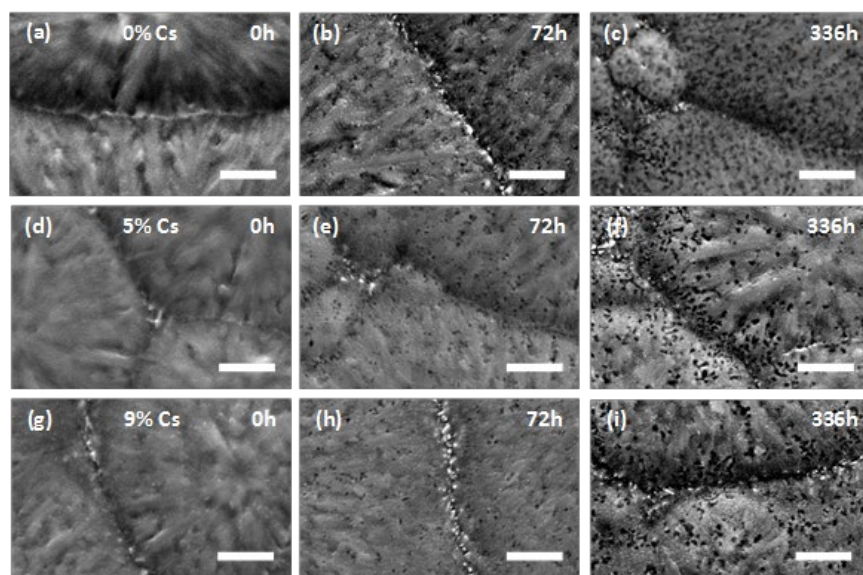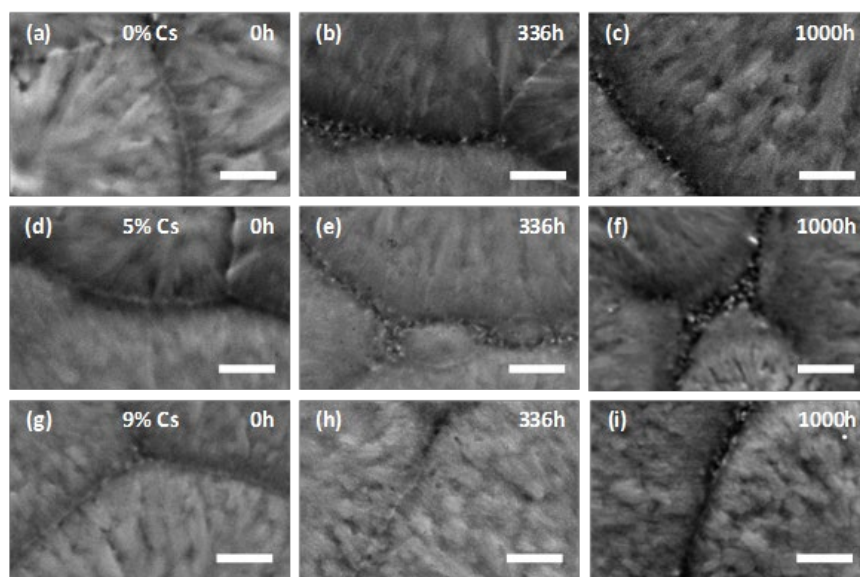Fig. 29.  SEM images of $Cs_xMA_{1-x}PbI_3$ perovskite with PMMA, where (a-c) x = 0%, (d-f) x = 5% and, (g-i) x = 9% after (a, d, g) 0hrs (b, e, h) 336hrs, and (c, f, i) 1000hrs of heating at 85 °C. Scale bar is 1 μm.

**6.4 Thermal stability of mixed cation perovskite thin film with polymer at 120 °C**

To probe the thermal stability of perovskite films at a temperature higher than $T_g$= 105°C, the heating temperature of perovskite films was raised to 120 °C. Fig. 30 (a) shows the XRD spectra of $Cs_xMA_{1-x}PbI_3$ perovskite films with PMMA heated at 120 °C for up to 72 hrs. With the thermal treatment, the XRD (110) and (220) planes for $Cs_xMA_{1-x}PbI_3$ film sharply decreased whereas the degradation characteristic peak of $PbI_2$ at 12.7° became prominent for all samples. In particular, $Cs_xMA_{1-x}PbI_3$ with 5% Cs exhibited better thermal stability compared to $Cs_xMA_{1-x}PbI_3$ with 0 and 9% Cs. Moreover, the XRD intensity of $I_2$ peak at 38.7° is lowest for $Cs_xMA_{1-x}PbI_3$ 5% Cs based perovskite thin film.
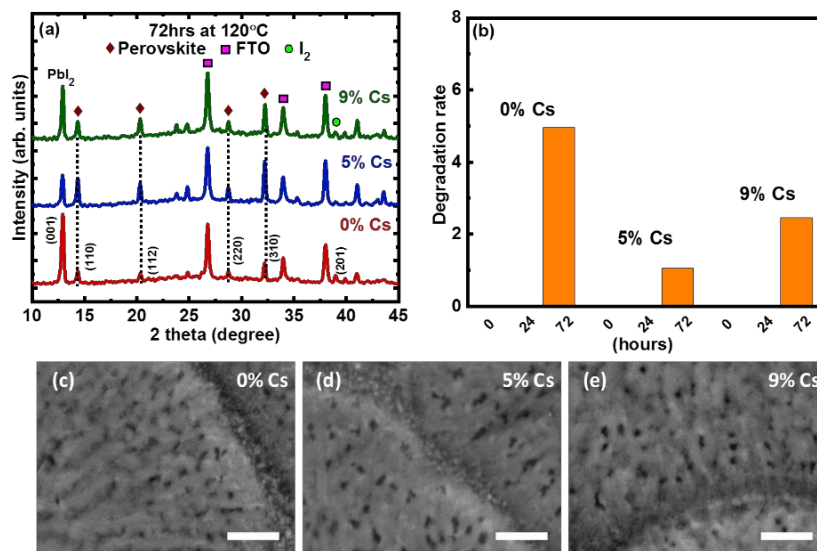


Fig. 30.  (a) XRD spectrum of $Cs_xMA_{1-x}PbI_3$ perovskite with PMMA, where x = 0, 5, and 9% after 72hrs of heating at 120 °C (d) Degradation rate of same sample set calculated by using the intensity

of PbI$_2$ divided by MAPbI$_3$ (110). SEM images of Cs$_x$MA$_{1-x}$PbI$_3$ perovskite with PMMA, where (c) x = 0%, (d) x = 5% and, (e) x = 9% after 72hrs of heating at 120 °C. (Scale bar is 1 μm.)

We also calculated the degradation rate by analyzing integrated XRD intensity ratios of the PbI$_2$/Cs$_x$MA$_{1-x}$PbI$_3$ (110) plane. Fig. 30 (b) shows the resultant degradation rate, which confirmed that Cs$_x$MA$_{1-x}$PbI$_3$ with 5% Cs exhibited better thermal stability. The degradation rate of 5% Cs based perovskite film with PMMA is 350% and 130% lower than that of 0 and 9% Cs, respectively. Therefore, this result indicates that PMMA is not effective to prevent thermal degradation at a temperature higher than Tg=105°C. In addition, the SEM images of Fig. 30 (c), (d), and (e) confirm that perovskite is decomposed into PbI$_2$ forming many pinholes, which correlates to the XRD spectrum observed in Fig. 30 (a).

## 6.5 Summary

In conclusion, we investigated a thermal stability study of Cs$_x$MA$_{1-x}$PbI$_3$ perovskite films with and without PMMA at 85 °C and 120 °C. The XRD analysis of Cs$_x$MA$_{1-x}$PbI$_3$ perovskite films reveals that without PMMA Cs$_x$MA$_{1-x}$PbI$_3$ perovskite films rapidly underwent thermal degradation processes forming PbI$_2$ and I$_2$ at 85 °C. At the same time, we observed such thermal degradation was accompanied by formation of a number of pin-holes on the surface of Cs$_x$MA$_{1-x}$PbI$_3$ films. Therefore, it can be inferred that the decomposition of perovskite films led to the loss of MAI, resulting in recrystallized byproducts of PbI$_2$ and I$_2$. Thus, an addition of Cs cation could not suppress thermal degradation upon heating at 85 °C. However, we observed the slightly better thermal stability with 5% Cs concentration. With the addition of PMMA on top of perovskites, we observed excellent thermal stability of Cs$_x$MA$_{1-x}$PbI$_3$ films based on XRD and SEM

measurements, crystallinity and morphologies of $Cs_xMA_{1-x}PbI_3$ with PMMA maintained high quality up to 1000 hrs of thermal treatment at 85 °C. This can be interpreted to mean that a PMMA polymer might serve as a scaffold to effectively prevent thermal decomposition and evaporation of perovskite chemistries. However, when $Cs_xMA_{1-x}PbI_3$ films with PMMA were thermally treated at a higher temperature of 120 °C, we observed the prompt thermal degradation of $Cs_xMA_{1-x}PbI_3$ films. This is because the thermal treatment temperature of 120 °C is higher than the glass transition temperature (105 °C) of PMMA. At 120 °C, PMMA did not prevent the thermal decomposition and evaporation of perovskite films. However, it is apparent from the crystal and morphological analysis that incorporation of a small amount of Cs increases the thermal stability of $Cs_xMA_{1-x}PbI_3$ perovskites at elevated temperatures for a prolonged period. We found that the perovskite film with 5% of Cs concentration showed moderately better thermal stability upon heating at 120 °C for 72 hours. These results indicate that incorporation of Cs cation into MA and the addition of PMMA on top of perovskite assists in obtaining thermally stable perovskite films at higher temperature.

**CHAPTER 7**

**ESTABLISHING THERMALLY STABLE PEROVSKITE SOLAR CELLS**

**7.1 Introduction**

In a typical perovskite solar cell, perovskite thin film is sandwiched between the electron and the hole transport layers. Perovskite thin films are very susceptible in oxygen and moisture though different cations and mixed halides have been employed in perovskite structures. As mentioned in previous chapters, hot casted perovskite thin films contain defective grain boundaries. Under thermal heating the defective GBs form many pinholes which create a direct shunt path between the electron and the hole transport layer. It has also been reported that the GBs are characterized by an enriched oxygen concentration, and iodide vacancies, which results in deep defect recombination centers at GBs unfavorable to PSCs performance. Therefore, to establish a thermally stable perovskite solar cells, the conventional fabrication method of perovskite solar cells was implemented. This method eliminates the leaf like grain structure of perovskite that is typically found in a hot-casing technique and provides a smooth perovskite film with compact grains.

Perovskite solar cells require protection from environmental factors such as heat, moisture, air, etc. As discussed in previous chapters, researchers have been extensively investigating several methods to achieve thermal stability of perovskite solar cells. A solution to this is encapsulation with polymers to protect perovskites from moisture. Polymers such as poly (methyl methacrylate) (PMMA), polystyrene, polyimide have been used to protect perovskite films from oxygen and moisture. Along with protection from air, polymers like polystyrene, PMMA, SWNT with PMMA

act as an insulating tunneling contact and passivates defects in perovskite film by increasing efficiency. Herein, we have studied the effect of polyimide as an encapsulation layer on top of perovskite solar cells to establish thermally stable perovskite solar cells.

## 7.2 Optimization of perovskite film

The nature of grain boundaries has been investigated in many reports [186] and it is proven that the degradation of perovskite materials in moisture, light, and heat primarily originates from the GBs through the release of volatile gases. Theoretically, GBs are characterized by shallow intrinsic levels and are considered to be benign [189]; however, in a theoretical calculation Agiorgousis et al. found that the deep charge-state transition levels within the bandgap were indeed possible by forming Pb dimers and I trimmers through very strong covalent bonds [190]. Experimental studies also revealed controversial results on the nature of GBs in perovskite materials. In another work from my research group, it was suggested that GBs of hot-casted perovskite films contain deep defect centers that might serve as recombinant centers and be detrimental to the perovskite solar cells [186]. Hence, these defective GBs are prone to degradation when exposed to environmental factors making perovskite solar cells unstable. Many GB passivation approaches such as advanced fabrication, fullerene or polymer incorporation, using Lewis acids and/or bases have been proven to enhance the photovoltaic performance and stability of PSCs due to the reduction of defects [191].
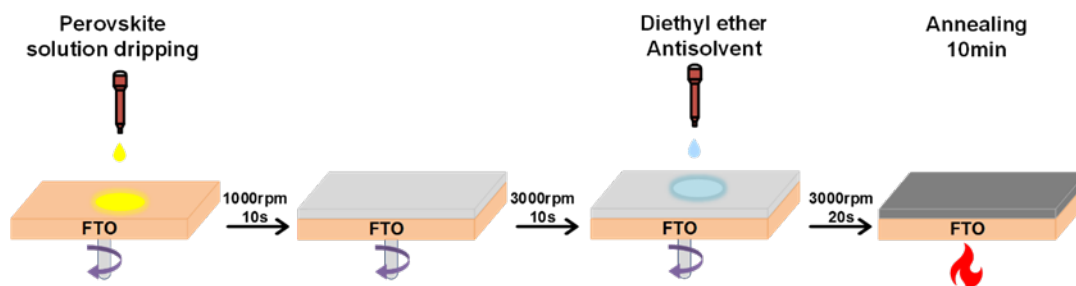
Fig. 31. Schematic of perovskite film formation using an antisolvent approach.

Perovskite films prepared in a hot-casting technique show leaf-like structure with deep and defective grain boundaries. Herein, we adopt an antisolvent approach which is one of the most popular methods in perovskite fabrication technique. The method was first proposed by Spiccia et al. [28] and Seok et al. [36]. The process involves dropping an antisolvent at a critical stage during the spin coating process enabling the formation of uniform films with large grains. Fig. 31 illustrates the method of the film fabrication. A precursor solution with $PbI_2$ : MAI : DMSO (1:1:1) in DMF was used. The precursor solution was dropped in a substrate and spun coated at a dynamic spin speed. Diethyl ether was dropped as an antisolvent after a critical time. The best film obtained after antisolvent washing was a transparent film suggesting the formation of adduct. The film became highly reflective after annealing for 10min in air.
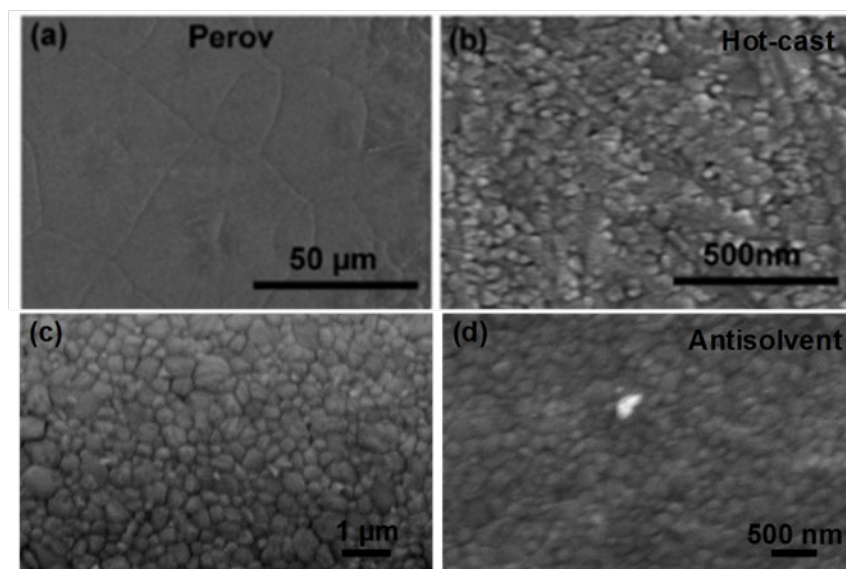
Fig. 32. SEM image of perovskite with (a) lower and (b) higher magnifications fabricated by a hot casting technique. SEM image of perovskite with (c) lower and (d) higher magnification fabricated by antisolvent approach exhibiting finer and densely packed grains.

Fig. 32 shows the scanning electron microscope image of perovskite film comparing two perovskite fabrication methods: hot-casting and the antisolvent approach. Fig. 32 (a) shows a SEM image of $MAPbI_{3-x}Cl_x$ and exhibits large grains with leaf-like structure of several tens of micrometers typical of a hot-casting technique. However, a high-resolution SEM image revealed grainy morphologies, as shown in Fig. 32 (b). In contrast, the SEM image of perovskite film fabricated using an antisolvent approach shows smooth and compact grains in nanoscale; however, no leaf like structures in microscale are observed.

**7.3 Perovskite solar device with polymer encapsulation**

Perovskite solar cells were fabricated having the device structure of FTO/NiO/MAPbI$_3$/C60/C60:C/Ag, as shown in Fig. 33 (a). Photoactive MAPbI$_3$ perovskite films were fabricated using the antisolvent approach on FTO/NiO substrate. C60, carbon, and Ag were deposited using the E-beam evaporation technique. To study the thermal stability of perovskite solar devices, an encapsulation layer of polyimide was deposited on top of silver. Fig. 33 (b) shows the current (J)–voltage (V) characteristics of MAPbI$_3$ solar cell. The short-circuit current (J$_{SC}$), open circuit voltage (V$_{OC}$) and fill factor (FF) were 21.95 mAcm$^{-2}$, 0.97 V and 0.65, resulting in a power conversion efficiency (PCE) of ~14% at room temperature.
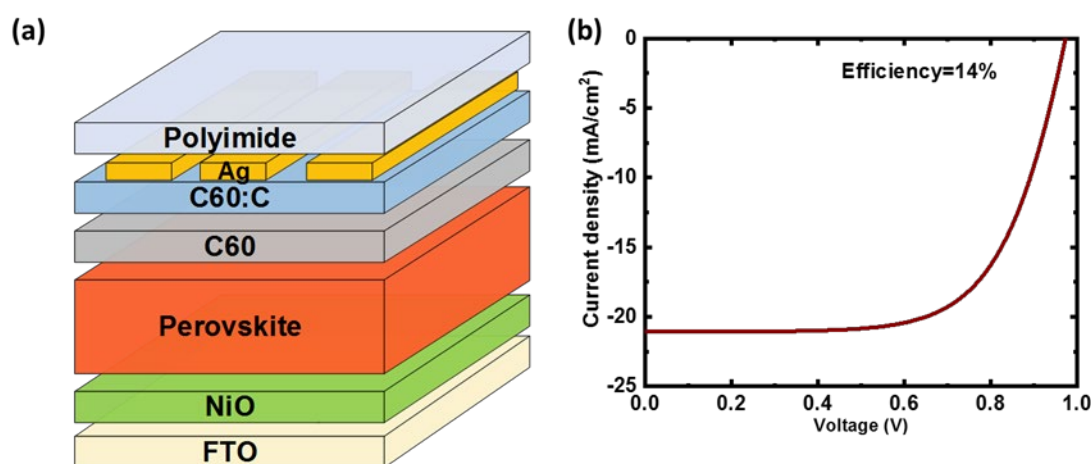


Fig. 33.    (a) Inverted p–i–n perovskite solar cell structure and (b) Current–voltage J–V characteristics of perovskite solar cells exhibited a PCE of 14% at room temperature.

**7.4 Thermal Stability Study**

A thermal stability study was conducted on perovskite solar devices with and without polyimide encapsulation. The fabricated perovskite solar cells with and without polyimide encapsulation were heated inside a glove box at a temperature of 85 °C, and the photovoltaic parameters and the film characteristics such as XRD, UV-Vis, and SEM images were analyzed to realize the underlying mechanism of stability of perovskite solar cells with polyimide encapsulation.

**7.4.1 J-V characteristics**

Preliminary thermal stability investigation was conducted on MAPbI$_3$ perovskite solar cells with and without polyimide. To demonstrate consistent photovoltaic performance with time, the average device parameters were calculated from the current density-voltage characteristics measured under 100 mW/cm$^2$ illumination using an AM 1.5G filter in an atmospheric environment. The average values (with standard deviation) of normalized PCE, fill factor (FF), short-circuit current density J$_{SC}$, and open circuit voltage V$_{OC}$ for MAPbI$_3$ perovskite solar cells with and without polyimide with the evolution of heating time are shown in Fig. 34. The photovoltaic parameters of solar cells without polyimide encapsulation initially tend to increase with heating time; however, a rapid decrease in performance is observed after 4 days of heating. The initial increase in performance could be because of the passivation of defects due to light soaking. In contrast, the solar cells with polyimide encapsulation could retain its initial efficiency for more than one month when heated at 85 °C in a nitrogen filled glove box. Hence, polyimide encapsulation layer prevents the solar cells from degradation under thermal heating. We hypothesize that when the perovskite solar cells with polyimide are heated in a nitrogen

environment, polyimide diffuses through the perovskite film passivating the defects. In addition, the water repellant characteristics of polyimide make it suitable in preventing degradation due to thermal heating.
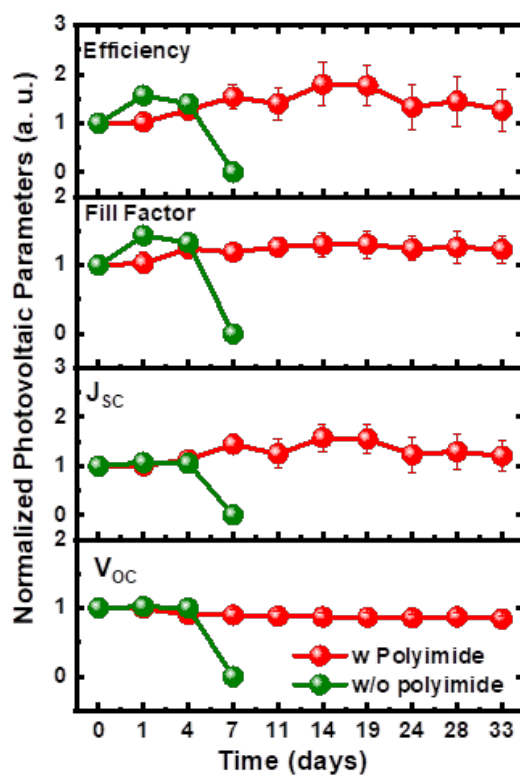


Fig. 34. The evolution of the normalized photovoltaic parameters of photo conversion efficiency (PCE), fill factor (FF), short circuit current density (Jsc), and open circuit voltage (Voc) of perovskite solar cells with and without polyimide encapsulation.
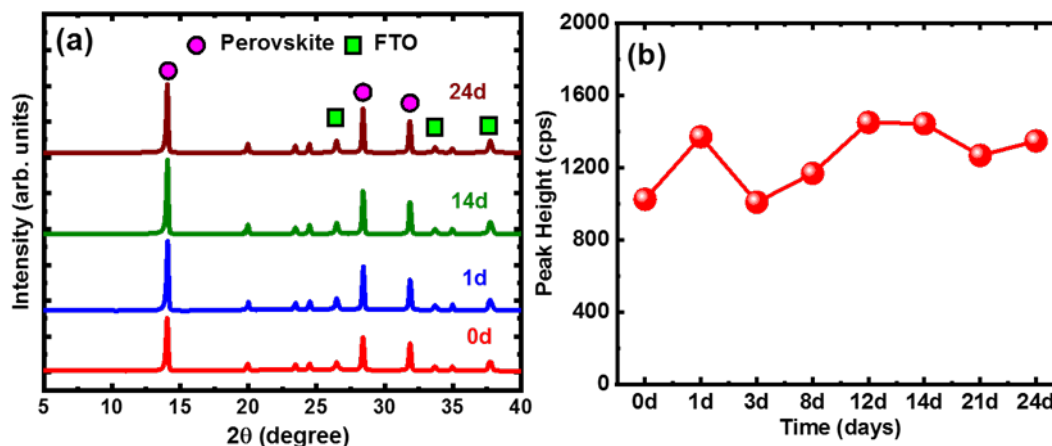
Fig. 35. (a) The time evolution of XRD spectra of MAPbI$_3$ with polyimide at 85 °C. (b) The integrated peak intensity of MAPbI$_3$ along (110) direction for MAPbI$_3$ sample with polyimide.

### 7.4.2 XRD characteristics

To investigate the thermal stability of the Perovskite films with polyimide layer, X-ray diffraction measurements were performed for up to 24 days heated at 85 °C, as shown in Fig. 35 (a). The fresh Perovskite film contains two prime Perovskite peaks located at 14° and 28.4° originated from the same families of the crystallographic plane along the (110) and (220) directions. The intensity along the (110) direction is superior to the (220). The presence of FTO can be seen at 26.8°, 33°, 37°. Interestingly, the perovskite related peak at scattering angles 14.3°, 28.8°, and 32.1° increased with increased heating time. This confirms the improvement of crystallinity in MAPbI$_3$ film with polyimide after heating which is most likely due to the passivation of defects in perovskite film with the diffusion of polyimide into perovskite. Fig. 35 (b) shows the integrated intensities of the perovskite peak along the (110) direction. The integrated

area of the (110) perovskite peak is used as a representative parameter for the volume fraction of the perovskite as a function of time. The sample with polyimide retains the XRD peak intensity of the perovskite peak along the (110) direction for a prolonged heating time.

### 7.4.3 UV-vis characteristics

We also measured UV-vis absorption for the fresh samples and the samples after heat treatment. Fig. 36 (a) and (b) compares the absorbance of perovskite samples with and without polyimide heated at 85 °C. The absorbance spectra clearly reveal the degradation of $MAPbI_3$ without polyimide over time. However, the absorption spectra of $MAPbI_3$/ polyimide film displayed a nearly identical pattern before and after heating at 85 °C. Moreover, the absorption bandedge shifts dramatically for the sample without polyimide, which can be observed from the optical bandgap $E_g$. Davis and Mott's work [164,192] on amorphous silicon shows that the optical absorption strength depends on the difference between photon energy and the bandgap as follows:

$$(\alpha h v)^{1/n} = A(h v - E_g) \qquad (14)$$

where, $h$ is Planck's constant, $v$ is the photon's energy, $\alpha$ is the absorption coefficient, $E_g$ is the bandgap, and A is a proportionality constant. The value of the exponent denotes the nature of the electronic transition, considered as n=1/2 for direct allowed transition in the case of perovskite. Fig. 36 (c) and (d) show the optical bandgap determined from the extrapolation of the linear part of a Tauc plot [193]. The value of optical bandgap for $MAPbI_3$ sample is 1.59 eV in consistent with the previous report. [167] Interestingly, the bandgap shifts from 1.59eV to 1.58eV after heating for 4 days in the case of the $MAPbI_3$ sample without polyimide, while a nominal change of optical bandgap is observed for $MAPbI_3$ with the polyimide sample. The minimal change in

optical bandgap is consistent with the crystal structure analysis and suggests that the polyimide

layer works as a protective layer and increases thermal stability.
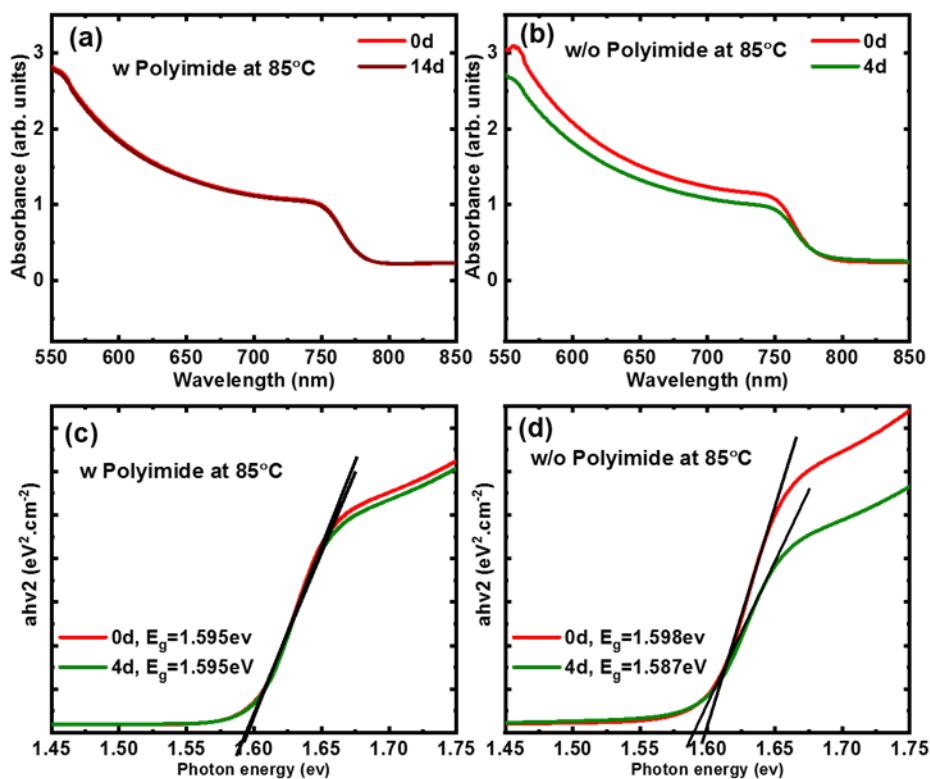


Fig. 36. Absorption spectra as a function of wavelength for MAPbI₃ sample (a) with polyimide

and (b) without polyimide. Tauc plots of optical coefficient $(\alpha h\nu)^2$ *vs.* photon energy (hν) for (c)

MAPbI₃ with polyimide and (d) MAPbI₃ without polyimide.
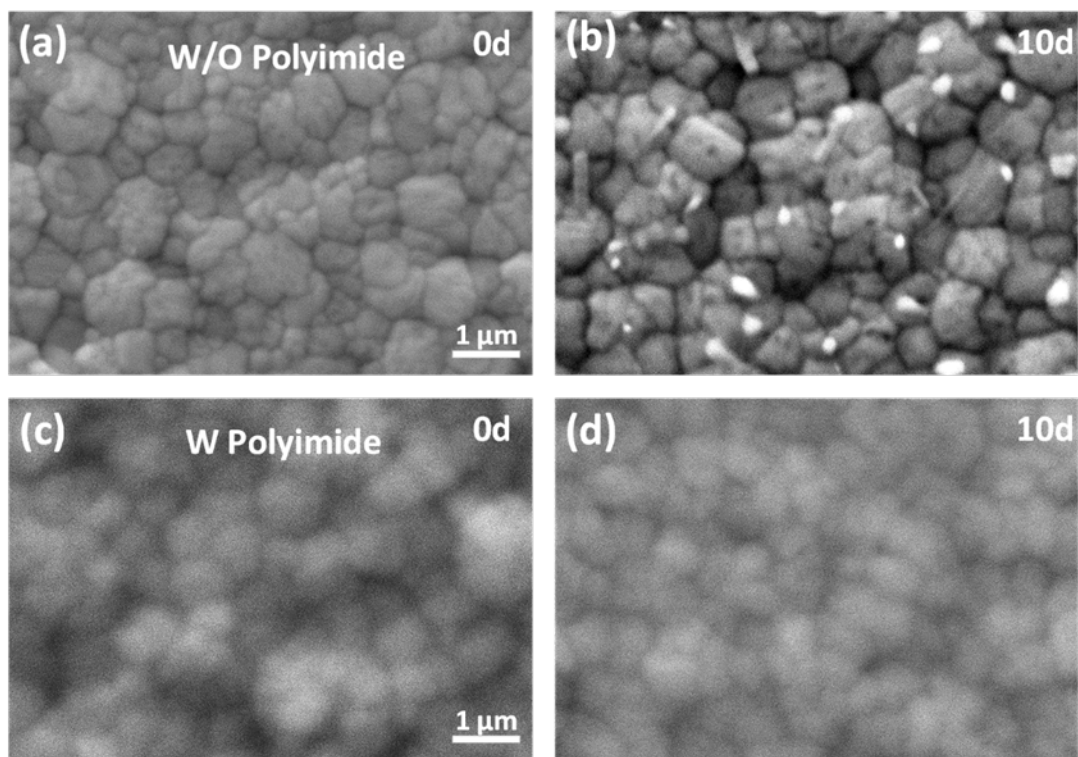
Fig. 37. SEM images of MAPbI$_3$ without polyimide (a) no heating at 0 day (b) after 10 days at 85 °C, and SEM images of MAPbI$_3$ with polyimide (c) no heating at 0 day (d) after 10 days at 85 °C. (Scale bar: 1 μm)

### 7.4.4 Morphological characteristics

SEM imaging of a perovskite sample with and without polyimide was performed before and after heating at 85 °C with the evolution of time. Before thermal treatment, both films were flat with no pinholes. The SEM image in Fig. 37 (a) and (b) proves the degradation of MAPbI$_3$ in the form of pinholes and decomposed particles (bright white particles) after 10 days of heating. Interestingly, the MAPbI$_3$ film with polyimide showed smoother grains after heating for 10 days

at 85 °C. As shown in Fig. 37 (c) and (d), MAPbI$_3$ film with polyimide showed improved crystallinity in the morphological analysis. This result agrees with the XRD results that polyimide increases the crystallinity of MAPbI$_3$ film when heated at 85 °C in a nitrogen environment. Therefore, incorporation of polyimide on MAPbI$_3$ solar cells could retain its initial stability for more than one month of heat exposure.

## 7.6 Summary

To summarize, a thermally stable perovskite solar cell was demonstrated using an encapsulation layer of polyimide. The polyimide coated solar cell was able to maintain its initial photo conversion efficiency for more than one month under continuous thermal heating. The incorporation of the polyimide layer passivates the defect and improves the crystallinity of the perovskite film, which is evident by the XRD, UV-vis and SEM measurements.

**CHAPTER 8**

**CONCLUSIONS**

## 8.1 Achieved Results

While organometal halide perovskite solar cells show great potential to meet future energy needs, thermal instability raises serious questions about commercialization viability. At present, the stability of perovskite solar cells has been studied in various environmental conditions including humidity and temperature. Nonetheless, an understanding of the performance of a $CH_3NH_3PbI_{3-x}Cl_x$ perovskite solar cell is limited. This study reports the irreversible performance of $CH_3NH_3PbI_{3-x}Cl_x$ perovskite solar cell during the heating and cooling processes under AM 1.5 and reveals what triggers irreversible performance of the solar cell. In particular, the primary cause of irreversible performance of $CH_3NH_3PbI_{3-x}Cl_x$ is quantitatively analysed by monitoring in real time the development of deteriorated crystallinity, charge trapping/detrapping, trap depth, and $PbI_2$ phase, namely a critical signal of perovskite degradation while varying the temperature of perovskite film and the solar cell. Most surprisingly, it is revealed that the degradation of both perovskite films and solar cells was triggered at ~70 °C. Remarkably, even after the device temperature cooled down to room temperature, degraded performance of solar cells persisted with increasing charge trapping and further development of the $PbI_2$ phase, which led to irreversible J-V characteristics of the perovskite solar cell.

Perovskite film decomposes into $PbI_2$ with thermal heating at 85 °C; therefore, we primarily concentrated on fabricating a thermally stable perovskite thin film. Thermal instability of perovskite films is one of the important issues limiting the outdoor application of perovskite

solar cells because perovskite films are intrinsically thermally unstable under normal operating temperature. We explore the new role of poly (methyl methacrylate) (PMMA) that alters $CH_3NH_3PbI_3$ (MAPbI$_3$) grain boundaries (GBs) so that they are more heat-resistant. It is found that hot-casted MAPbI$_3$ films contain GBs composed of hydrated $(CH_3NH_3)_4PbI_4 \bullet H_2O$, while grain interiors (GIs) are mainly composed of $CH_3NH_3PbI_3$. Upon heating bare MAPbI$_3$ film at 85 °C up to 1000 hrs in a nitrogen environment, thermal degradation of MAPbI$_3$ started at GBs and extended into GIs. Such a degradation pathway can be explained by hydrated $(CH_3NH_3)_4PbI_4 \bullet H_2O$ structures where moisture at GBs acts as a catalyst for thermal degradation at GBs. Conversely, when PMMA was applied to MAPbI$_3$, a new level of thermal stability of MAPbI$_3$/PMMA was achieved where PMMA altered the perovskite GB to be thermally resistant. Remarkably, the high thermal stability of perovskite GBs is attributed to the newly discovered role of PMMA in absorbing moisture from hydrated $(CH_3NH_3)_4PbI_4 \bullet H_2O$ GBs and driving them out through GB channels and the high stability characteristics ($T_g$=105 °C) of PMMA scaffolding perovskite GBs.

Perovskite thin film is stable at 85 °C for up to 1000 hrs with the application of PPMA. Subsequently, we incorporated mixed cation into perovskite thin film to realize the role of mixed cation in the thermal stability of perovskite film. In this context, we investigated the thermal stability of Cs$_x$MA$_{1-x}$PbI$_3$ (Cs=0, 5, and 9%) with and without PMMA at thermal treatment temperatures of 85 °C and 120 °C in a nitrogen filled glove box. Without PMMA coating, it is found that all Cs$_x$MA$_{1-x}$PbI$_3$ films rapidly degraded by producing byproducts of PbI$_2$ and I$_2$ and forming a number of pin-holes even though Cs$_x$MA$_{1-x}$PbI$_3$ with 5% Cs exhibited slightly better thermal stability. In particular, it is found that degradation started within 72 hrs of thermal treatment and exhibited extensive thermal degradation after 300 hrs at 85 °C. However, when a PMMA polymer was introduced on top of the Cs$_x$MA$_{1-x}$PbI$_3$ perovskite films, we achieved

remarkable thermal stability up to 1000 hrs of thermal heating at 85 °C with no significant sign of thermal decomposition to $PbI_2$ and $I_2$ and of pin-holes on the surfaces. However, it is found that when $Cs_xMA_{1-x}PbI_3$ films with PMMA were heated at a temperature of 120 °C higher than the glass transition temperature (105 °C) of PMMA, the rapid thermal degradation of $Cs_xMA_{1-x}PbI_3$ was observed, producing $PbI_2$ and $I_2$ and forming many pin-holes on the surface. This indicates that PMMA serves as an excellent scaffold to prevent the thermal degradation of $Cs_xMA_{1-x}PbI_3$ films at a temperature lower than the glass transition temperature ($T_g$) of PMMA but not at higher than $T_g$ of PMMA. Our findings suggest that $Cs_xMA_{1-x}PbI_3$ perovskite with PMMA is one of the possible solutions for better thermal stability in perovskites at higher temperature.

Until now, we have fabricated a perovskite solar cell using the hot casting technique. Though hot casting technique-based perovskite solar cells showed high efficiency, deeper grain boundaries were observed. Grain boundaries are considered to be where degradation starts in the perovskite thin film under thermal stress. Thermal degradation starts from the grain boundary and extends towards the grain interior. Hence, we have fabricated perovskite thin film in a conventional antisolvent method which does not contain any large grain boundary as observed in a hot casting technique. Also, we incorporated a new polymer polyimide in the solar cell as polyimide has higher glass transition temperature than PMMA. In addition, polyimide can repel moisture from the surface of perovskite solar cells and removes defects in perovskite thin film which helps improve thermal stability. The perovskite solar cell with polyimide showed thermal stability for more than one month when heated at 85 °C while solar cells without polyimide degraded within 72hrs.

**8.2 Future works**

We have incorporated polyimide on top of a perovskite solar cell which works as a water repellant and passivates defects. In addition, it is believed that the excellent hygroscopicity of PMMA played an active role in absorbing moisture from hydrated $(CH_3NH_3)_4PbI_6 \bullet H_2O$ GBs, driving them out through the GB channel. This might make the GBs less susceptible to moisture. Moreover, mixed cation based perovskite has higher stability than single cation perovskite at a higher temperature as inorganic cations are less prone to degrade in heat. In this thesis, we fabricated solar cells with the configuration of FTO/NiO/Perovskite/C60/C60:C/Ag/Polyimide. Further improvement can be achieved by adding PMMA, polyimide and mixed cation which could improve stability. Perovskite solar cells are not only unstable under thermal heating but also tend to degrade in air. The water contact angle of polyimide can be increased up to 162° [194]. Consequently, a mixed cation perovskite solar cell with PMMA and polyimide could have air and thermal stability which would be a potential candidate in order to commercialize perovskite solar cells.

# REFERENCES

[1] U.S. Environmental Protection Agency, *Inventory of U.S. Greenhouse Gas Emissions and Sinks: 1990-2018*, April 2020. Includes U.S. Territories.

[2] U.S. Energy Information Administration, *Monthly Energy Review*, Environment, July 2020, preliminary data.

[3] U.S. Energy Information Administration, Monthly Energy Review, Appendix D.1, and Tables 1.1 and 10.1, April 2020, preliminary data for 2019

[4] U.S. Energy Information Administration, Monthly Energy Review, Table 1.3 and 10.1, April 2020, preliminary data.

[5] Green, M.A., Wenham, S.R., Zhao, J., Zolper, J. and Blakers, A.W., 1990, May. Recent improvements in silicon solar cells and module efficiency. In IEEE Conference on Photovoltaic Specialists (pp. 207-210). IEEE.

[6] Chapin, D.M., Fuller, C.S. and Pearson, G.L., 1954. A new silicon p-n junction photocell for converting solar radiation into electrical power. Journal of applied physics, 25(5), pp.676-677.

[7] Meng, L., You, J. and Yang, Y., 2018. Addressing the stability issue of perovskite solar cells for commercial applications. Nature communications, 9(1), pp.1-4.

[8] NREL Solar Cell Efficiency Chart. http://www.nrel.gov/ncpv/. (accessed on March 7, 2021).

[9] Al Mamun, A., Ava, T.T., Byun, H.R., Jeong, H.J., Jeong, M.S., Nguyen, L., Gausin, C. and Namkoong, G., 2017. Unveiling the irreversible performance degradation of organo-inorganic halide perovskite films and solar cells during heating and cooling processes. Physical Chemistry Chemical Physics, 19(29), pp.19487-19495.

[10] Ava, T.T., Jeong, H.J., Yu, H.M., Lee, K.N., Abdel-Fattah, T.M., Jeong, M.S. and Namkoong, G., 2021. Role of PMMA to make MAPbI$_3$ grain boundary heat-resistant. Applied Surface Science, 558, p.149852.

[11] Jeon, N.J., Noh, J.H., Kim, Y.C., Yang, W.S., Ryu, S. and Seok, S.I., 2014. Solvent engineering for high-performance inorganic–organic hybrid perovskite solar cells. *Nature materials*, *13*(9), pp.897-903.

[12] Zhou, H., Chen, Q., Li, G., Luo, S., Song, T.B., Duan, H.S., Hong, Z., You, J., Liu, Y. and Yang, Y., 2014. Interface engineering of highly efficient perovskite solar cells. *Science*, *345*(6196), pp.542-546.

[13] Jeon, N.J., Noh, J.H., Yang, W.S., Kim, Y.C., Ryu, S., Seo, J. and Seok, S.I., 2015. Compositional engineering of perovskite materials for high-performance solar cells. Nature, 517(7535), pp.476-480.

[14] Kojima, A., Teshima, K., Shirai, Y. and Miyasaka, T., 2009. Organometal halide perovskites as visible-light sensitizers for photovoltaic cells. Journal of the American Chemical Society, 131(17), pp.6050-6051.

[15] Stranks, S.D., Eperon, G.E., Grancini, G., Menelaou, C., Alcocer, M.J., Leijtens, T., Herz, L.M., Petrozza, A. and Snaith, H.J., 2013. Electron-hole diffusion lengths exceeding 1 micrometer in an organometal trihalide perovskite absorber. *Science*, *342*(6156), pp.341-344.

[16] Lin, Q., Armin, A., Nagiri, R.C.R., Burn, P.L. and Meredith, P., 2015. Electro-optics of perovskite solar cells. Nature Photonics, 9(2), pp.106-112.

[17] Nie, W., Tsai, H., Asadpour, R., Blancon, J.C., Neukirch, A.J., Gupta, G., Crochet, J.J., Chhowalla, M., Tretiak, S., Alam, M.A. and Wang, H.L., 2015. High-efficiency solution-processed perovskite solar cells with millimeter-scale grains. Science, 347(6221), pp.522-525

[18] Dong, Q., Fang, Y., Shao, Y., Mulligan, P., Qiu, J., Cao, L. and Huang, J., 2015. Electron-hole diffusion lengths> 175 μm in solution-grown $CH_3NH_3PbI_3$ single crystals. Science, 347(6225), pp.967-970.

[19] Jena, A.K., Kulkarni, A. and Miyasaka, T., 2019. Halide perovskite photovoltaics: background, status, and future prospects. Chemical reviews, 119(5), pp.3036-3103.

[20] Kim, H.S., Lee, C.R., Im, J.H., Lee, K.B., Moehl, T., Marchioro, A., Moon, S.J., Humphry-Baker, R., Yum, J.H., Moser, J.E. and Grätzel, M., 2012. Lead iodide perovskite sensitized all-solid-state submicron thin film mesoscopic solar cell with efficiency exceeding 9%. Scientific reports, 2(1), pp.1-7.

[21] Lee, M.M., Teuscher, J., Miyasaka, T., Murakami, T.N. and Snaith, H.J., 2012. Efficient hybrid solar cells based on meso-superstructured organometal halide perovskites. Science, 338(6107), pp.643-647.

[22] Bach, U., Lupo, D., Comte, P., Moser, J.E., Weissörtel, F., Salbeck, J., Spreitzer, H. and Grätzel, M., 1998. Solid-state dye-sensitized mesoporous $TiO_2$ solar cells with high photon-to-electron conversion efficiencies. Nature, 395(6702), pp.583-585.

[23] Wojciechowski, K., Saliba, M., Leijtens, T., Abate, A. and Snaith, H.J., 2014. Sub-150 C processed meso-superstructured perovskite solar cells with enhanced efficiency. Energy & Environmental Science, 7(3), pp.1142-1147.

[24] OXFORD PVs – Next generation solar power, January 2015.

[25] Yin, W.J., Yang, J.H., Kang, J., Yan, Y. and Wei, S.H., 2015. Halide perovskite materials for solar cells: a theoretical review. Journal of Materials Chemistry A, 3(17), pp.8926-8942.

[26] Eperon, G.E., Stranks, S.D., Menelaou, C., Johnston, M.B., Herz, L.M. and Snaith, H.J., 2014. Formamidinium lead trihalide: a broadly tunable perovskite for efficient planar heterojunction solar cells. Energy & Environmental Science, 7(3), pp.982-988.

[27] Goldschmidt, V.M., 1927. Krystallbau und chemische Zusammensetzung. Berichte der deutschen chemischen Gesellschaft (A and B Series), 60(5), pp.1263-1296.

[28] Ava, T.T., Al Mamun, A., Marsillac, S. and Namkoong, G., 2019. A review: thermal stability of methylammonium lead halide based perovskite solar cells. Applied Sciences, 9(1), p.188.

[29] Korshunova, K., Winterfeld, L., Beenken, W.J. and Runge, E., 2016. Thermodynamic stability of mixed Pb: Sn methyl-ammonium halide perovskites. physica status solidi (b), 253(10), pp.1907-1915.

[30] Kawamura, Y., Mashiyama, H. and Hasebe, K., 2002. Structural study on cubic-tetragonal transition of $CH_3NH_3PbI_3$. Journal of the Physical Society of Japan, 71(7), pp.1694-1697.

[31] Whitfield, P.S., Herron, N., Guise, W.E., Page, K., Cheng, Y.Q., Milas, I. and Crawford, M.K., 2016. Structures, phase transitions and tricritical behavior of the hybrid perovskite methyl ammonium lead iodide. Scientific reports, 6(1), pp.1-16.

[32] Burschka, J., Pellet, N., Moon, S.J., Humphry-Baker, R., Gao, P., Nazeeruddin, M.K. and Grätzel, M., 2013. Sequential deposition as a route to high-performance perovskite-sensitized solar cells. *Nature*, *499*(7458), pp.316-319.

[33] Liu, M., Johnston, M.B. and Snaith, H.J., 2013. Efficient planar heterojunction perovskite solar cells by vapour deposition. *Nature*, *501*(7467), pp.395-398.

[34] Eperon, G.E., Burlakov, V.M., Docampo, P., Goriely, A. and Snaith, H.J., 2014. Morphological control for high performance, solution-processed planar heterojunction perovskite solar cells. Advanced Functional Materials, 24(1), pp.151-157.

[35] Heo, J.H., Im, S.H., Noh, J.H., Mandal, T.N., Lim, C.S., Chang, J.A., Lee, Y.H., Kim, H.J., Sarkar, A., Nazeeruddin, M.K. and Grätzel, M., 2013. Efficient inorganic–organic hybrid heterojunction solar cells containing perovskite compound and polymeric hole conductors. Nature photonics, 7(6), pp.486-491.

[36] Unger, E.L., Hoke, E.T., Bailie, C.D., Nguyen, W.H., Bowring, A.R., Heumüller, T., Christoforo, M.G. and McGehee, M.D., 2014. Hysteresis and transient behavior in current–voltage measurements of hybrid-perovskite absorber solar cells. Energy & Environmental Science, 7(11), pp.3690-3698.

[37] Zhao, X., Kim, H.S., Seo, J.Y. and Park, N.G., 2017. Effect of selective contacts on the thermal stability of perovskite solar cells. ACS applied materials & interfaces, 9(8), pp.7148-7153.

[38] Xu, J., Buin, A., Ip, A.H., Li, W., Voznyy, O., Comin, R., Yuan, M., Jeon, S., Ning, Z., McDowell, J.J. and Kanjanaboos, P., 2015. Perovskite–fullerene hybrid materials suppress hysteresis in planar diodes. Nature communications, 6(1), pp.1-8.

[39] Song, Z., Watthage, S.C., Phillips, A.B. and Heben, M.J., 2016. Pathways toward high-performance perovskite solar cells: review of recent advances in organo-metal halide perovskites for photovoltaic applications. Journal of Photonics for Energy, 6(2), p.022001.

[40] Hussain, I., Tran, H.P., Jaksik, J., Moore, J., Islam, N. and Uddin, M.J., 2018. Functional materials, device architecture, and flexibility of perovskite solar cell. Emergent Materials, 1(3), pp.133-154.

[41] Chen, J. and Park, N.G., 2018. Inorganic hole transporting materials for stable and high efficiency perovskite solar cells. The Journal of Physical Chemistry C, 122(25), pp.14039-14063.

[42] Hao, F., Stoumpos, C.C., Cao, D.H., Chang, R.P. and Kanatzidis, M.G., 2014. Lead-free solid-state organic–inorganic halide perovskite solar cells. Nature photonics, 8(6), pp.489-494.

[43] Miyata, A., Mitioglu, A., Plochocka, P., Portugall, O., Wang, J.T.W., Stranks, S.D., Snaith, H.J. and Nicholas, R.J., 2015. Direct measurement of the exciton binding energy and effective masses for charge carriers in organic–inorganic tri-halide perovskites. Nature Physics, 11(7), pp.582-587.

[44] Xing, G., Mathews, N., Sun, S., Lim, S.S., Lam, Y.M., Grätzel, M., Mhaisalkar, S. and Sum, T.C., 2013. Long-range balanced electron-and hole-transport lengths in organic-inorganic CH3NH3PbI3. *Science*, *342*(6156), pp.344-347.

[45] Noh, J.H., Im, S.H., Heo, J.H., Mandal, T.N. and Seok, S.I., 2013. Chemical management for colorful, efficient, and stable inorganic–organic hybrid nanostructured solar cells. *Nano letters*, *13*(4), pp.1764-1769.

[46] Niu, G., Guo, X. and Wang, L., 2015. Review of recent progress in chemical stability of perovskite solar cells. *Journal of Materials Chemistry A*, *3*(17), pp.8970-8980.

[47] Grätzel, M., 2014. The light and shade of perovskite solar cells. *Nature materials*, *13*(9), pp.838-842.

[48] Li, X., Tschumi, M., Han, H., Babkair, S.S., Alzubaydi, R.A., Ansari, A.A., Habib, S.S., Nazeeruddin, M.K., Zakeeruddin, S.M. and Grätzel, M., 2015. Outdoor performance and stability under elevated temperatures and long-term light soaking of triple-layer mesoporous perovskite photovoltaics. *Energy Technology*, *3*(6), pp.551-555.

[49] Chang, Y.H., Park, C.H. and Matsuishi, K., 2004. First-principles study of the Structural and the electronic properties of the lead-Halide-based inorganic-organic perovskites (CH$_3$NH$_3$) PbX$_3$ and CsPbX$_3$ (X= Cl, Br, I). *Journal-Korean Physical Society*, *44*, pp.889-893.

[50] Umari, P., Mosconi, E. and De Angelis, F., 2014. Relativistic GW calculations on CH$_3$NH$_3$PbI$_3$ and CH$_3$NH$_3$SnI$_3$ perovskites for solar cell applications. *Scientific reports*, *4*(1), pp.1-7.

[51] Umebayashi, T., Asai, K., Kondo, T. and Nakao, A., 2003. Electronic structures of lead iodide based low-dimensional crystals. *Physical Review B*, *67*(15), p.155405.

[52] Leijtens, T., Eperon, G.E., Noel, N.K., Habisreutinger, S.N., Petrozza, A. and Snaith, H.J., 2015. Stability of metal halide perovskite solar cells. *Advanced Energy Materials*, *5*(20), p.1500963.

[53] Wasylishen, R.E., Knop, O. and Macdonald, J.B., 1985. Cation rotation in methylammonium lead halides. *Solid state communications*, *56*(7), pp.581-582.

[54] Egger, D.A., Kronik, L. and Rappe, A.M., 2015. Theory of hydrogen migration in organic–inorganic halide perovskites. *Angewandte Chemie International Edition*, *54*(42), pp.12437-12441.

[55] Ball, J.M., Lee, M.M., Hey, A. and Snaith, H.J., 2013. Low-temperature processed meso-superstructured to thin-film perovskite solar cells. *Energy & Environmental Science*, *6*(6), pp.1739-1743.

[56] Stoumpos, C.C., Malliakas, C.D. and Kanatzidis, M.G., 2013. Semiconducting tin and lead iodide perovskites with organic cations: phase transitions, high mobilities, and near-infrared photoluminescent properties. *Inorganic chemistry*, *52*(15), pp.9019-9038.

[57] Im, J.H., Lee, C.R., Lee, J.W., Park, S.W. and Park, N.G., 2011. 6.5% efficient perovskite quantum-dot-sensitized solar cell. *Nanoscale*, *3*(10), pp.4088-4093.

[58] You, J., Meng, L., Song, T.B., Guo, T.F., Yang, Y.M., Chang, W.H., Hong, Z., Chen, H., Zhou, H., Chen, Q. and Liu, Y., 2016. Improved air stability of perovskite solar cells via solution-processed metal oxide transport layers. *Nature nanotechnology*, *11*(1), pp.75-81.

[59] Conings, B., Drijkoningen, J., Gauquelin, N., Babayigit, A., D'Haen, J., D'Olieslaeger, L., Ethirajan, A., Verbeeck, J., Manca, J., Mosconi, E. and Angelis, F.D., 2015. Intrinsic thermal instability of methylammonium lead trihalide perovskite. *Advanced Energy Materials*, *5*(15), p.1500477.

[60] Han, Y., Meyer, S., Dkhissi, Y., Weber, K., Pringle, J.M., Bach, U., Spiccia, L. and Cheng, Y.B., 2015. Degradation observations of encapsulated planar $CH_3NH_3PbI_3$ perovskite solar cells at high temperatures and humidity. *Journal of Materials Chemistry A*, *3*(15), pp.8139-8147.

[61] Wang, F., Shimazaki, A., Yang, F., Kanahashi, K., Matsuki, K., Miyauchi, Y., Takenobu, T., Wakamiya, A., Murata, Y. and Matsuda, K., 2017. Highly efficient and stable perovskite solar

cells by interfacial engineering using solution-processed polymer layer. *The Journal of Physical Chemistry C*, *121*(3), pp.1562-1568.

[62] Habisreutinger, S.N., Leijtens, T., Eperon, G.E., Stranks, S.D., Nicholas, R.J. and Snaith, H.J., 2014. Carbon nanotube/polymer composites as a highly stable hole collection layer in perovskite solar cells. *Nano letters*, *14*(10), pp.5561-5568.

[63] Jeon, N.J., Noh, J.H., Yang, W.S., Kim, Y.C., Ryu, S., Seo, J. and Seok, S.I., 2015. Compositional engineering of perovskite materials for high-performance solar cells. *Nature*, *517*(7535), pp.476-480..

[64] Pellet, N., Gao, P., Gregori, G., Yang, T.Y., Nazeeruddin, M.K., Maier, J. and Grätzel, M., 2014. Mixed-organic-cation Perovskite photovoltaics for enhanced solar-light harvesting. *Angewandte chemie*, *126*(12), pp.3215-3221.

[65] Eperon, G.E., Paternò, G.M., Sutton, R.J., Zampetti, A., Haghighirad, A.A., Cacialli, F. and Snaith, H.J., 2015. Inorganic caesium lead iodide perovskite solar cells. *Journal of Materials Chemistry A*, *3*(39), pp.19688-19695.

[66] Sutton, R.J., Eperon, G.E., Miranda, L., Parrott, E.S., Kamino, B.A., Patel, J.B., Hörantner, M.T., Johnston, M.B., Haghighirad, A.A., Moore, D.T. and Snaith, H.J., 2016. Bandgap-tunable cesium lead halide perovskites with high thermal stability for efficient solar cells. *Advanced Energy Materials*, *6*(8), p.1502458.

[67] Kulbak, M., Gupta, S., Kedem, N., Levine, I., Bendikov, T., Hodes, G. and Cahen, D., 2016. Cesium enhances long-term stability of lead bromide perovskite-based solar cells. *The journal of physical chemistry letters*, *7*(1), pp.167-172.

[68] Beal, R.E., Slotcavage, D.J., Leijtens, T., Bowring, A.R., Belisle, R.A., Nguyen, W.H., Burkhard, G.F., Hoke, E.T. and McGehee, M.D., 2016. Cesium lead halide perovskites with improved stability for tandem solar cells. *The journal of physical chemistry letters*, *7*(5), pp.746-751.

[69] Saliba, M., Matsui, T., Seo, J.Y., Domanski, K., Correa-Baena, J.P., Nazeeruddin, M.K., Zakeeruddin, S.M., Tress, W., Abate, A., Hagfeldt, A. and Grätzel, M., 2016. Cesium-containing triple cation perovskite solar cells: improved stability, reproducibility and high efficiency. *Energy & environmental science*, *9*(6), pp.1989-1997.

[70] McMeekin, D.P., Sadoughi, G., Rehman, W., Eperon, G.E., Saliba, M., Hörantner, M.T., Haghighirad, A., Sakai, N., Korte, L., Rech, B. and Johnston, M.B., 2016. A mixed-cation lead mixed-halide perovskite absorber for tandem solar cells. *Science*, *351*(6269), pp.151-155.

[71] Lee, J.W., Kim, D.H., Kim, H.S., Seo, S.W., Cho, S.M. and Park, N.G., 2015. Formamidinium and cesium hybridization for photo-and moisture-stable perovskite solar cell. *Advanced Energy Materials*, *5*(20), p.1501310.

[72] Li, Z., Yang, M., Park, J.S., Wei, S.H., Berry, J.J. and Zhu, K., 2016. Stabilizing perovskite structures by tuning tolerance factor: formation of formamidinium and cesium lead iodide solid-state alloys. *Chemistry of Materials*, *28*(1), pp.284-292.

[73] Yi, C., Luo, J., Meloni, S., Boziki, A., Ashari-Astani, N., Grätzel, C., Zakeeruddin, S.M., Röthlisberger, U. and Grätzel, M., 2016. Entropic stabilization of mixed A-cation $ABX_3$ metal halide perovskites for high performance perovskite solar cells. *Energy & Environmental Science*, *9*(2), pp.656-662.

[74] Binek, A., Hanusch, F.C., Docampo, P. and Bein, T., 2015. Stabilization of the trigonal high-temperature phase of formamidinium lead iodide. *The journal of physical chemistry letters*, *6*(7), pp.1249-1253.

[75] Saliba, M., Matsui, T., Domanski, K., Seo, J.Y., Ummadisingu, A., Zakeeruddin, S.M., Correa-Baena, J.P., Tress, W.R., Abate, A., Hagfeldt, A. and Grätzel, M., 2016. Incorporation of rubidium cations into perovskite solar cells improves photovoltaic performance. *Science*, *354*(6309), pp.206-209.

[76] Rong, Y., Liu, L., Mei, A., Li, X. and Han, H., 2015. Beyond efficiency: the challenge of stability in mesoscopic perovskite solar cells. *Advanced Energy Materials*, *5*(20), p.1501066.

[77] Pathak, S.K., Abate, A., Ruckdeschel, P., Roose, B., Gödel, K.C., Vaynzof, Y., Santhala, A., Watanabe, S.I., Hollman, D.J., Noel, N. and Sepe, A., 2014. Performance and stability enhancement of dye-sensitized and perovskite solar cells by Al doping of $TiO_2$. *Advanced Functional Materials*, *24*(38), pp.6046-6055.

[78] Ahn, N., Kwak, K., Jang, M.S., Yoon, H., Lee, B.Y., Lee, J.K., Pikhitsa, P.V., Byun, J. and Choi, M., 2016. Trapped charge-driven degradation of perovskite solar cells. *Nature communications*, *7*(1), pp.1-9.

[79] Wojciechowski, K., Stranks, S.D., Abate, A., Sadoughi, G., Sadhanala, A., Kopidakis, N., Rumbles, G., Li, C.Z., Friend, R.H., Jen, A.K.Y. and Snaith, H.J., 2014. Heterojunction modification for highly efficient organic–inorganic perovskite solar cells. *ACS nano*, *8*(12), pp.12701-12709.

[80] Wojciechowski, K., Leijtens, T., Siprova, S., Schlueter, C., Hörantner, M.T., Wang, J.T.W., Li, C.Z., Jen, A.K.Y., Lee, T.L. and Snaith, H.J., 2015. C60 as an efficient n-type compact layer in perovskite solar cells. *The journal of physical chemistry letters*, *6*(12), pp.2399-2405.

[81] Ye, S., Sun, W., Li, Y., Yan, W., Peng, H., Bian, Z., Liu, Z. and Huang, C., 2015. CuSCN-based inverted planar perovskite solar cell with an average PCE of 15.6%. *Nano letters*, *15*(6), pp.3723-3728.

[82] Labban, A.E., Chen, H., Kirkus, M., Barbe, J., Del Gobbo, S., Neophytou, M., McCulloch, I. and Eid, J., 2016. Improved Efficiency in Inverted Perovskite Solar Cells Employing a Novel Diarylamino-Substituted Molecule as PEDOT: PSS Replacement. *Advanced Energy Materials*, *6*(11), p.1502101.

[83] Lee, W., Song, M., Park, S., Nam, S., Seo, J., Kim, H. and Kim, Y., 2016. Acidity-controlled conducting polymer films for organic thermoelectric devices with horizontal and vertical architectures. *Scientific reports*, *6*(1), pp.1-10.

[84] Vitoratos, E., Sakkopoulos, S., Dalas, E., Paliatsas, N., Karageorgopoulos, D., Petraki, F., Kennou, S. and Choulis, S.A., 2009. Thermal degradation mechanisms of PEDOT: PSS. *Organic Electronics*, *10*(1), pp.61-66.

[85] Hu, L., Li, M., Yang, K., Xiong, Z., Yang, B., Wang, M., Tang, X., Zang, Z., Liu, X., Li, B. and Xiao, Z., 2018. PEDOT: PSS monolayers to enhance the hole extraction and stability of perovskite solar cells. *Journal of Materials Chemistry A*, *6*(34), pp.16583-16589.

[86] Zhang, H., Cheng, J., Lin, F., He, H., Mao, J., Wong, K.S., Jen, A.K.Y. and Choy, W.C., 2016. Pinhole-free and surface-nanostructured $NiO_x$ film by room-temperature solution

process for high-performance flexible perovskite solar cells with good stability and reproducibility. *ACS nano*, *10*(1), pp.1503-1511.

[87] Kim, H.S., Seo, J.Y. and Park, N.G., 2016. Impact of selective contacts on long-term stability of $CH_3NH_3PbI_3$ perovskite solar cells. *The Journal of Physical Chemistry C*, *120*(49), pp.27840-27848.

[88] Sheikh, A.D., Bera, A., Haque, M.A., Rakhi, R.B., Del Gobbo, S., Alshareef, H.N. and Wu, T., 2015. Atmospheric effects on the photovoltaic performance of hybrid perovskite solar cells. *Solar Energy Materials and Solar Cells*, *137*, pp.6-14.

[89] Sfyri, G., Kumar, C.V., Raptis, D., Dracopoulos, V. and Lianos, P., 2015. Study of perovskite solar cells synthesized under ambient conditions and of the performance of small cell modules. *Solar Energy Materials and Solar Cells*, *134*, pp.60-63.

[90] Machui, F., Hösel, M., Li, N., Spyropoulos, G.D., Ameri, T., Søndergaard, R.R., Jørgensen, M., Scheel, A., Gaiser, D., Kreul, K. and Lenssen, D., 2014. Cost analysis of roll-to-roll fabricated ITO free single and tandem organic solar modules based on data from manufacture. *Energy & Environmental Science*, *7*(9), pp.2792-2802.

[91] Divitini, G., Cacovich, S., Matteocci, F., Cinà, L., Di Carlo, A. and Ducati, C., 2016. In situ observation of heat-induced degradation of perovskite solar cells. *Nature Energy*, *1*(2), pp.1-6.

[92] Domanski, K., Correa-Baena, J.P., Mine, N., Nazeeruddin, M.K., Abate, A., Saliba, M., Tress, W., Hagfeldt, A. and Grätzel, M., 2016. Not all that glitters is gold: metal-migration-induced degradation in perovskite solar cells. *ACS nano*, *10*(6), pp.6306-6314.

[93] Li, J., Dong, Q., Li, N. and Wang, L., 2017. Direct evidence of ion diffusion for the silver-electrode-induced thermal degradation of inverted perovskite solar cells. *Advanced Energy Materials*, *7*(14), p.1602922.

[94] Mei, A., Li, X., Liu, L., Ku, Z., Liu, T., Rong, Y., Xu, M., Hu, M., Chen, J., Yang, Y. and Grätzel, M., 2014. A hole-conductor–free, fully printable mesoscopic perovskite solar cell with high stability. *science*, *345*(6194), pp.295-298

[95] Baranwal, A.K., Kanaya, S., Peiris, T.N., Mizuta, G., Nishina, T., Kanda, H., Miyasaka, T., Segawa, H. and Ito, S., 2016. 100° C thermal stability of printable perovskite solar cells using porous carbon counter electrodes. *ChemSusChem*, *9*(18), pp.2604-2608.

[96] Dualeh, A., Moehl, T., Tétreault, N., Teuscher, J., Gao, P., Nazeeruddin, M.K. and Grätzel, M., 2014. Impedance spectroscopic analysis of lead iodide perovskite-sensitized solid-state solar cells. *ACS nano*, *8*(1), pp.362-373.

[97] Christians, J.A., Manser, J.S. and Kamat, P.V., 2015. Best practices in perovskite solar cell efficiency measurements. Avoiding the error of making bad cells look good.

[98] Chen, B., Yang, M., Priya, S. and Zhu, K., 2016. Origin of J–V hysteresis in perovskite solar cells. *The journal of physical chemistry letters*, *7*(5), pp.905-917.

[99] Tress, W., Marinova, N., Moehl, T., Zakeeruddin, S.M., Nazeeruddin, M.K. and Grätzel, M., 2015. Understanding the rate-dependent J–V hysteresis, slow time component, and aging in $CH_3NH_3PbI_3$ perovskite solar cells: the role of a compensated electric field. *Energy & Environmental Science*, *8*(3), pp.995-1004.

[100] Sanchez, R.S., Gonzalez-Pedro, V., Lee, J.W., Park, N.G., Kang, Y.S., Mora-Sero, I. and Bisquert, J., 2014. Slow dynamic processes in lead halide perovskite solar cells. Characteristic times and hysteresis. *The journal of physical chemistry letters*, *5*(13), pp.2357-2363.

[101] Chen, B., Yang, M., Zheng, X., Wu, C., Li, W., Yan, Y., Bisquert, J., Garcia-Belmonte, G., Zhu, K. and Priya, S., 2015. Impact of capacitive effect and ion migration on the hysteretic behavior of perovskite solar cells. *The journal of physical chemistry letters*, *6*(23), pp.4693-4700.

[102] Kim, H.S. and Park, N.G., 2014. Parameters affecting I–V hysteresis of $CH_3NH_3PbI_3$ perovskite solar cells: effects of perovskite crystal size and mesoporous TiO2 layer. *The journal of physical chemistry letters*, *5*(17), pp.2927-2934.

[103] Wei, J., Zhao, Y., Li, H., Li, G., Pan, J., Xu, D., Zhao, Q. and Yu, D., 2014. Hysteresis analysis based on the ferroelectric effect in hybrid perovskite solar cells. *The journal of physical chemistry letters*, *5*(21), pp.3937-3945.

[104 Snaith, H.J., Abate, A., Ball, J.M., Eperon, G.E., Leijtens, T., Noel, N.K., Stranks, S.D., Wang, J.T.W., Wojciechowski, K. and Zhang, W., 2014. Anomalous hysteresis in perovskite solar cells. *The journal of physical chemistry letters*, *5*(9), pp.1511-1515.

[105] Chen, B., Zheng, X., Yang, M., Zhou, Y., Kundu, S., Shi, J., Zhu, K. and Priya, S., 2015. Interface band structure engineering by ferroelectric polarization in perovskite solar cells. *Nano Energy*, *13*, pp.582-591.

[106] Ke, W., Fang, G., Wan, J., Tao, H., Liu, Q., Xiong, L., Qin, P., Wang, J., Lei, H., Yang, G. and Qin, M., 2015. Efficient hole-blocking layer-free planar halide perovskite thin-film solar cells. *Nature communications*, *6*(1), pp.1-7.

[107] Zhang, W., Saliba, M., Moore, D.T., Pathak, S.K., Hörantner, M.T., Stergiopoulos, T., Stranks, S.D., Eperon, G.E., Alexander-Webber, J.A., Abate, A. and Sadhanala, A., 2015. Ultrasmooth organic–inorganic perovskite thin-film formation and crystallization for efficient planar heterojunction solar cells. *Nature communications*, *6*(1), pp.1-10.

[108] Ono, L.K., Raga, S.R., Wang, S., Kato, Y. and Qi, Y., 2015. Temperature-dependent hysteresis effects in perovskite-based solar cells. *Journal of Materials Chemistry A*, *3*(17), pp.9074-9080.

[109] Ryu, S., Seo, J., Shin, S.S., Kim, Y.C., Jeon, N.J., Noh, J.H. and Seok, S.I., 2015. Fabrication of metal-oxide-free $CH_3NH_3PbI_3$ perovskite solar cells processed at low temperature. *Journal of Materials Chemistry A*, *3*(7), pp.3271-3275.

[110] Frost, J.M., Butler, K.T. and Walsh, A., 2014. Molecular ferroelectric contributions to anomalous hysteresis in hybrid perovskite solar cells. *Apl Materials*, *2*(8), p.081506.

[111] Almora, O., Zarazua, I., Mas-Marza, E., Mora-Sero, I., Bisquert, J. and Garcia-Belmonte, G., 2015. Capacitive dark currents, hysteresis, and electrode polarization in lead halide perovskite solar cells. *The journal of physical chemistry letters*, *6*(9), pp.1645-1652.

[112] Cojocaru, L., Uchida, S., Jayaweera, P.V., Kaneko, S., Nakazaki, J., Kubo, T. and Segawa, H., 2015. Origin of the hysteresis in I–V curves for planar structure perovskite solar cells rationalized with a surface boundary-induced capacitance model. *Chemistry Letters*, *44*(12), pp.1750-1752.

[113] Jena, A.K., Chen, H.W., Kogo, A., Sanehira, Y., Ikegami, M. and Miyasaka, T., 2015. The interface between FTO and the TiO2 compact layer can be one of the origins to hysteresis in

planar heterojunction perovskite solar cells. *ACS applied materials & interfaces*, *7*(18), pp.9817-9823.

[114] Kim, H.S., Jang, I.H., Ahn, N., Choi, M., Guerrero, A., Bisquert, J. and Park, N.G., 2015. Control of I–V hysteresis in $CH_3NH_3PbI_3$ perovskite solar cell. *The journal of physical chemistry letters*, *6*(22), pp.4633-4639.

[115] Eames, C., Frost, J.M., Barnes, P.R., O'regan, B.C., Walsh, A. and Islam, M.S., 2015. Ionic transport in hybrid lead iodide perovskite solar cells. *Nature communications*, *6*(1), pp.1-8.

[116] Yang, T.Y., Gregori, G., Pellet, N., Grätzel, M. and Maier, J., 2015. The significance of ion conduction in a hybrid organic–inorganic lead-iodide-based perovskite photosensitizer. *Angewandte Chemie International Edition*, *54*(27), pp.7905-7910.

[117] Fabini, D., 2015. Quantifying the potential for lead pollution from halide perovskite photovoltaics.

[118] Noel, N.K., Stranks, S.D., Abate, A., Wehrenfennig, C., Guarnera, S., Haghighirad, A.A., Sadhanala, A., Eperon, G.E., Pathak, S.K., Johnston, M.B. and Petrozza, A., 2014. Lead-free organic–inorganic tin halide perovskites for photovoltaic applications. *Energy & Environmental Science*, *7*(9), pp.3061-3068.

[119] Shi, Z. and Jayatissa, A.H., 2018. Perovskites-based solar cells: A review of recent progress, materials and processing methods. *Materials*, *11*(5), p.729.

[120] Zhu, H.L., Xiao, J., Mao, J., Zhang, H., Zhao, Y. and Choy, W.C., 2017. Controllable Crystallization of CH3NH3Sn0. 25Pb0. 75I3 Perovskites for Hysteresis-Free Solar Cells with Efficiency Reaching 15.2%. *Advanced Functional Materials*, *27*(11), p.1605469.

[121] Park, B.W., Philippe, B., Zhang, X., Rensmo, H., Boschloo, G. and Johansson, E.M., 2015. Bismuth based hybrid perovskites $A_3Bi_2I_9$ (A: methylammonium or cesium) for solar cell application. *Advanced materials*, *27*(43), pp.6806-6813.

[122] Ming, W., Shi, H. and Du, M.H., 2016. Large dielectric constant, high acceptor density, and deep electron traps in perovskite solar cell material $CsGeI_3$. *Journal of Materials Chemistry A*, *4*(36), pp.13852-13858.

[123] Lu, X., Zhao, Z., Li, K., Han, Z., Wei, S., Guo, C., Zhou, S., Wu, Z., Guo, W. and Wu, C.M.L., 2016. First-principles insight into the photoelectronic properties of Ge-based perovskites. *RSC advances*, *6*(90), pp.86976-86981.

[124] Jacobsson, T.J., Pazoki, M., Hagfeldt, A. and Edvinsson, T., 2015. Goldschmidt's rules and strontium replacement in lead halogen perovskite solar cells: theory and preliminary experiments on CH3NH3SrI3. *The Journal of Physical Chemistry C*, *119*(46), pp.25673-25683.

[125] Uribe, J.I., Ramirez, D., Osorio-Guillén, J.M., Osorio, J. and Jaramillo, F., 2016. $CH_3NH_3CaI_3$ perovskite: synthesis, characterization, and first-principles studies. *The Journal of Physical Chemistry C*, *120*(30), pp.16393-16398.

[126] Lee, M.M., Teuscher, J., Miyasaka, T., Murakami, T.N. and Snaith, H.J., 2012. Efficient hybrid solar cells based on meso-superstructured organometal halide perovskites. *Science*, *338*(6107), pp.643-647.

[127] Zhou, H., Chen, Q., Li, G., Luo, S., Song, T.B., Duan, H.S., Hong, Z., You, J., Liu, Y. and Yang, Y., 2014. Interface engineering of highly efficient perovskite solar cells. *Science*, *345*(6196), pp.542-546.

[128] Jeon, N.J., Lee, H.G., Kim, Y.C., Seo, J., Noh, J.H., Lee, J. and Seok, S.I., 2014. o-Methoxy substituents in spiro-OMeTAD for efficient inorganic–organic hybrid perovskite solar cells. *Journal of the American Chemical Society*, *136*(22), pp.7837-7840.

[129] Peng, J., Sun, Y., Chen, Y., Yao, Y. and Liang, Z., 2016. Light and thermally induced evolutional charge transport in $CH_3NH_3PbI_3$ perovskite solar cells. *ACS Energy Letters*, *1*(5), pp.1000-1006.

[130] Deretzis, I., Alberti, A., Pellegrino, G., Smecca, E., Giannazzo, F., Sakai, N., Miyasaka, T. and La Magna, A., 2015. Atomistic origins of $CH_3NH_3PbI_3$ degradation to $PbI_2$ in vacuum. *Applied Physics Letters*, *106*(13), p.131904.

[131] Yang, B., Dyck, O., Ming, W., Du, M.H., Das, S., Rouleau, C.M., Duscher, G., Geohegan, D.B. and Xiao, K., 2016. Observation of nanoscale morphological and structural degradation in perovskite solar cells by in situ TEM. *ACS applied materials & interfaces*, *8*(47), pp.32333-32340.

[132] Brivio, F., Frost, J.M., Skelton, J.M., Jackson, A.J., Weber, O.J., Weller, M.T., Goni, A.R., Leguy, A.M., Barnes, P.R. and Walsh, A., 2015. Lattice dynamics and vibrational spectra of the orthorhombic, tetragonal, and cubic phases of methylammonium lead iodide. *Physical Review B*, *92*(14), p.144308.

[133] Chen, Q., De Marco, N., Yang, Y.M., Song, T.B., Chen, C.C., Zhao, H., Hong, Z., Zhou, H. and Yang, Y., 2015. Under the spotlight: The organic–inorganic hybrid halide perovskite for optoelectronic applications. *Nano Today*, *10*(3), pp.355-396.

[134] Ahn, N., Son, D.Y., Jang, I.H., Kang, S.M., Choi, M. and Park, N.G., 2015. Highly reproducible perovskite solar cells with average efficiency of 18.3% and best efficiency

of 19.7% fabricated via Lewis base adduct of lead (II) iodide. *Journal of the American Chemical Society*, *137*(27), pp.8696-8699.

[135] Domanski, K., Tress, W., Moehl, T., Saliba, M., Nazeeruddin, M.K. and Grätzel, M., 2015. Working principles of perovskite photodetectors: analyzing the interplay between photoconductivity and voltage-driven energy-level alignment. *Advanced Functional Materials*, *25*(44), pp.6936-6947.

[136] Tan, Z.K., Moghaddam, R.S., Lai, M.L., Docampo, P., Higler, R., Deschler, F., Price, M., Sadhanala, A., Pazos, L.M., Credgington, D. and Hanusch, F., 2014. Bright light-emitting diodes based on organometal halide perovskite. *Nature nanotechnology*, *9*(9), pp.687-692.

[137] Xing, G., Mathews, N., Lim, S.S., Yantara, N., Liu, X., Sabba, D., Grätzel, M., Mhaisalkar, S. and Sum, T.C., 2014. Low-temperature solution-processed wavelength-tunable perovskites for lasing. *Nature materials*, *13*(5), pp.476-480.

[138] Saliba, M., Wood, S.M., Patel, J.B., Nayak, P.K., Huang, J., Alexander-Webber, J.A., Wenger, B., Stranks, S.D., Hörantner, M.T., Wang, J.T.W. and Nicholas, R.J., 2016. Structured organic–inorganic perovskite toward a distributed feedback laser. *Advanced Materials*, *28*(5), pp.923-929.

[139] Leguy, A.M., Hu, Y., Campoy-Quiles, M., Alonso, M.I., Weber, O.J., Azarhoosh, P., Van Schilfgaarde, M., Weller, M.T., Bein, T., Nelson, J. and Docampo, P., 2015. Reversible hydration of $CH_3NH_3PbI_3$ in films, single crystals, and solar cells. *Chemistry of Materials*, *27*(9), pp.3397-3407.

[140] Wang, Z., Shi, Z., Li, T., Chen, Y. and Huang, W., 2017. Stability of perovskite solar cells: a prospective on the substitution of the A cation and X anion. *Angewandte Chemie International Edition*, *56*(5), pp.1190-1212.

[141] Berhe, T.A., Su, W.N., Chen, C.H., Pan, C.J., Cheng, J.H., Chen, H.M., Tsai, M.C., Chen, L.Y., Dubale, A.A. and Hwang, B.J., 2016. Organometal halide perovskite solar cells: degradation and stability. *Energy & Environmental Science*, *9*(2), pp.323-356.

[142] Djurišić, A.B., Liu, F., Ng, A.M., Dong, Q., Wong, M.K., Ng, A. and Surya, C., 2016. Stability issues of the next generation solar cells. *physica status solidi (RRL)–Rapid Research Letters*, *10*(4), pp.281-299.

[143] Huang, D., Swanson, E.A., Lin, C.P., Schuman, J.S., Stinson, W.G., Chang, W., Hee, M.R., Flotte, T., Gregory, K. and Puliafito, C.A., 1991. Optical coherence tomography. *science*, *254*(5035), pp.1178-1181.

[144] Misra, R.K., Aharon, S., Li, B., Mogilyansky, D., Visoly-Fisher, I., Etgar, L. and Katz, E.A., 2015. Temperature-and component-dependent degradation of perovskite photovoltaic materials under concentrated sunlight. *The journal of physical chemistry letters*, *6*(3), pp.326-330.

[145] Leijtens, T., Eperon, G.E., Pathak, S., Abate, A., Lee, M.M. and Snaith, H.J., 2013. Overcoming ultraviolet light instability of sensitized $TiO_2$ with meso-superstructured organometal tri-halide perovskite solar cells. *Nature communications*, *4*(1), pp.1-8.

[146] Bryant, D., Aristidou, N., Pont, S., Sanchez-Molina, I., Chotchunangatchaval, T., Wheeler, S., Durrant, J.R. and Haque, S.A., 2016. Light and oxygen induced

degradation limits the operational stability of methylammonium lead triiodide perovskite solar cells. *Energy & Environmental Science*, *9*(5), pp.1655-1660.

[147] Luo, P., Liu, Z., Xia, W., Yuan, C., Cheng, J. and Lu, Y., 2015. Uniform, stable, and efficient planar-heterojunction perovskite solar cells by facile low-pressure chemical vapor deposition under fully open-air conditions. *ACS applied materials & interfaces*, *7*(4), pp.2708-2714.

[148] Dewprashad, B. and Eisenbraun, E.J., 1994. Fundamentals of epoxy formulation. *Journal of chemical education*, *71*(4), p.290.

[149] Wang, Q., Chen, B., Liu, Y., Deng, Y., Bai, Y., Dong, Q. and Huang, J., 2017. Scaling behavior of moisture-induced grain degradation in polycrystalline hybrid perovskite thin films. *Energy & Environmental Science*, *10*(2), pp.516-522.

[150] Park, C., Ko, H., Sin, D.H., Song, K.C. and Cho, K., 2017. Organometal halide perovskite solar cells with improved thermal stability via grain boundary passivation using a molecular additive. *Advanced Functional Materials*, *27*(42), p.1703546.

[151] Wen, X., Wu, J., Ye, M., Gao, D. and Lin, C., 2016. Interface engineering via an insulating polymer for highly efficient and environmentally stable perovskite solar cells. *Chemical Communications*, *52*(76), pp.11355-11358.

[152] Corsini, F. and Griffini, G., 2020. Recent progress in encapsulation strategies to enhance the stability of organometal halide perovskite solar cells. *Journal of Physics: Energy*, *2*(3), p.031002.

[153] Physical properties table, https://static.thermoscientific.com/images/D20826%7E.pdf, accessed April 2021.

[154] Feng, J., Athanassiou, A., Bonaccorso, F. and Fragouli, D., 2018. Enhanced electrical conductivity of poly (methyl methacrylate) filled with graphene and in situ synthesized gold nanoparticles. *Nano Futures*, *2*(2), p.025003.

[155] McKenna, B., Troughton, J.R., Watson, T.M. and Evans, R.C., 2017. Enhancing the stability of organolead halide perovskite films through polymer encapsulation. *RSC advances*, *7*(52), pp.32942-32951.

[156] Han, G.S., Yoo, J.S., Yu, F., Duff, M.L., Kang, B.K. and Lee, J.K., 2017. Highly stable perovskite solar cells in humid and hot environment. *Journal of Materials Chemistry A*, *5*(28), pp.14733-14740.

[157] Habisreutinger, S.N., McMeekin, D.P., Snaith, H.J. and Nicholas, R.J., 2016. Research Update: Strategies for improving the stability of perovskite solar cells. *APL Materials*, *4*(9), p.091503.

[158] Yu, H.M., Oh, H.M., Park, D.Y. and Jeong, M.S., 2020. Nanochemical Investigation of Degradation in Organic–Inorganic Hybrid Perovskite Films Using Infrared Nanoscopy. *The Journal of Physical Chemistry C*, *124*(6), pp.3915-3922.

[159] Strelcov, E., Dong, Q., Li, T., Chae, J., Shao, Y., Deng, Y., Gruverman, A., Huang, J. and Centrone, A., 2017. $CH_3NH_3PbI_3$ perovskites: Ferroelasticity revealed. *Science advances*, *3*(4), p.e1602165.

[160] Chae, J., Dong, Q., Huang, J. and Centrone, A., 2015. Chloride incorporation process in $CH_3NH_3PbI_{3-x}Cl_x$ perovskites via nanoscale bandgap maps. *Nano letters*, *15*(12), pp.8114-8121.

[161] Katzenmeyer, A.M., Holland, G., Kjoller, K. and Centrone, A., 2015. Absorption spectroscopy and imaging from the visible through mid-infrared with 20 nm resolution. *Analytical chemistry*, *87*(6), pp.3154-3159.

[162] Duan, G., Zhang, C., Li, A., Yang, X., Lu, L. and Wang, X., 2008. Preparation and characterization of mesoporous zirconia made by using a poly (methyl methacrylate) template. *Nanoscale research letters*, *3*(3), pp.118-122.

[163] G Abdelmageed, G., Jewell, L., Hellier, K., Seymour, L., Luo, B., Bridges, F., Zhang, J.Z. and Carter, S., 2016. Mechanisms for light induced degradation in MAPbI$_3$ perovskite thin films and solar cells. *Applied Physics Letters*, *109*(23), p.233905.

[164] Davis, E.A. and Mott, N., 1970. Conduction in non-crystalline systems V. Conductivity, optical absorption and photoconductivity in amorphous semiconductors. *Philosophical magazine*, *22*(179), pp.0903-0922.

[165] Tauc, J., Grigorovici, R. and Vancu, A., 1966. Optical properties and electronic structure of amorphous germanium. *physica status solidi (b)*, *15*(2), pp.627-637

[166] Leguy, A.M., Azarhoosh, P., Alonso, M.I., Campoy-Quiles, M., Weber, O.J., Yao, J., Bryant, D., Weller, M.T., Nelson, J., Walsh, A. and Van Schilfgaarde, M., 2016. Experimental and theoretical optical properties of methylammonium lead halide perovskites. *Nanoscale*, *8*(12), pp.6317-6327.

[167] Kim, T.G., Seo, S.W., Kwon, H., Hahn, J. and Kim, J.W., 2015. Influence of halide precursor type and its composition on the electronic properties of vacuum deposited perovskite films. *Physical Chemistry Chemical Physics*, *17*(37), pp.24342-24348.

[168] Reyes-Acosta, M.A., Torres-Huerta, A.M., Domínguez-Crespo, M.A., Flores-Vela, A.I., Dorantes-Rosales, H.J. and Andraca-Adame, J.A., 2015. Thermal, mechanical and UV-shielding properties of poly (methyl methacrylate)/cerium dioxide hybrid systems obtained by melt compounding. *Polymers*, *7*(9), pp.1638-1659.

[169] Berglund, B. and Vaughan, R.W., 1980. Correlations between proton chemical shift tensors, deuterium quadrupole couplings, and bond distances for hydrogen bonds in solids. *The Journal of Chemical Physics*, *73*(5), pp.2037-2043.

[170] Fan, Z., Xiao, H., Wang, Y., Zhao, Z., Lin, Z., Cheng, H.C., Lee, S.J., Wang, G., Feng, Z., Goddard III, W.A. and Huang, Y., 2017. Layer-by-layer degradation of methylammonium lead tri-iodide perovskite microplates. *Joule*, *1*(3), pp.548-562.

[171] Zhao, Y., Wei, J., Li, H., Yan, Y., Zhou, W., Yu, D. and Zhao, Q., 2016. A polymer scaffold for self-healing perovskite solar cells. *Nature communications*, *7*(1), pp.1-9.

[172] Song, Z., Abate, A., Watthage, S.C., Liyanage, G.K., Phillips, A.B., Steiner, U., Graetzel, M. and Heben, M.J., 2016. Perovskite solar cell stability in humid air: partially reversible phase transitions in the $PbI_2$-$CH_3NH_3I$-$H_2O$ system. *Advanced Energy Materials*, *6*(19), p.1600846.

[173] Li, X., Tschumi, M., Han, H., Babkair, S.S., Alzubaydi, R.A., Ansari, A.A., Habib, S.S., Nazeeruddin, M.K., Zakeeruddin, S.M. and Grätzel, M., 2015. Outdoor performance and stability under elevated temperatures and long-term light soaking of triple-layer mesoporous perovskite photovoltaics. *Energy Technology*, *3*(6), pp.551-555.

[174] Leguy, A.M., Hu, Y., Campoy-Quiles, M., Alonso, M.I., Weber, O.J., Azarhoosh, P., Van Schilfgaarde, M., Weller, M.T., Bein, T., Nelson, J. and Docampo, P., 2015. Reversible

hydration of $CH_3NH_3PbI_3$ in films, single crystals, and solar cells. *Chemistry of Materials*, *27*(9), pp.3397-3407.

[175] Reese, M.O., Nardes, A.M., Rupert, B.L., Larsen, R.E., Olson, D.C., Lloyd, M.T., Shaheen, S.E., Ginley, D.S., Rumbles, G. and Kopidakis, N., 2010. Photoinduced degradation of polymer and polymer–fullerene active layers: experiment and theory. *Advanced Functional Materials*, *20*(20), pp.3476-3483.

[176] Krebs, F.C. and Norrman, K., 2007. Analysis of the failure mechanism for a stable organic photovoltaic during 10 000 h of testing. *Progress in Photovoltaics: Research and Applications*, *15*(8), pp.697-712.

[177] Bi, D., Gao, P., Scopelliti, R., Oveisi, E., Luo, J., Grätzel, M., Hagfeldt, A. and Nazeeruddin, M.K., 2016. High-performance perovskite solar cells with enhanced environmental stability based on amphiphile-modified $CH_3NH_3PbI_3$. *Advanced Materials*, *28*(15), pp.2910-2915.

[178] Chen, W., Wu, Y., Yue, Y., Liu, J., Zhang, W., Yang, X., Chen, H., Bi, E., Ashraful, I., Grätzel, M. and Han, L., 2015. Efficient and stable large-area perovskite solar cells with inorganic charge extraction layers. *Science*, *350*(6263), pp.944-948.

[179] Møller, C.K., 1958. Crystal structure and photoconductivity of caesium plumbohalides. *Nature*, *182*(4647), pp.1436-1436.

[180] Saliba, M., Orlandi, S., Matsui, T., Aghazada, S., Cavazzini, M., Correa-Baena, J.P., Gao, P., Scopelliti, R., Mosconi, E., Dahmen, K.H. and De Angelis, F., 2016. A molecularly engineered hole-transporting material for efficient perovskite solar cells. *Nature Energy*, *1*(2), pp.1-7.

[181] Amat, A., Mosconi, E., Ronca, E., Quarti, C., Umari, P., Nazeeruddin, M.K., Gratzel, M. and De Angelis, F., 2014. Cation-induced band-gap tuning in organohalide perovskites: interplay of spin–orbit coupling and octahedra tilting. *Nano letters*, *14*(6), pp.3608-3616.

[182] Choi, H., Jeong, J., Kim, H.B., Kim, S., Walker, B., Kim, G.H. and Kim, J.Y., 2014. Cesium-doped methylammonium lead iodide perovskite light absorber for hybrid solar cells. *Nano Energy*, *7*, pp.80-85.

[183] Niu, G., Li, W., Meng, F., Wang, L., Dong, H. and Qiu, Y., 2014. Study on the stability of $CH_3NH_3PbI_3$ films and the effect of post-modification by aluminum oxide in all-solid-state hybrid solar cells. *Journal of Materials Chemistry A*, *2*(3), pp.705-710.

[184] Kim, I.S. and Martinson, A.B., 2015. Stabilizing hybrid perovskites against moisture and temperature via non-hydrolytic atomic layer deposited overlayers. *Journal of Materials Chemistry A*, *3*(40), pp.20092-20096.

[185] Wilderspin, T.J., De Rossi, F. and Watson, T.M., 2016. A simple method to evaluate the effectiveness of encapsulation materials for perovskite solar cells. *Solar Energy*, *139*, pp.426-432.

[186] Namkoong, G., Jeong, H.J., Mamun, A., Byun, H., Demuth, D. and Jeong, M.S., 2016. Chemically, spatially, and temporally resolved 2D mapping study for the role of grain interiors and grain boundaries of organic-inorganic lead halide perovskites. *Solar Energy Materials and Solar Cells*, *155*, pp.134-140.

[187] Gu, S., Zhu, P., Lin, R., Tang, M., Zhu, S. and Zhu, J., 2017. Thermal-stable mixed-cation lead halide perovskite solar cells. *Chinese Optics Letters*, *15*(9), p.093501.

[188] Niu, G., Yu, H., Li, J., Wang, D. and Wang, L., 2016. Controlled orientation of perovskite films through mixed cations toward high performance perovskite solar cells. *Nano Energy*, *27*, pp.87-94.

[189] Yin, W.J., Shi, T. and Yan, Y., 2014. Unique properties of halide perovskites as possible origins of the superior solar cell performance. *Advanced Materials*, *26*(27), pp.4653-4658.

[190] Agiorgousis, M.L., Sun, Y.Y., Zeng, H. and Zhang, S., 2014. Strong covalency-induced recombination centers in perovskite solar cell material $CH_3NH_3PbI_3$. *Journal of the American Chemical Society*, *136*(41), pp.14570-14575.

[191] Wang, C., Song, Z., Zhao, D., Awni, R.A., Li, C., Shrestha, N., Chen, C., Yin, X., Li, D., Ellingson, R.J. and Zhao, X., 2019. Improving Performance and Stability of Planar Perovskite Solar Cells through Grain Boundary Passivation with Block Copolymers. *Solar RRL*, *3*(9), p.1900078.

[192] Mott, N.F. and Davis, E.A., 2012. *Electronic processes in non-crystalline materials*. Oxford university press.

[193] Tauc, J., Grigorovici, R. and Vancu, A., 1966. Optical properties and electronic structure of amorphous germanium. *physica status solidi (b)*, *15*(2), pp.627-637.

[194] Zhao, Y., Lu, Q., Chen, D. and Wei, Y., 2006. Superhydrophobic modification of polyimide films based on gold-coated porous silver nanostructures and self-assembled monolayers. *Journal of Materials Chemistry*, *16*(46), pp.4504-4509.

# VITA

Tanzila Tasnim Ava

tava001@odu.edu, (757)-683-3741

ECE Dept., Old Dominion University

Norfolk, VA, USA

Education

| | | |
|---|---|---|
| PhD | Old Dominion University, Norfolk, VA, USA<br>Ph.D. Candidate, Electrical and Computer Engineering | expected August 2021 |
| MS | Karlsruhe Institute of Technology, Karlsruhe, Germany<br>Optics and Photonics | October 2015 |
| BS | University of Dhaka, Bangladesh<br>Applied Physics, Electronics, and Communication Engineering | June 2012 |

Experience

- Old Dominion University, Norfolk, VA, USA

    o Graduate Research Assistant, January 2016 – present

    o Graduate Teaching Assistant, August 2016 – present

- Institute of Microstructure Technology, KIT, Germany

    o Intern, March 2015 – April 2015

Honors and Awards

- European Erasmus Mundus Scholarship on EUROPHOTONICS to study Optics and Photonics in France, Germany, and Spain, Oct '13 - Oct '15.

Publications

- Published 11 peer-reviewed journal papers and 2 conference proceedings.